Jordi **Marin Garcia**

Off-Axis Holography in **Microwave Imaging** Systems

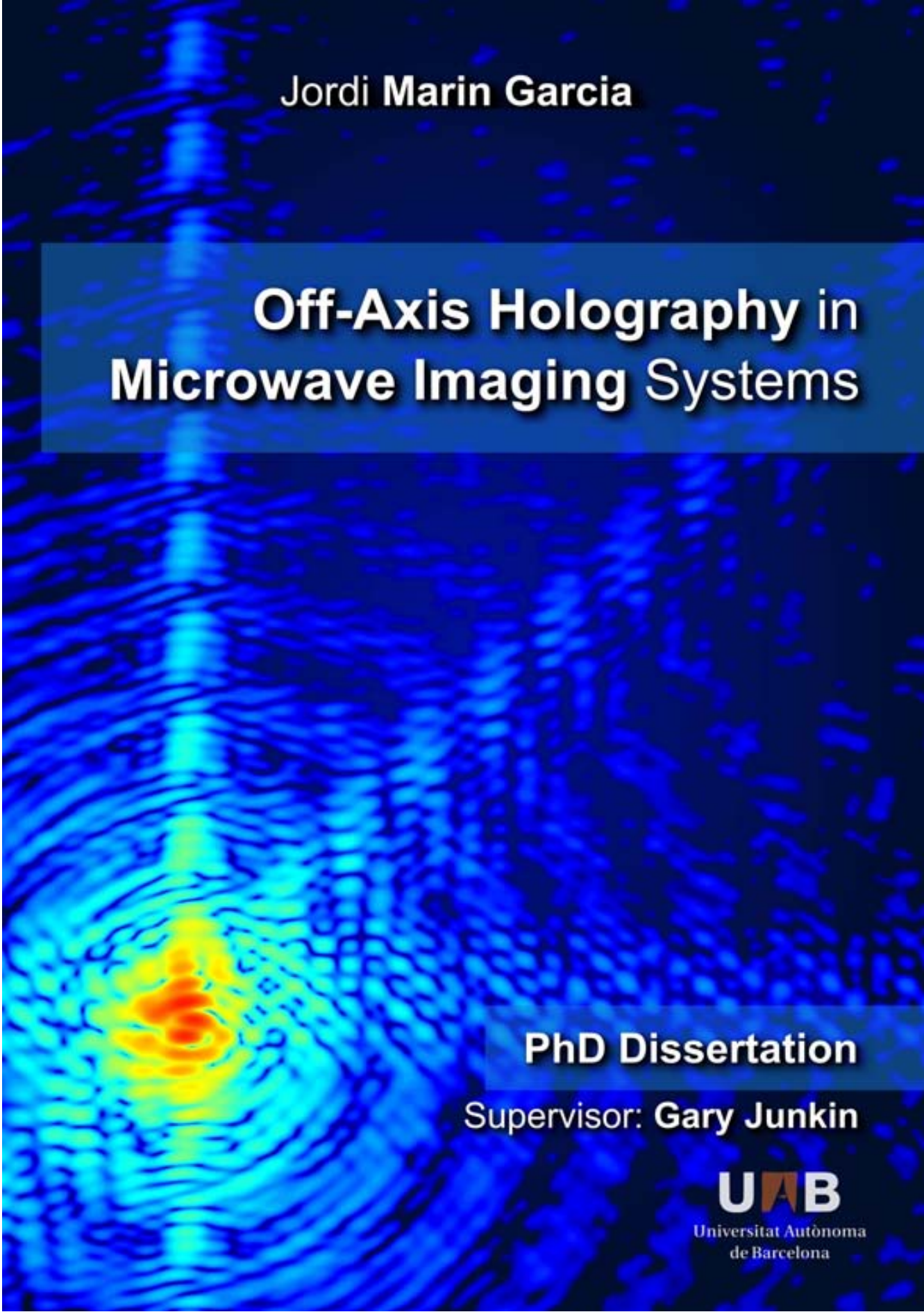

PhD Dissertation

Supervisor: **Gary Junkin**

UAB
Universitat Autònoma
de Barcelona

Jordi Marin Garcia

PhD Dissertation

Off-Axis Holography in Microwave Imaging Systems

X-Band and W-Band Imaging

Supervisor: Gary Junkin

Universitat Autònoma de Barcelona

Department of Telecommunication and Systems Engineering

Off-Axis Holography in Microwave Imaging Systems

By

Jordi Marin Garcia

Dr. G. Junkin, lecturer Professor at Universitat Autònoma de Barcelona

CERTIFIES:

That the thesis entitled **Off-Axis Holography in Microwave Imaging Systems** and submitted by **Jordi Marin Garcia** in partial fulfilment of the requirements for the degree of Doctor in Telecommunications and Systems Engineering, embodies original work done by Mr. Marin under Dr. Junkin's supervision.

Dr. Gary Junkin, Thesis Supervisor

Jordi Marin Garcia, PhD Student

Thanks to all of you who contributed,
even in the slightest possible way,
to the completion of this Ph.D.
With special recognition to family, friends
and most importantly, to you, Maria.

CONTENTS

List of Figures

ACRONYMS

Acronyms

ADC Analog-to-Digital Converter. 14, 93, 125

AMC Active Multiplier Chain. 12, 13

CMB Cosmic Microwave Background. 2

CW Continuos-Wave. 8, 11, 12

DSS Direct Digital Synthesis. 108, 122

EHF Extremely High Frequency. 1

FBW Fractional Bandwidth. 68

FFT Fast Fourier Transform. 10, 43, 124

FMCW Frequency Modulated Continuous Wave. 26

GHZ Gigahertz. 1

HB Harmonic Balance. 70

HEB Hot Electron Bolometer. 13, 15, 16

HIFI Heterodyne Instrument for the Far Infrared. 15, 16

IED Improvised Explosive Device. 7, 8

IF Intermediate Frequency. 14

IR Infrared. 8

ITU International Telecommunication Union. 1

LO Local Oscillator. 14, 16

LSF Line Spread Function. 107

LSSP Large-Signal S-Parameters. 70

NDT Non-Destructive Testing. 5, 6

NEP Noise Equivalent Power. 24

PSF Point Spread Function. 106

PWS Plane-Wave Spectrum. 49

QCL Quantum Cascade Laser. 11, 12

RAM Radar Absorbent Material. 107

SIS Superconductor Insulator Superconductor. 13

TES Transition Edge Sensor. 15

THZ Terahertz. 1

TSS Tangential Signal Sensitivity. 24

VNA Vector Network Analyzer. 67, 98, 99, 101–104, 108, 122

CHAPTER 

INTRODUCTION

In the past few decades, technological advances in electromagnetics have allowed to push the upper frequency limit of microwave devices towards millimeter and submillimeter wave ranges.

Even though standardization is not yet fully available for those frequency bands, the following frequency range definitions are going to be used through all the ongoing text. Millimeter waves occur in the radio frequency spectrum ranging between 30 to 300 Gigahertz (GHz)[1] (10 mm to 1 mm wavelength in vacuum for a more optical physics approach) recognized as the Extremely High Frequency (EHF) band from the International Telecommunication Union (ITU) [1]. The frequency spectrum known as the submillimeter wave band ranges from the upper limit of millimeter waves, 300 GHz, to either 3 or 10 Terahertz (THz)[2] (depending on the author) and corresponds to the lower limit of the far-infrared spectrum. There is no nomenclature available yet from ITU regulations but some speculations lean towards the acronym Tremendously High

[1] GHz $\equiv 1 \cdot 10^9$ cycles per second = 10^9 Hz

[2] THz $\equiv 1 \cdot 10^{12}$ cycles per second = 10^{12} Hz = 1000 GHz

Frequency (THF). One last frequency range known as the Terahertz band is commonly used and loosely defined to comprise from 100 GHz to 10 THz, thus comprising part of both millimeter and submillimeter wave bands. It is also worth to define here the most used bands throughout the dissertation, X-Band comprising from 8 to 12 GHz and W-Band ranging between 75 to 110 GHz.

1.1 Background and motivation

In past decades research in terahertz technology was solely motivated by instruments for topics such as astrophysics, planetary and earth sciences. Molecular line spectroscopy detection, identification and mapping of thermal emission and absorption signatures from low pressure gases comprised the main focus for most scientific requirements and motivated the development of terahertz instrumentation and technology [2]. In addition, the Cosmic Microwave Background (CMB) radiation is also confined to frequencies inside the millimeter wave spectrum with peak intensity at 150 GHz [3]. Concurrently to the development of this thesis different instruments have been released such as the Planck spacecraft, launched on May 2009 for studying the CMB. Planck uses nine bands ranging from 30 to 857 GHz in order to image CMB temperature anisotropies with unprecedented resolution [4]. Still under construction, the Atacama Large Millimeter Array (ALMA) has been designed to provide new and unique insights into the formation of galaxies, stars, planets and chemical precursors for life itself. ALMA is an international effort which will comprise of more than sixty 12-meter receivers with ten frequency bands ranging from 31 to 950 GHz [5, 6].

In spite of the scientific contributions of terahertz radiation, its spectrum is still one of the least used electromagnetic bands in commercial use. The unavailability of sources, sensors, sub-systems and instruments have been a cumbersome issue over the past years for its wide-spread use in commercial instrumentation. The combination of technological advances coming from the space-based community, along with the emergence of new applications, have

managed to drive again the interest from both public and private sectors which has renewed and skyrocketed the funding and research in terahertz applications and devices.

Aside from the aforementioned scientific interests, terahertz radiation has appealing characteristics such as good imaging resolution (as compared to lower frequencies), material penetration, spectroscopic capabilities, water absorption and low energy levels.

The work of this thesis is part of a Spanish national research project called Terasense. The main focus of the project is to equip national academic research institutions with a completely new set of instrumentations and capabilities in order to advance towards the current state of the art in millimeter and submillimeter wave technologies. Sixteen teams throughout the country have combined their efforts to integrate different areas of expertise from numerical electromagnetic simulation to high frequency device design and manufacturing in order to address the challenge of providing a joint public-private framework for research and development in both research institutions and industry. The final goal for the Terasense project is to design and develop different imaging systems at 100 GHz, 300 GHz and 0.5-3 THz.

1.2 Terahertz Radiation

The appealing features of terahertz radiation can be summarized as:

- **Very low energy levels (1-50 meV)**
  One of the key points of interest in many applications is that terahertz radiation, in comparison to X-rays, is a non-ionizing radiation and therefore it does not distort the atomic structure of biological bodies [7]. The energy levels required to damage biological cells or tissue must be on excess of 1 eV, which correspond to signals beyond near-infrared spectrum. Damage to cells is still possible due to thermal heating of biological tissues by using large amounts of power.

- **Spectroscopic capability**
  Terahertz radiation is specially adequate to detect energies consistent with discrete molecular vibration, torsion and liberation modes in liquids, solids and gases [8]. This makes it ideal to identify chemical elements and some of their properties. Moreover the ability to detect different modes in materials allows terahertz microscopy to identify different crystalline structures of the same pharmaceutical compound. Those different forms or polymorphs have the same chemical formula but different physical and chemical properties. For example, it has been described that terahertz radiation properly identifies and discriminates between different dissolution rates and even different stability forms of a same pharmaceutical drug [9].

- **Material Penetration**
  Terahertz waves are able to penetrate through thin layers of materials such as plastics, ceramics, clothes or even skin. This means that many optically opaque materials are transparent at terahertz radiation which make them ideal for non-destructive testing, concealed thread detection or medical imaging. It is worth noting that since penetration is inversely proportional to frequency, the lower band comprised of the millimeter wave band will be more suited for thick materials penetration.

- **Imaging resolution**
  Since imaging resolution is proportional to wavelength, terahertz spectrum has the ability to obtain relatively good imaging resolutions as compared to optics, while maintaining the other interesting properties as seen on lower frequencies. The resolution can be shown to be on the order of few centimeters to a few tens of microns, which are suitable for image recognition in different applications.

- **Water absorption**
  The terahertz spectrum is specially vulnerable to losses in water mediums which make them unsuitable for long range earth communications.

Even though this is a major drawback, some promising applications rely on this feature to obtain greater contrast between different biological tissues, in food quality testing, or cancer detection.

1.3 Terahertz Applications

Commercial applications opportunities have been focused by multiple research groups in different fields. In the following sections a brief introduction to different applications currently under research is presented for applications awaiting a wide-spread commercial deployment. For a more profound understanding of each application and both its features and requirements, different reviews for each specific application have been cited.

1.3.1 Medical Applications

The medical field has shown great interest in both imaging and spectroscopic capabilities of terahertz for non-invasive an non-hazardous diagnostic of cancer tissue as well as wound, dental or burn tissue assessment [10].

Different systems have been used both *in vivo* and *in vitro* for different types of cancer, where the variation of water content is shown to provide enough contrast for its detection. For example skin carcinoma is a good candidate for *in vivo* terahertz detection by means of reflection based measurements since no absorption of outer layers of skin and muscle are present. Multiple techniques for breast cancer are being developed for early detection as well as *in situ* mapping of the cancerous area to be surgically removed [11].

Even though medical applications show a great potential, further research is required in order to compete with more established methods such as magnetic resonance imaging (MRI) or X-Rays.

1.3.2 Non-Destructive Testing

Evaluating the properties of different materials, as well as its defects, without compromising its utility and usefulness is the science known as Non-Destruc-

tive Testing (NDT). Different techniques can be used such as X-Ray as in the case of medical imaging, vibration analysis and can be as straightforward as simple visual inspection. Nevertheless by means of using terahertz radiation multiple new approaches and applications have been developed for evaluation and testing of different low-loss dielectric materials thanks to its penetration and imaging capabilities [12].

Even though terahertz NDT has been under research for quite a few years, recent events concerning the disaster of the space shuttle *Columbia* in 2003 have speed-up the race for obtaining feasible and reliable evaluation systems [13].

Non-destructive testing and evaluation with terahertz has a huge spectrum of interest fields such as the aforementioned material characterization, fatigue, crack, corrosion and flaw detection, but also on foodstuff with quality assessment [14] as well as detection of anomalies on processed food [15]. Other NDT applications, such as in arts, have been reported, as for example studying the underlying layers in paintings [16] or assessing the conservation requirements of historical pieces [17].

1.3.3 Safety, Security & Defense

Research on applications regarding safety, security and defense applications have shown a tremendous growth in the past few decades. Nevertheless, interest and thus initial research has been going on and off again from as early as 1920's. This cycle has been caused by the difficulty of working at the Terahertz gap (which will be described in the upcoming section) [18].

In the fields of safety, security and defense, three main goals have been pushing research and development in the Terahertz field. First of all, there has been a huge development in the field of personnel screening for both concealed weapon and explosive detection, to be used in public areas such as airports and public spaces [19]. On the other hand, great efforts have been carried out in explosive or chemical identification by means of spectroscopy in applications such as drug anti-smuggling in border patrol or security mail screening

[20]. Another security related hot topic is the use of terahertz waves for poor weather navigation, such as for terrestrial, air and nautical vehicle guidance in non-visibility situations where other techniques are not feasible such as in fog or heavy smoke [21].

Chemical Detection

The same properties which make the THz frequency range interesting in both astrophysics and earth science, as aforementioned in section 1.1 and 1.2, are also used for detecting and characterizing different material compounds. The transmitted and reflected THz spectrum of different materials contain absorption fingerprints characteristic to each material. Those fingerprints are caused by low frequency crystalline lattice vibrations (photon modes), hydrogen-bonding stretches and other intermolecular vibrations of molecules [22].

Drug detection As aforementioned, terahertz spectroscopy has the capability of determining the fingerprint of multiple chemicals and drugs. This feature can be used in pharmaceutical companies as a non-destructive testing for drug analysis and quality assurance [23].

Drug detection by means of non-destructing testing is also a must for border patrol agencies as well as mail screening for detecting smuggling or even consumption of illegal drugs [24]. Major efforts are being put into developing more portable hand-held systems capable of inspecting and analyzing drugs on the field without requiring large laboratory equipment [25, 26].

Explosive detection Different systems are under development for different types of threats. Mainly two systems are being developed for stowaway explosive detection on public places, such as airports, or for Improvised Explosive Device (IED) detection at stand-off distances greater than 5 m, considered as the minimum range for likely surviving an IED explosion without shrapnel (100 m may be required if shrapnel is present) [27]. In Fig. 1.1 examples of commonly used explosives fingerprint are shown for terahertz range spectroscopy.

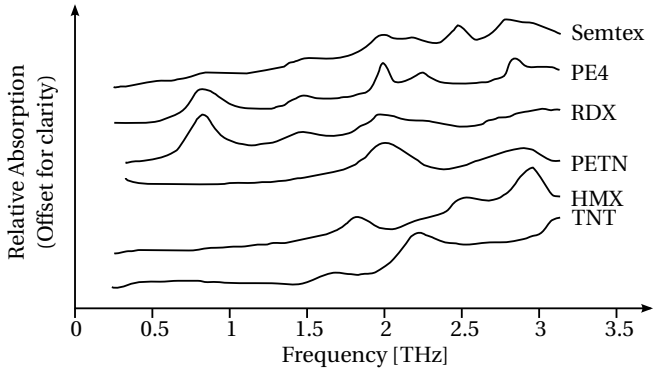

Figure 1.1: Terahertz absorption spectra of raw explosives Trinitrotoluene (TNT), High-velocity Military eXplosive (HMX), Pentaerythritol tetranitrate (PETN), Research Department eXplosive (RDX) and compound plastic explosive PE4 and Semtex H. Image adapted from [28]

Identification and characterization of different explosives is carried out by spectroscopy where raw samples, suspicious packages or envelopes can be tested. Either broadband pulsed or narrowband Continuos-Wave (CW) sources can be used to determine the fingerprints of the samples. Out of the lab equipment is commonly known as compact or portable THz systems. For more insight on such systems, the reader is pointed towards a spectroscopy review on defense applications in [22].

On the other hand personnel screening for IEDs at stand-off distances [29], have been commonly reported side by side under concealed weapon detection and will be introduced later on this section.

Poor Weather Navigation

Even though Infrared (IR) systems are commonly known for their use in night time imaging, they can also be used to image through mist, battlefield obscurants and smoke (to a certain extent), but have greater difficulties to penetrate through fog, clouds, light drizzle or even fire, which seriously attenuate IR radiation. In this scenarios, the atmosphere of the lower-end of the terahertz spectrum remains practically transparent [30, 31]. In military applications there is

a clear need for navigational aids and guidance systems that will allow navigation in poor weather conditions where both visual and/or infrared systems are compromised [32]. Terahertz systems do not attempt to replace actual guidance systems but to complement them. A comparison between millimetre-wave passive and infrared imaging is shown in [33] where complementary information can be obtained from using both instruments.

Furthermore terahertz imaging entail new possible applications in navigational imaging such as for example the ability to identify wires in the flight path of helicopters [34].

Concealed Weapon Detection

Possibly the most well known, as well as controversial, application of terahertz waves is the so called concealed weapon detection, also known as stand-off personnel screening or commonly “airport scanners”.

Concealed weapon detection can be classified in two similar applications: personnel screening portals and stand-off systems. Differences between systems are mostly characterized by the willingness of subject cooperation, which lead to different specifications for minimum stand-off distance and scan times [35].

The acquisition of personnel screening portals by worldwide homeland security departments, such as the Transportation Security Administration (TSA) of the United States of America (USA), for airport security has made this particular application one of the only few terahertz systems with a wide-spread commercialization.

Stand-off detection for use in military applications for screening unknown personnel at prudent stand-off distances from few meters up to 20 or even 100 meters has been the purpose of extensive research. Those systems are required to cope with the greater challenge of screening subjects at the required stand-off distances with sufficient resolution and scanning times. Even though promising results have been made, there is still no such system available for wide-spread use on the field, outside the academia or research groups.

Different imaging system architectures have been proposed and tested in either passive or active imaging schemes. In order to obtain appropriate spatial resolutions in stand-off screening, focusing elements are required. Since the wavelength can be quite small at terahertz frequencies, the aperture size of the focusing elements can be shown to be smaller or in the order of a meter [36, 37]. One of the main problems faced by stand-off imaging systems is the requirement of near-video-rate images which require either a huge number of receivers (not appropriate for heterodyne receivers), or mechanically scanning the subject by means of clever optics design, or a combination of both [38].

In passive terahertz imaging the natural emissivity of black body radiation, as well as the reflectivity from the sky, are used to obtain contrast between each element of an image. Even though enough contrast can be achieved in exterior scenarios, the increase in sky brightness in indoors settings makes it practically impossible to differentiate between different elements and objects since the dynamic range of temperatures is diminished to a few degree kelvin [32, 39].

On the other hand, active terahertz imaging by using coherent heterodyne detectors have shown outstanding image reconstruction capabilities through garment at significant stand-off distances up to 20 meters. One of the most astonishing systems as reported by Ken B. Cooper et al in [40] uses a ultra wide-band radar that can produce sub-millimeter three-dimensional images at stand-off distances at 600 GHz. By using direct measurements of reflectivity not enough contrast is obtained to identify objects under clothing, nevertheless by employing the Fast Fourier Transform (FFT) of the same data for each pixel, full information of each pixel can be obtained and thus the systems is capable of detecting multiple layers comprised of both clothes and skin, as well as possible objects thread lying below.

1.4 State of the Art in Terahertz Technology

1.4.1 Terahertz Sources and the Terahertz Gap

Although tremendous progress has occurred in different terahertz areas such as in receivers, both direct (incoherent) and heterodyne (coherent) detectors. In terahertz sources this effort has not yet provided the same progress.

It is an understatement that terahertz sources are among the greatest challenges for terahertz frequency engineers in order to obtain adequate power, frequency span and spectral purity.

Over the past several decades, space based instruments for astrophysics and science has been the sole purpose for the development of terahertz sources. Nevertheless the upcoming new set of applications has further pushed the interest for obtaining smaller and affordable sources.

Generating power at frequencies below 100 GHz is commonly carried out with oscillators, amplifiers, p-i-n diode comb generators and similar devices, all of them well-known in the radio-frequency field. Above 10 THz the availability of sources coming from the optical world comprises gas lasers, Quantum Cascade Lasers (QCLs) and other optical techniques.

At the terahertz gap, both radio-frequency and optical communities are trying to push their devices beyond their limits towards greater frequencies and wavelengths respectively. Nowadays, the most commonly used devices are solid-state based frequency multipliers driven by conventional microwave sources. Nevertheless, other technologies providing CW sources are rapidly emerging at terahertz frequencies such as high-electron mobility transitor (HEMT), heterojunction bipolar transistor (HBT) and Gunn-diode based fundamental and harmonic oscillators, as well as QCLs. Other technologies such as vacuum electronic devices (VEDs), comprised of backward-wave oscillators (BWOs), travelling-wave tubes (TWTs) and gyrotrons, amongst others, are able to produce large amounts of output power in exchange of poor beam quality, size and energy consumption. A more profound review on VEDs can be found in [41]. Photonic generation using photodiodes as optical down-converters has

become feasible as wideband sources with moderate power levels and high stability. This devices have started to become available for mid-budget terahertz instrumentation. A more comprehensive picture of the terahertz gap, and source availability can be found in Fig. 1.2.

Beyond 2 THz, QCLs have become popular where frequency multipliers are not available yet. Even-though recent development of frequency multiplier up to 2.7 THz may shift the use of QCLs towards upper frequencies, since QCLs require cryogenic cooling to achieve continuous wave operations, and have serious issues with frequency stability, tuning bandwidth and operation lifetime.

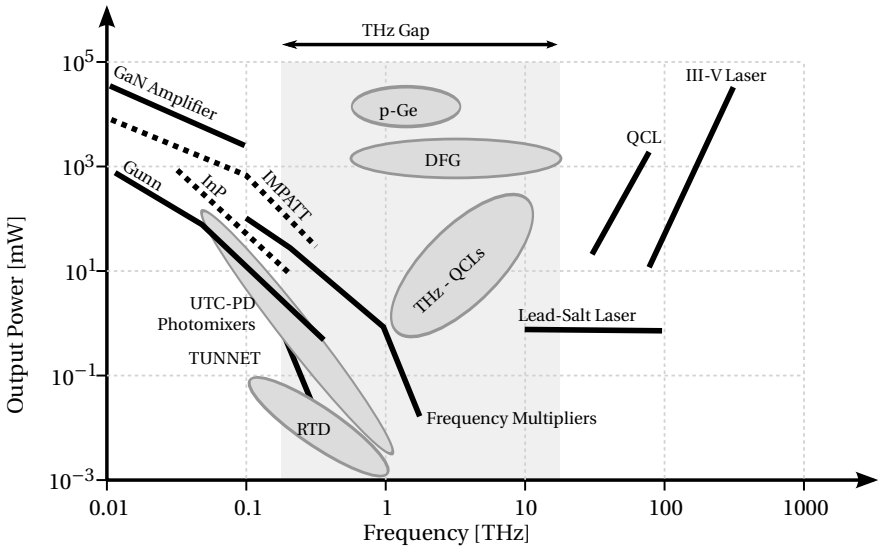

Figure 1.2: Terahertz available power for different source technology as a function of frequency. The majority of sources shown correspond to CW power at room temperature. QCLs, III-V lasers and DFG power correspond the peak power of pulsed sources. THz-QCL power is at cryogenic temperatures, as well as p-Ge laser [42].

Frequency Multipliers

In this thesis only solid-state CW sources are employed based on Active Multiplier Chains (AMCs).

AMCs based on planar Schottky diodes are a combination of amplifiers and frequency multipliers which enables a low-frequency signal, as generated with a general purpose microwave synthesizer, to be scaled in frequency up to the terahertz range [43].

Different multiplier configurations are used in order to obtain frequencies up to the current cutting-edge multiplier source at 2.7 THz reported in [44]. For a more extensive review on the state-of-the-art and future roadmap on solid-state broadband frequency-multiplied terahertz sources, the reader is referred to [45].

1.4.2 Terahertz Receivers

Even though sources are the most visible challenge in terahertz technology, equivalent effort has been made in order to obtain sensitive receptors at terahertz frequencies. Again, the driving force of millimeter and sub-millimeter wave receivers have historically been space and earth science applications [46].

Receivers, or sensors, can be broadly classified in two distinct types: heterodyne (coherent) detectors and direct (incoherent) detectors.

Coherent detectors preserve the information of both amplitude and phase of the electromagnetic field with high sensitivity only limited by quantum noise. There are three major mixer technology contenders for terahertz heterodyne detection. The particular choice is dictated by the availability of local oscillator power, the receiver sensitivity criteria, and the choice of operation temperature. In the following section a review of the current state-of-the-art is evaluated for Superconductor Insulator Superconductor (SIS), Hot Electron Bolometer (HEB) and Schottky mixers.

On the other hand incoherent detectors are based on sensing material changes produced by the absorption of photons from the electric field. As a consequence of their inherently large detection bandwidth, a large number of high-resolution instruments have been based on this type of receivers [47].

Heterodyne Receivers

In heterodyne or coherent receivers the desired high-frequency signal is down converted to an Intermediate Frequency (IF) over a limited bandwidth, which at terahertz frequencies is commonly in the order of a few up to tens of GHz.

The down conversion effect is performed by "beating" two different but close-by frequencies inside a non-linear device known as *mixer*. By using this device, the sum and difference frequencies, as well as multiples of them, are created between the incoming signal and some synthesized wave known as the Local Oscillator (LO).

Heterodyne receivers are optimized for the detection of the difference frequency, occurring at a fraction of the beating frequencies, typically at a few GHz for a terahertz receiver.

A common coherent receiver is composed of two basic subsystems known as the front and back-end. The front-end deals with the terahertz radiation, and is basically composed of the required quasi-optical elements, or antennas, which drive the incoming signal towards the mixer. The LO can be coupled by means of a quasi-optical system configuration as used in large antenna receivers [48], or directly coupled inside the mixer structure, for example in waveguide technology as commonly used by solid-state mixers [49].

The back-end of the receiver conditions the IF signal with amplifiers and filters before delivering the signal to the acquisition system, which could be composed of an Analog-to-Digital Converter (ADC), power detector or spectrometer depending on the end application [50].

The SIS Mixer

The most commonly used devices for high-end applications, where budget is not quite the limiting factor, are the superconductor – insulator – superconductor (SIS) mixers, which have demonstrated an outstanding performance for frequencies up to 1.5 THz [51], requiring low LO powers. Even though SIS mixers have the best sensitivity as compared to other heterodyne technologies, their use is limited by the requirement of expensive cryogenic cooling systems which

need to provide a temperature low enough for the device to operate in its superconducting state below 4°k. Furthermore above 1.2 - 1.5 THz the noise of the device greatly increases, reducing the sensitivity and thus the benefits of using this technology amongst others.

Examples of instruments using SIS mixer technology can be found inside the spatial observatory Herschel, where the Heterodyne Instrument for the Far Infrared (HIFI) is located. HIFI carries five SIS mixer which cover the spectrum from 480 to 1150 GHz [52]. Also SIS mixers can be found in several cartridges of the ALMA spatial observatory, as for example cartridge number 10 with a working range from 795 to 950 GHz [53]. The use of SIS mixers in imaging applications is not a widespread subject since their limitations are incompatible with wide-spread commercial use, even though some experiments have been carried out such as in [54]. A more complete review on superconducting receivers for astrophysics can be found in [55].

The HEB Mixer

HEB mixers are thermal detectors, and as such can be used as square-law mixers. A conventional bolometer, commonly used for measuring the energy of incident electromagnetic radiation, consists on an absorptive element, such as a thin layer of metal, connected to a heat sink (a body of constant temperature) through a thermal link. As a result, any radiation impinging on the absorptive element raises the temperature above that of the heat sink, which can then be measured with a thermal sensitive device [56]. A simple diagram of a bolometer is shown in Fig. 1.3.

As with SIS mixers, the operation of HEB mixers relys on the properties of a thin layer of superconducting material (commonly Niobium Nitride (NbN)). In a HEB mixer a thin superconducting micro-bridge interconnects two thick metal pads used as heat sinks. The superconductor bridge serves as both the absorber and thermometer as compared to the common bolometer. HEBs are a type of Transition Edge Sensor (TES) that means that the device is operated on the boundary between metal and semiconductor where the change in temper-

ature, as a result of the incident field absorption, results on a greater resistance change and thus a enhanced sensitivity [57]. An important feature of HEB mixers is that they require small amounts of LO power, which can be as low as 30 nW depending mainly on the size of the superconducting bridge [58].

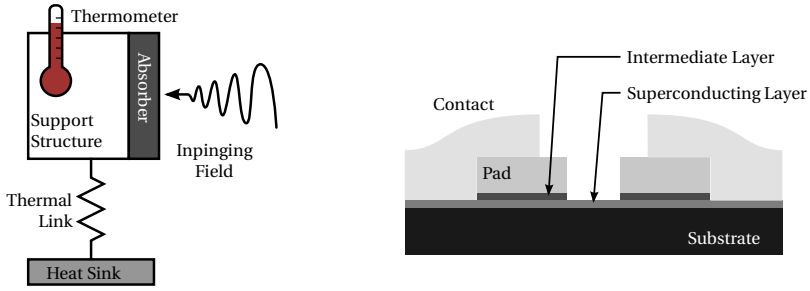

Figure 1.3: Simple diagram of (a) common bolometer and (b) Hot Electron Bolometer (HEB). The HEB is based on an antenna coupled mixer where the contacts are directly the antenna metal strip contacting the HEB pad usually both made from aluminum or gold. The superconducting microbridge (usually NbN) is shown to go underneath the metal pads, where an intermediate superconducting (NbTiN) layer is optionally placed to improve the noise temperature of the device. Finally the whole device is supported by a silicon substrate. Images are based on [57] and [59] respectively.

Unlike SIS mixers, HEB mixers have been used in imaging for concealed weapon detection obtaining state-of-the-art images in near-video frame rates. HEBs have commonly been reported in combination with small printed twin-slot antennas up to 3.1 THz [60] or spiral antennas up to 4 THz [61] (as depicted in Fig. 1.4). Nevertheless, its main applications have been in space and earth science, used for example in the high-range of the HIFI instrument, specifcally on bands 6 and 7 (1.4 - 1.9 THz) using NbN hot-electron bolometer HEB mixers with a LO power between 5 and 50 μW [62].

The Schottky Mixer

In Schottky diode mixers, the incoming signal is mixed with the LO signal by the non-linear I-V relation of the barrier Schottky diode. A more in-depth introduction to Schottky diodes is carried out in page 18, where Schottky-diode

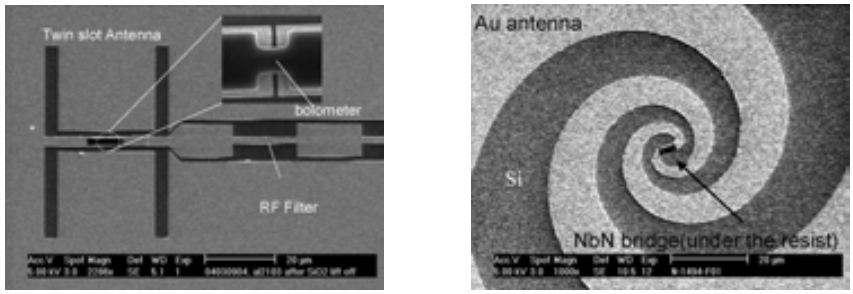

(a) (b)

Figure 1.4: Antenna coupled HEBs for (a) Twin-Slot and (b) Spiral antenna, extracted from [58].

based detectors are discussed. Even-though the working basis is the same as with lower frequency mixers, the technological problems to overcome in these particular frequencies are quite challenging. Schottky mixers in the low-end of the terahertz range have been usually mounted on waveguide structures, while new advances in micro-machining techniques allow Schottky mixers to be integrated in silicon substrates [49]. Heterodyne receivers based on planar Schottky diodes are the most appropriate for long life, particularly since they operate at room temperature, and can be used in instruments up to 2.5 THz [63], for example the HIFI instrument on the Herschel spacecraft, as mentioned in previous sections, was launched on 14 May 2009 and during the writing time of this dissertation, the helium feeding both SIS and HEB mixers cooling systems was depleted, in the forecasted EOHe (End-of-Helium) event on 29 April 2013 [64]. For a more comprehensive and historical review on GaAs Schottky Diodes for mixer applications the reader is encouraged to look further into [65].

In the present time the most commonly used Schottky based mixer are based on the sub-harmonic architecture with balanced anti-parallel diode pair configuration. Sub-harmonic mixers with similar performance to fundamental mixers have been greatly reported in the literature, since they provide some advantages such as more compact receivers, they require one less multiplication stage on AMCs and thus result in a cost reduction, moreover a greater RF and IF bandwidth in detriment of overall sensitivity and the requirement of even

more LO power, this time in the order of mW [66].

Mixer comparison

The most commonly used method to compare between mixer performance is by using either its single-sideband (SSB) or double-sideband (DSB) noise temperature depending on the mixer operation. It is important to note that the minimum theoretical noise, as stated by the Heisenberg uncertainty principle, of SSB or DSB mixers (as well as for amplifiers) is limited by quantum noise and therefore it will be lower bound by either $h^3 f/k^4$ for SSB and $hf/2k$ for DSB operation [67]. In Fig. 1.5, a slightly outdated (2006) data comparison on the DSB noise of current deployed Schottky, HEB and SIS mixers is shown. As aforementioned, while SIS mixer report the lower noise for the low-band of terahertz ($\sim 30^{\circ}$K at 300 GHz), HEBs are used in the upper-band. Schottky detectors with lower cooling temperatures can be designed in the whole band in expense of greater noise temperatures.

Direct (Incoherent) Receivers

Heterodyne receivers are well suited for high-resolution spectroscopy, nevertheless their sensitivity to broadband continuum radiation is compromised by their relatively limited IF bandwidth. On the other hand, direct detectors such as Schottky diode based detectors or bolometers offer very wide bandwidths [68].

The Schottky Diode

Whereas the classical *pn* junction diode commonly employed at low frequencies has a large junction capacitance that makes this type of diodes impractical for high-frequency applications, even at frequencies lower than Terahertzs. The Schottky barrier diode, relies on a semiconductor-metal junction instead

[3] h: Planck constant = $6.62606957 \cdot 10^{-34}$ m^2 kg / s
[4] Boltzmann constant $1.3806488 \cdot 10^{-23}$ m^2 kg s^{-2} K^{-1}

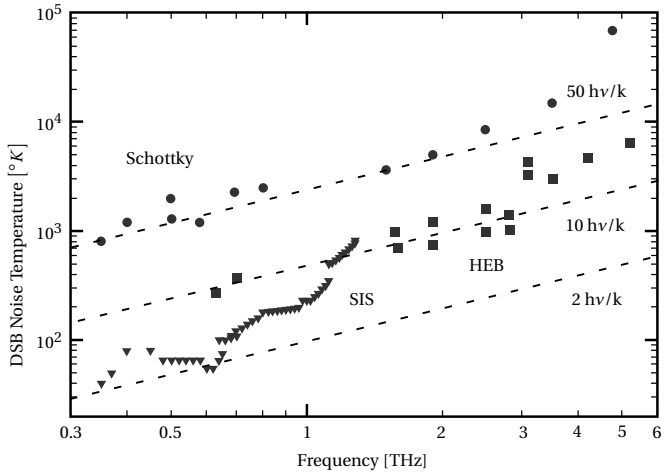

Figure 1.5: Mixer comparison by means of DSB noise temperatures of Schottky diode mixers (circles), SIS mixers (triangles) and HEB mixers (squares). The image is based on 2006 data as reported in [50].

of a N-type/P-type doped semiconductor as used with common diodes. Whereas *pn* junction diode current flow involves both electron and hole carriers, in a Schottky diode metal-semiconductor junction only one type of carriers are used based on the doping of the semiconductor material. In Schottky diodes, when the metal is placed into contact with an n-type semiconductor, electrons diffuse out of the semiconductor into the metal, which leaves the region under the metal contact free of electrons (known as the *depletion layer*), this process continues until the semiconductor is so positive that no more electrons are able to go into the metal. The depletion layer is then formed by donor atoms positively charged, since they have lost its excess electron, which makes the semiconductor positive with respect to the metal. The voltage difference between the metal and the semiconductor is known as the *contact potential* and in Schottky diodes is in the range of 0.3 to 0.8 V. When a positive voltage is applied to the metal, the internal difference is reduced, and thus electrons can flow again into the metal. As compared to common *pn* junction diodes, there is no delay effect due to charge storage and thus removing the voltage stops

the current almost instantly. Reverse voltage can be established in only a few picoseconds, which accounts for the important role of Schottky diode in microwave mixers and detectors [69]. The semiconductor-metal junction results in a much lower junction capacitance and thus an increase on the cutoff frequency of the device, as shown in the introduction devices based on Schottky diodes, are reported up to a few THZ.

This characteristic makes them ideal to use primary for applications involving the three basic frequency conversion operations of *rectification* (conversion to DC), *mixing* (frequency down-conversion) and the most important operation in our case, *detection* (demodulation of an amplitude modulated signal).

Schottky model

The Schottky diode can be simply modelled as a non-linear resistor [70], with a small-signal V-I relation expressed as

$$I(V) = I_S\left(e^{\alpha V} - 1\right) \tag{1.1}$$

where $\alpha = q/nkT$, and q is the charge of an electron, k is the Boltzmann's constant, T the physical temperature of the device, n the ideality factor, and I_s the saturation current. Schottky diode common values for the ideality factor is 1.2 and for I_s ranges between 10^{-6} to 10^{-5} A, and thus α can be shown to be approximately 1/(25 mV) for a standard room temperature of 290°K. The typical V-I relation of a Schottky diode is shown in Fig. 1.6 (a).

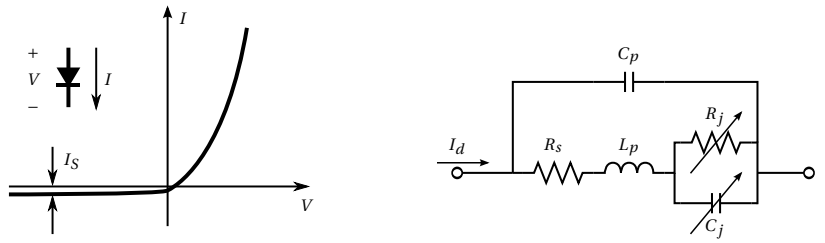

(a) (b)

Figure 1.6: (a) V-I relation and (b) equivalent AC circuit model for a common Schottky diode.

Small-signal approximation

By using the small-signal approximation, voltage on the diode is shown to be

$$V = V_0 + v \tag{1.2}$$

where V_0 is the DC biasing voltage and v is a small superimposed AC signal. By expanding (1.1) into its Taylor series at V_0 it leads to

$$I(V) = I_0 + v \left.\frac{dI}{dV}\right|_{V_0} + \frac{1}{2} v^2 \left.\frac{d^2 I}{dV^2}\right|_{V_0} + \cdots \tag{1.3}$$

where $I_0 = I(V_0)$ is the DC bias current. By evaluating the derivatives, equation (1.3) can be rewritten as the sum of the DC bias current and other terms corresponding to the AC current.

$$I(V) = I_0 + vG_d + \frac{v^2}{2} G_d' + \cdots \tag{1.4}$$

where $G_d = 1/R_j$ is the dynamic conductance of the diode which defines R_j, the junction resistance of the diode. The three-term approximation in equation (1.4) is the so called small-signal approximation, it shows that the equivalent circuit of the diode involves a non-linear resistance. However, in practice, the AC characteristics of a diode also involve reactive effects due to its own structure, as well as the packaging of the diode, which is of out-most importance as operation frequency increases, the common model is shown in Fig. 1.6 (b). First of all, the leads and contacts of the diode package involve a series inductance L_p and a shunt capacitance C_p. The series resistor R_s accounts for contact and current-spreading resistance. The junction is modelled as a bias-dependent conductance C_j and resistor R_j [71].

Diode rectifier and detector operation

Diodes for rectifier applications are used to convert a fraction of an RF signal to DC power. They are currently used in a wide number of applications involving power monitoring, automatic gain control circuits, and signal strength

indicators. If the diode voltage consist on DC bias signal plus a small-signal RF voltage at a single frequency,

$$V = V_0 + v_0 \cos \omega_0 t \tag{1.5}$$

then from equation (1.4) the current in the diode can be shown to be

$$I = I_0 + \frac{v_0^2}{4} G_d' + v_0 G_d \cos \omega_0 t + \frac{v_0^2}{4} G_d' \cos 2\omega_0 t \tag{1.6}$$

where I_0 is the bias current and the second term $\left(v_0^2 G_d'/4\right)$ corresponds to the DC rectified current. It is important to note that other AC signals of frequencies ω_0 and $2\omega_0$ as well as higher-order harmonics are present on the signal, but can be filtered out by using a low-pass filter.

In order to quantify the power conversion of the device, a *current sensitivity* γ_i is defined as a measure of the change in DC output current for a given RF input power. While the power of the RF input can be shown to be, by using only the first term in equation (1.4) $v_0^2 G_d/2$, the change in DC output current is $v_0 G_d'/4$ as shown in eq. (1.6).

$$\gamma_i = \frac{\Delta I_{DC}}{P_{in}^{RF}} = \frac{G_d'}{2G_d} \qquad \left[\frac{\mathrm{A}}{\mathrm{W}}\right] \tag{1.7}$$

The sensitivity is commonly expressed as the open-circuit voltage γ_v, which can be defined in terms of the voltage drop across the junction resistance when the diode is open-circuited. Typical values for this voltage sensitivity are 400 to 10000 mV/mW.

$$\gamma_v = \gamma_i R_j \qquad \left[\frac{\mathrm{V}}{\mathrm{W}}\right] \tag{1.8}$$

By employing the diode as a detector, the non-linearity of the device is used to demodulate an amplitude modulated carrier signal. This time varying voltage in the diode can be expressed as

$$v(t) = v_0 (1 + m \cos \omega_m) \cos \omega_0 t \tag{1.9}$$

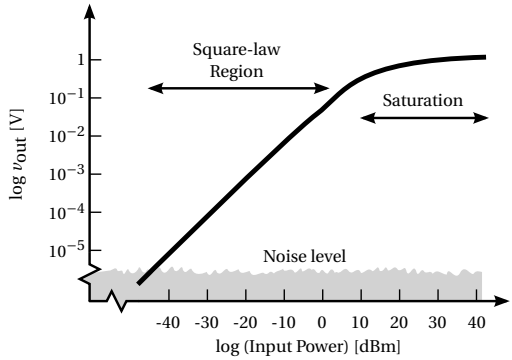

Figure 1.7: Typical detected output voltage versus input power characteristic for a conventional Schottky diode.

where m is defined as the modulation index ($0 \leq m \leq 1$) and ω_m is the modulation frequency.

By using this voltage in the small-signal response from equation 1.4, the time varying diode current for the detector can be shown to be

$$\begin{aligned} i(t) \quad = \quad & v_0 G_d \left[\cos\omega_0 t + \tfrac{m}{2}\cos(\omega_0+\omega_m)\,t + \tfrac{m}{2}\cos(\omega_0-\omega_m)\,t\right] \\ & + \tfrac{v_0^2}{4} G'_d \left[1 + \tfrac{m^2}{2} + 2m\cos\omega_m t + \tfrac{m^2}{2}\cos 2\omega_m t + \cos 2\omega_0 t \right. \\ & + m\cos(2\omega_0+\omega_m)\,t + m\cos(2\omega_0-\omega_m)\,t + \tfrac{m^2}{2}\cos 2\omega_0 t \\ & \left. + \tfrac{m^2}{4}\cos 2(\omega_0+\omega_m)\,t + \tfrac{m^2}{4}\cos 2(\omega_0-\omega_m)\,t\right] \end{aligned} \tag{1.10}$$

Even-though the resulting spectrum of demodulation is rich in spectral terms, with both linear and non-linear voltage dependence, the desired demodulated output of the ω_m frequency can be easily separated from the other components by a low-pass filter. By observation of the demodulated term $\left(m v_0^2 G'_d/2\right)$, the amplitude of the current is shown to be proportional to the power of the input signal, phenomenon known as the *square-law* behaviour which is the usual operating condition of diode detectors, but it is only valid over a restricted range of input powers. The operating range for the diode to operate as a detector is limited in low RF powers by the noise floor of the device, the bandwidth of the video amplifier and its noise level.

For high input RF powers (greater than -15 dBm on most common devices),

the small-signal condition does not hold true and the behaviour of the device saturates, first to a linear and then to constant value. Fig. 1.7 shows the typical output detected voltage (v_{out}) versus input RF power characteristic.

Square-Law Region Bounds

As mentioned before, the square-law region is bounded both in low and high input powers. There is a point when the input RF power is so small that the output of the detector is masked by its own noise and thus it is said to be noise-limited. Noise of the detector can be quantified by its Noise Equivalent Power (NEP), although this is used throughout the frequency spectrum, commonly another parameter is used to discuss the quality of a detector, known as the Tangential Signal Sensitivity (TSS). Since other types of noise characterizations such as TSS are not feasible due to the non-linear behaviour of the diode, commonly the performance of the systems with respect to the noise is described by means of the minimum input RF signal which produce a required signal-to-noise ratio at the output of the detector, as measured in the whole bandwidth of the detector itself [73]. In order to obtain a measurement of the TSS, first the

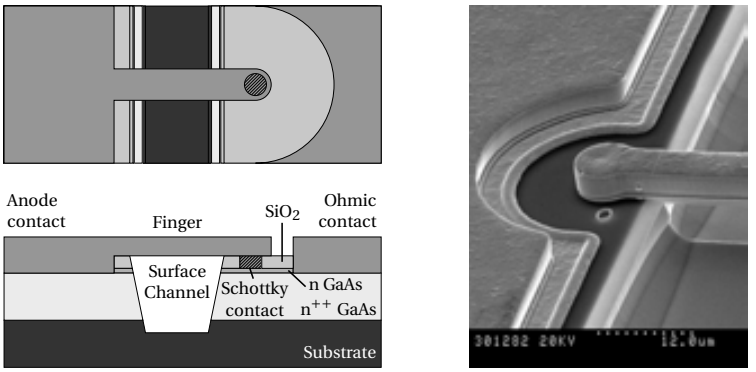

Figure 1.8: Left: Diagram of a planar Schottky diode with finger structure, image based on [72, 50]. Right: SEM image of an actual Schottky diode finger of a commercial zero-bias detector from *Virgina Diodes Inc.* (VDI).

detector noise is measured by switching off the input RF signal. By taking an appropriate number of measurements, then the RF signal is switched on and slowly increased until the top of the previously measured noise matches the bottom of the RF signal noise. This value can be shown to correspond to an actual SNR of 8 dB.

Commercially available Schottky detectors based on GaAs are available with sensitivities ranging from 4000 V/W at 100 GHz up to 300 V/W at 1.5 THz [74], in Fig. 1.8 a diagram of an actual W-Band diode and its actual SEM picture are shown for a commercial Schottky diode.

1.5 Millimeter-Wave Imaging

The main focus of this thesis is the study of imaging techniques for applications at microwave and millimeter-wave bands. This section positions the dissertation among the different existing techniques.

Imaging with radio frequency waves is usually classified in Passive or Active imaging, based on the nature of the architecture used to sense or measure the field which will compose the image.

1.5.1 Passive Imaging

Imaging systems based on spatial incoherent waves, are based on radiometric systems, which are able to sense difference in the brightness temperature of black-body emitted radiation or reflected radiation from the sky (or any other given incoherent source).

Different constraints must be taken into account if using a radiometer indoors or outdoors, since different dynamic range are required in each scenario. For instance, on an outdoor scene the sky temperature is about 60°K, while an effective human body temperature of 285°K can be stated, thus for example providing a total contrast of 225°K between the human body and a perfect reflective object such as a metal knife or gun, which reflects the totality of the sky temperature. On an indoor scenario, an average room temperature of 295°K

can be assumed, with an effective human temperature of 310°K, thus obtaining a contrast of only 15°K. Artificial non-coherent sources are being used to increase the contrast on indoor scenarios. However, those devices are still expensive and far away from being a real solution for any wide-spread application.

Radiometry requires bigger bandwidths and huge amplification in order to compensate for small emitted or reflected power, as well as big antennas to collect as much radiated energy as possible. However, using non-coherent imaging brings two important benefits, first of all, there is no need to radiate the subject under test, since the system is sensing both the subject own emission and/or the actual reflection from its environment (provided that no incoherent source is being used). On the other hand, the spatial incoherence nature of this measurement makes the system robust versus multipath, reflections and interference.

1.5.2 Active Imaging

Active imaging systems always require the target under test to be illuminated, thus providing an improved dynamic range over the non-coherent system. However, small deviation on the illuminating wave path result in speckle noise, polluting the image which usually requires some additional processing after the recovering process.

Multiple types of imaging system using coherent waves have been reported, the most known technique is probably the Frequency Modulated Continuous Wave (FMCW) radar, which provides high resolution images over long distances as demonstrated in [75]. This technique has been widely used for earth studies in remote sensing applications, and nowadays is one of the most wide-spread commercialized products in millimeter-wave applications thanks to its usage on automotive crash detection systems.

One of the characteristics of active imaging is the requirement of a radiating source that illuminates the target. By taking into account our previous discussion in section 1.4.1, only limited power and frequency span are available at

terahertz frequencies. Thus, active imaging systems tend to be frequency range limited, or even single frequency, as is the case with the techniques used in this dissertation.

Monochromatic techniques such as phase-retrieval or holography are active systems based on recovering the image of an illuminated target by means of using intensity-only measurements. These techniques acquire the intensity usually by employing direct detection receivers as the aforementioned Schottky based detectors. Once the amplitude and phase of the field are recovered, the image is focused by means of propagating the unfocused image at the target plane. Aforementioned methods are often single frequency techniques which can be enhanced by using multi-tone approaches which unlock the acquisition of better images, or improved depth information over the more basic single tone approach. Monochromatic single-tone measurements have been mostly used to characterize large antennas reflectors.

1.5.3 Holography

First known as *wavefront reconstruction* and later as *holograph* (from ancient greek *hólos* "whole" and *grafein* "writing" or "drawing"), the idea was conceived by Dennis Gabor while working towards improving the resolution of electron microscopes in 1947, for which he received the novel prize in 1971 [76]. Gabor theorized that when a suitable coherent reference wave coexisted simultaneously with light diffracted by (or scattered from) an object, information of both amplitude and phase could be recovered from intensity (power-only) measurements, showing that from this measurements the wavefront propagated by the object could be fully reconstructed.

Holography became widely used in optics when the development of the laser in 1960 provided a convenient coherent optical source. As coherent microwave sources were available well before then, introduction of holography in the microwave field was actually carried out beforehand in 1951 [77]. However, the widespread application of microwave holography did not take place until a few decades later by taking advantage of work in optics [78].

The main disadvantages of optical holography in the early days were the absence of coherent illumination sources (until the invention of lasers), and the intrinsic theoretical problem known as the twin-image problem. This twin-image translates into a superposition of both the desired image term and its conjugate, also known as the virtual image.

It was not until early 1960s when E.N. Leith and J. Upatnieks [79], workers of the University of Michigan's Radar Laboratory, found the similarity of holography to the synthetic-aperture-radar (SAR) problem and suggested a modification that greatly improved the holographic process with the later known *Off-Axis* or *Leith-Upatnieks* holographic technique.

Other techniques have been used to reduce the twin-image problem, such as *In-Line* holography, first introduced in 1951-56, by Goss and Gabor himself [80].

The application of holographic techniques have had a major importance not only in the optical world, with three dimensional images, credit card security systems and military head-up displays (HUD) among others, but also in acoustics with shock wave visualization, resonances in musical instruments etc., not forgetting other fields such as the study of earthquake seismic waves or the huge range of possible applications in the field of microwaves and its use in terahertz, where it has been used for diagnosis and testing of big reflectors through Fresnel field measurements [81], as well as obtaining far field antenna patterns [82]. Other not so widespread uses have been aerial mapping of geographical areas [83], detection of defects and anomalies in dielectric structures [84] and in security application by means of metal detection in dielectric bodies [85].

1.6 Objectives

The main objective of this thesis is to explore the viability of microwave and millimeter-wave imaging systems based on intensity-only holographic techniques. This dissertation is mostly focused on the Off-Axis holography tech-

nique. Not only from a theoretical perspective but specially from an actual implementation standpoint.

In order to do so, different experimental setups and devices will be designed and manufactured. Iteration between hardware and software has created a framework for devising and testing different imaging techniques under consideration. The frequency range W-Band has been chosen as the main goal for all systems under study, however different setups will first be constructed, characterized and tested at X-Band in order to build up the expertise required to work at millimeter-wave frequencies.

Therefore the main objectives of this dissertation can be summarized as:

- Revisit and explore the viability of Off-Axis Holography for image acquisition.
- Design, manufacture and construction of a two-dimensional scanner for Off-Axis holography to be used in different setups and configurations.
- Test and validate different improvements over the used techniques.

1.7 Outline of the Dissertation

Chapter 1 introduces the fundamentals of Terahertz radiation, as well as the state of the art on Millimeter-wave technology. An important emphasis has been made to review the most fundamental background and most commonly used devices for Millimeter and Sub-millimeter wave systems. In the chapter, a list of the scientific contributions is also presented.

In Chapter 2, the principles of imaging theory used throughout the dissertation are introduced. Scalar Diffraction Theory is linked with an introduction to the Plane Wave Spectrum, followed by a brief introduction to Quasioptical propagation by Gaussian Beams, and the actual theory of Holography and the imaging technique Off-Axis Holography.

Chapter 3 uses the aforementioned theory to simulate, design and manufacture an imaging array at X-Band, which is used in both a Cartesian and Cir-

cular scenario. The simulation of the whole system is presented, along with the whole design process of the individual element receiver and the measurement setup and experimental results.

Chapter 4 introduces two improvements over the more classical holographic approach by adding a second measurement shifted 180° and the ability to programatically shift the phase of the reference wave used in the holographic progress. As in the previous chapter, the simulation, design and manufacture of the receiver is shown, followed by the experimental setup and measurement results.

In Chapter 5, further microwave and millimeter-wave experiments are shown that complete the acquired knowledge of the imaging process through the use of different setups and techniques, giving a deeper view of what can actually be accomplished with different methods, using actual measurements as the main vehicle to drive the conclusions.

Finally, Chapter 6 of this dissertation ends with a summary of the conclusions drawn through all the dissertation, and future work.

1.8 Scientific Contributions

This dissertation collects the work that has been carried out during the Ph.D. Most of the results have been published in international or nationaol conferences. Some results are still pending publication. Here follows a list of the contributions:

- Marin, J. and Parron, J. and de Paco, P., "In-line hologram with synthesized opposite-phase internal reference", Antennas and Propagation Society International Symposium (APSURSI), 2013 IEEE.

- Marin, J. and de Paco, P., "Autocorrelation removal by phase-shifted reference in off-axis Gabor holography", 7th European Conference on Antennas and Propagation (EuCAP), 2013.

- Marin, J. and De Paco, P., “Rotary array imaging system by means of Gabor’s Holography”, IEEE MTT-S International Microwave Workshop Series on Millimeter Wave Integration Technologies (IMWS), 2011

- Camarero, R. and Marin, J. and Menendez, O. and De Paco, P., “On designing a W-band active coherent array”, IEEE MTT-S International Microwave Workshop Series on Millimeter Wave Integration Technologies (IMWS), 2011.

- Marin, J. and De Paco, P., “X-Band rotary array imaging system by means of Gabor’s Holography”, 41st European Microwave Conference (EuMC), 2011

- J. Parron, P. de Paco, G. Junkin, J. Marin, O. Menendez, “Design of a W-band Quasi-Optical Measurement System”, XXV Simposium Nacional de Unión Científica Internacional de Radio (URSI), Bilbao, Spain.

- A. Broquetas, J. Romeu, Ll. Jofre, A. Aguasca, M. Alonso, J. Abril, E. Nova, M. Lort, J. Parrón, P. De Paco, G. Junkin, J. Marín, “TeraSense: 94 GHz short range real-time camera”, XXIX Simposium Nacional de Unión Científica Internacional de Radio (URSI), Valencia, Spain, 2014.

- A. García, M. Barba, E. González, J. Gutiérrez, J. Montero de Paz, J. Parrón, J. Romeu, P. de Paco, J.A. Encinar, L.E. García, B. González, E. Nova, R. Vera, K. Zeljami, A. Badolato, J.L. Besada, T. Fernández, J. Fierrez, J. García, J.M. Gil, M.A. González, J. Grajal, G. Junkin, C.A. Leal, J. Marín, B. Mencía, Ó. Menéndez, J.R. Montejo, J. Ortega, J.E. Page, J.P. Pascual, G. Pérez, J.M. Rebollar, Ó. Rubiños, J. Rubio, J.A. Ruíz, D. Segovia, A. Tazón, J. Zapata, “TeraSense: THz Device Technology Laboratory. Final Summary”, XXIX Simposium Nacional de Unión Científica Internacional de Radio (URSI), Valencia, Spain, 2014.

- A. Broquetas, J. Romeu Robert, Ll. Jofre, M. Alonso, J. Abril, E. Nova, A. Aguasca, D. Varela, J. Parrón, P. de Paco, G. Junkin, J. Marín, “TeraSense:

94 GHz Short Range Real-Time Camera", XXVIII Simposium Nacional de Unión Científica Internacional de Radio (URSI), Santiago de Compostela, Spain, 2013.

- A. García, J. Gutiérrez, J. Montero-de-Paz, J. Parrón, J. Romeu, R. Vera, P. de Paco, L.E. García, B. González, M. Moreno, E. Nova, K. Zeljami, A. Badolato, J.L. Besada, T. Fernández, J. Fiérrez, J. Grajal, G. Junkin, J. Marín, B. Mencía, O. Menéndez, J. Ortega, J.P. Pascual, O. Rubiños, D. Segovia, A. Tazón, "TeraSense: THz Device Technology Laboratory", XXVIII Simposium Nacional de Unión Científica Internacional de Radio (URSI), Santiago de Compostela, Spain, 2013.

- G. Junkin, J. Marin, "Near-Field Phase Retrieval for Terahertz Applications using NVIDIA CUDA", PUMPS Summer School (Programming and Tuning Massively Parallel Systems), Barcelona, Spain, 2012.

- J. Marin, G. Junkin, P. de Paco, "Rotary array imaging system by means of Gabor holography (Spanish: Sistema de Imagen con Array Rotatorio Mediante Holografía de Gabor)",XXVI Simposium Nacional de Unión Científica Internacional de Radio (URSI), Madrid, Spain 2011.

- J. Marin, G. Junkin, P. de Paco, J. Parrón, "Millimeterwave Images by Means of Gabor Holography (Spanish: Imgenes en banda milimérica mediante holografía de Gabor)", XXV Simposium Nacional de Unión Científica Internacional de Radio (URSI), Bilbao, Spain 2010.

Other contributions whose content is not related to this thesis:

- Gemio, J., Parrón, J., de Paco, P., Junkin, G., Marin, J., & Menéndez, O, "A split-ring-resonator loaded monopole for triple band applications", Journal of Electromagnetic Waves and Applications, 24(2-3), 241-250, 2010

- de Paco, P., Menendez, O., & Marin, J. "Dual-band filter using nonbianisotropic split-ring resonators", Progress In Electromagnetics Research Letters, 13, 51-58, 2010.

- J. Marin, P. de Paco & O. Menéndez, “Multi-Constellation and MultiFrequency Receiver Front-End for satellite navigation systems Galileo and GPS” (Spanish: Cabecera de recepciń multifrecuencia para los sistemas de navegación por satélite Galileo y GPS)”, XXIV Simposium Nacional de Unión Científica Internacional de Radio (URSI), Santander, Spain 2009.

CHAPTER 

THEORETICAL BACKGROUND

The objective of this chapter is to introduce the reader to the different theories used throughout the dissertation, leading in the final of the chapter to the introduction of Off-Axis Holography. Multiple approaches to solving both propagation and diffraction will be introduced, each one of them serving a different purpose on computation for either simulation or measurement manipulation. A brief introduction to propagation and diffraction by means of the most usual way of introducing Fourier Optics theory is presented by solving the Helmholtz equation using Green's function. However, a second approach based on the angular spectrum of plane waves will also be presented for solving both propagation and diffraction in a much more convenient way for our final purpose, the recovering of images through Off-Axis holography. One last propagation theory, based on a paraxial approximation is presented by means of the Quasi-Optical theory, where the use of Gaussian beams are taken into consideration, which in this dissertation are going to be used mainly for high-directivity antenna field propagation. Finally, by using some of the concepts introduced for

Fourier Optics, Off-Axis holography is introduced.

2.1 Scalar Diffraction Theory

Fourier Optics by means of the Scalar Diffraction Theory is a common link between optics and radio-frequency. While the former field uses geometrical optics to provide a proper solution to light propagation on scenarios much greater than the wavelength, the later uses Maxwell's equations in order to describe the behaviour of radio-frequency waves. Both fields using different approaches to the same problem are linked with the Scalar Diffraction theory when both ends try to cope with bigger problems, in the case of the radio-frequency field, or fewer (or bigger) wavelengths in the case of optics.

The main problem to solve by Fourier Optics is diffraction. The term diffraction was defined by Sommerfeld as "any deviation of light rays from rectilinear paths which cannot be interpreted as reflection or refraction". Diffraction is caused by the confinement of the lateral extent of a wave, and is most appreciable when the aperture of the confinement is comparable to the wavelength of the radiation.

The study of the Scalar Diffraction theory in this section starts directly with the *Helmholtz equation* as derived directly from Maxwell's equations. Its derivation can be found in either the reference book *Introduction to Fourier Optics* by Joseph W. Goodman [86] as well as on *Advanced Engineering Electromagnetics* by Constantine A. Balanis [87], those two references are the main basis for this section mathematical background, the reader will be referred to them to look for additional information.

In order for Scalar Diffraction theory to hold true, some considerations must be defined for the wave propagating medium. The medium should be linear, it must satisfy the linearity properties of superposition and scaling. The medium must be isotropic, its properties must be independent of the direction of polarization of the wave. The medium must be homogeneous, the permittivity must be constant throughout the region of propagation. The medium

must be non-dispersive, the permittivity must be independent of wavelength over the wavelength region occupied by the propagating wave. And finally, the medium must be non-magnetic, which means that the magnetic permeability must be always the vacuum permeability (μ_0). By taking this into consideration, all components of the electric and magnetic field in Maxwell's equations are uncoupled, thus behaving identically, with their behaviour described entirely by a single scalar wave equation. This is the main requirement for the Scalar Diffraction theory and Fourier Optics.

This may not hold true when boundary conditions are imposed on a wave that propagates in a homogeneous medium, since some coupling will be introduced between the electric and the magnetic field, thus using the scalar theory will entail some degree of error. However, this error will be small provided the boundary conditions only have effect over a small area of the aperture.

2.1.1 The Helmholtz Equation

The Helmholtz equation represents a time-independent form of the original scalar wave equation as derived from Maxwell's equations. By taking into consideration the complex field $U(P)$ as

$$U(P) = A(P)\, e^{-j\phi(P)} \tag{2.1}$$

where $A(P)$ is the amplitude and $\phi(P)$ the phase of the field disturbance at the position point P. Thus the Helmholtz equation for this disturbance is represented as

$$\left(\nabla^2 + k_0^2\right) U(P) = 0 \tag{2.2}$$

where ∇^2 is the Laplacian operator and k_0 is the *wave number*, the number of wave cycles that fits in a meter

$$k_0 = \frac{2\pi}{\lambda} \tag{2.3}$$

where λ is the *wavelength* in the dielectric medium ($\lambda = 1/\sqrt{\mu\epsilon}$).

2.1.2 Green's Theorem for Propagation

In order to compute a complex disturbance at a given point in space, a two dimensional special case of the Stoke's theorem, Green's theorem is used.

Green's theorem gives an analytical solution to uncoupled partial differential equations as Helmholtz ones. This is performed by a superposition of an impulse response with the Dirac's delta function at different points. Since further Green's theorem theory is out of the scope of this work, we start by using the following equation where the relationship between a closed surface integral and a volume integral is given

$$\iiint_V \left(U\nabla^2 G - G\nabla^2 U\right) dU = \oiint_S \left(U\frac{\partial G}{\partial n} - G\frac{\partial U}{\partial n}\right) dS \tag{2.4}$$

where $G(P)$ is the auxiliary function used to solve Green's theorem. A more physical intuition of what is an auxiliary function as $G(P)$ can be obtained from the Stokes theorem where the circulation over a closed line is obtained by addition of an auxiliary function, in this case, tiny curls over the surface which the line encloses. Both $U(P)$, $G(P)$ and their first and second partial derivatives must be single-valued and continuous within the closed surface S which surrounds the volume V. In our case, only a few auxiliary functions allow Green's Theorem to be directly applied to solve scalar diffraction problems with the required boundary conditions. For doing such procedure Kirchhoff's auxiliary function is usually chosen, also known as *free space* Green's function.

$$G(P_0) = e^{j\frac{k_0 r_{01}}{r_{01}}} \tag{2.5}$$

Where P_0 is the observation point surrounded by the closed surface S. The problem is then the computation of the complex disturbance at P_0 in terms of the values on S. r_{01} is the distance of the vector $\vec{r}_{01}$ pointing from P_0 to a point P_1 on the surface S.

The use of this particular auxiliary function lead to Kirchhoff's formulation of diffraction by a planar screen, although in good agreement with measurements, two conditions must be followed known as the *Kirchhoff boundary conditions*, which state that:

- Across the surface Σ, the field distribution U and its derivatives $\partial U/\partial n$ are the same as they would be in absence of the screen.

- Over the opaque portion of S_1, there is a geometrical shadow of the screen, the field distribution U and its derivatives are zero.

For the complete derivation of *Kirchhoff's formulation of diffraction by a planar screen* and the *Fresnel-Kirchhoff diffraction formula*, the user is redirected to the main reference of this chapter [86].

2.1.3 The Rayleigh-Sommerfeld Formulation of Diffraction

Although the Kirchhoff theory has been found to yield accurate results, there are some inconsistencies which arise from the fact that boundary conditions must be imposed on both the disturbance and its first derivative.

In order to remove the inconsistencies of the Kirchhoff theory, Sommerfeld proposed using a different auxiliary function G generated not only by a point source located at P_0 but simultaneously by a second point source located at position $\tilde{P}_0$ mirrored at the other side of the screen. If both sources are taken with a 180° phase difference, the Green's function in this case is

$$G_{-}(P_1) = \frac{e^{jk_0 r_{01}}}{r_{01}} - \frac{e^{jk_0 \tilde{r}_{01}}}{\tilde{r}_{01}} \tag{2.6}$$

where the subscript $-$ has been took in order to account for the 180° phase shift. Equation (2.6) vanishes in the aperture plane, therefore Kirchhoff boundary conditions can be applied to U alone, obtaining the so-called *first Rayleigh-Sommerfeld solution*:

$$U_I(P_0) = \frac{-1}{4\pi} \iint_{\Sigma} U \frac{\partial G_{-}}{\partial n} ds \tag{2.7}$$

The normal derivative of G_{-} is

$$\frac{\partial G_{-}(P_1)}{\partial n} = \cos(\hat{n}, \hat{r}_{01}) \left(jk_0 - \frac{1}{r_{01}} \right) \frac{e^{jk_0 r_{01}}}{r_{01}} - \cos\left(\hat{n}, \hat{\tilde{r}}_{01}\right) \left(jk_0 - \frac{1}{\tilde{r}_{01}} \right) \frac{e^{jk_0 \tilde{r}_{01}}}{\tilde{r}_{01}} \tag{2.8}$$

for P_1 on the surface S_1 the distances and the director cosines from the point sources P_0 and $\tilde{P}_0$ to P_1 are

$$\begin{aligned} r_{01} &= \tilde{r}_{01} \\ \cos(\hat{n}, \hat{r}_{01}) &= -\cos\left(\hat{n}, \hat{\tilde{r}}_{01}\right) \end{aligned} \tag{2.9}$$

and therefore on the surface the derivative of the auxiliary Green's function is

$$\frac{\partial G_-(P_1)}{\partial n} = 2\cos(\hat{n}, \hat{r}_{01})\left(jk_0 - \frac{1}{r_{01}}\right)\frac{e^{jk_0 r_{01}}}{r_{01}} \tag{2.10}$$

which can be further simplified taking into account that $r_{01} \gg \lambda$, leaving

$$\frac{\partial G_-(P_1)}{\partial n} = 2jk_0\cos(\hat{n}, \hat{r}_{01})\frac{e^{jk_0 r_{01}}}{r_{01}} \tag{2.11}$$

which can be seen as twice the normal derivative of the Green's function G used in Kirchhoff theory

$$\frac{\partial G_-(P_1)}{\partial n} = 2\frac{\partial G(P_1)}{\partial n} \tag{2.12}$$

Taking into account this result, the first Rayleigh-Sommerfeld solution can be rewritten in terms of the more simpler Green's function as

$$U_I(P_0) = \frac{-1}{2\pi}\iint_\Sigma U\frac{\partial G}{\partial n}ds \tag{2.13}$$

In order to obtain the *second Rayleigh-Sommerfeld solution* an analogue procedure can be followed starting by using the "in-phase" auxiliary function G_+

$$G_+(P_1) = \frac{e^{jk_0 r_{01}}}{r_{01}} + \frac{e^{jk_0 \tilde{r}_{01}}}{\tilde{r}_{01}} \tag{2.14}$$

In this case, the normal derivative is the one that vanishes on the screen aperture leading to the solution

$$U_{II}(P_0) = \frac{-1}{4\pi}\iint_\Sigma \frac{\partial U}{\partial n}G_+ ds \tag{2.15}$$

It can be shown that, supposing again that $r_{01} \gg \lambda$, G_+ in this case is twice the Green's Function used by Kirchhoff

$$G_+ = 2G \tag{2.16}$$

therefore the second Rayleigh-Sommerfeld solution yields

$$U_{II}(P_0) = \frac{1}{2\pi}\iint_{\Sigma} \frac{\partial U}{\partial n} G\, ds \tag{2.17}$$

2.1.4 The Rayleigh-Sommerfeld Diffraction Formula

In order to stablish a better comparison between the two Rayleigh-Sommerfeld solutions and the Kirchhoff theory, let the Green's function G_- and G_+ be replaced by the free space Green's function. Replacing (2.5) into (2.13) and assuming $r_{01} \gg \lambda$ yields

$$U_I(P_0) = \frac{1}{j\lambda}\iint_{S_1} U(P_1)\,\frac{e^{jk_0 r_{01}}}{r_{01}} \cos(\hat{n}, \hat{r}_{01})\, ds \tag{2.18}$$

The Kirchhoff boundary conditions may now be applied to U alone. Since no boundary conditions needs to be applied to $\partial U/\partial n$, the inconsistencies of the Kirchhoff theory have been removed, leading to the general result

$$U_I(P_0) = \frac{1}{j\lambda}\iint_{\Sigma} U(P_1)\,\frac{e^{jk_0 r_{01}}}{r_{01}} \cos(\hat{n}, \hat{r}_{01})\, ds \tag{2.19}$$

In 1678 Huygens proposed that the superposition of spherical waves will determine the disturbance of the wave at any subsequent position or time. Later in 1816, Fresnel corroborated the Huygens principle adding its own principle of interference. This equation states just that, a perturbation field U_I at point P_0 can be determined by the superposition of spherical waves with a given point source value $U(P_1)$. Thus, the Rayleight-Sommerfeld diffraction formula as derived from the first Rayleigh-Sommerfeld solution is in fact the *Huygens-Fresnel Principle*.

From here on after, equation (2.19) will be used as the main equation for propagation and diffraction when using the Scalar Diffraction theory.

By using the second Rayleigh-Sommerfeld solution the general result is

$$U_{II}(P_0) = \frac{1}{2\pi}\iint_{\Sigma} \frac{\partial U(P_1)}{\partial n}\,\frac{e^{jk_0 r_{01}}}{r_{01}}\, ds \tag{2.20}$$

It is worth mentioning that the Kirchhoff solution is the average of both Rayleigh-Sommerfeld solutions.

2.2 Diffraction in the Plane Wave Spectrum

Although the Scalar Diffraction theory is the usual way of presenting Fourier Optics, it is worth to have a second read using the Plane Wave Spectrum, also known as Angular Spectrum of Plane Waves or simply the k-Space. The Plane Wave Spectrum will be of the out-most importance in upcoming sections and chapters, mainly because the off-axis holographic process takes entire place on this domain, and thus special interest is placed on its presentation.

Following the introduction of the Plane Wave Spectrum, an alternate formulation for scalar diffraction theory is introduced by using this different framework that will introduce a linear and invariant approach by means of using the Fourier Transform and its convolution properties.

2.2.1 Plane Wave Spectrum

The Plane Wave Spectrum is a decomposition of any field disturbance in plane waves travelling in different directions, as described by the $\vec{k}$ vector, away from a given plane. In order to obtain this decomposition, the Fourier transform can be used. The Fourier transform of any field in a given plane allows its plane-wave representation to be retrieved for each $\vec{k}$ component $\vec{k} = \left(k_x, k_y, k_z\right)$ representing each travelling direction.

For a given field on $U\left(x, y, 0\right)$ travelling with a component of propagation in the positive z direction, its plane wave spectrum $\mathscr{U}\left(k_x, k_y; 0\right)$ can be obtained from its Fourier transform in a 2D plane as

$$\mathscr{U}\left(k_x, k_y; 0\right) = \iint_{-\infty}^{\infty} U\left(x, y, 0\right) e^{-j\left(k_x x + k_y y\right)} dx dy \tag{2.21}$$

And therefore the field can be reconstructed as the inverse Fourier transform of its spectrum

$$U(x,y;0) = \iint_{-\infty}^{\infty} \mathscr{U}(k_x,k_y,0)\, e^{j(k_x x + k_y y)}\, dk_x dk_y \tag{2.22}$$

One of the main advantages of using the Fourier transform is that the computation cost of all the required calculations will be greatly reduced by using the FFT, in spite of using the Spatial Diffraction theory presented in previous section.

2.2.2 Diffraction and Propagation in the *PWS*

In this section scalar diffraction and propagation theory are introduced as a linear filtering process carried out in the spectrum of plane waves. In [88] a more in-depth read can be found, as well as other references to a more rigorous set of references.

This approach starts with the Fourier transform of the Helmholtz equation (as seen on equation 2.2)

$$\left(k_x^2 + k_y^2 + k_z^2 - k_0^2\right) \cdot \mathscr{U}(k_x,k_y,k_z) = 0 \tag{2.23}$$

where (k_x,k_y,k_z) are the conjugate coordinates corresponding to the spatial coordinates (x,y,z), and $\mathscr{U}(k_x,k_y,k_z)$ is the Fourier transform of the scalar wave field $U(x,y,z)$. By taking into account that the integral can be reduced to a double integral on a sphere of radius k_0, thus the Fourier transform of the scalar wave field can be reduced to:

$$U(x,y,z) = \iint \mathscr{U}_0(k_x,k_y)\, e^{-jk_z' z} e^{-j(k_x x + k_y y)}\, dk_x dk_y \tag{2.24}$$

where $k_z' = \sqrt{k_0^2 - k_x^2, k_y^2}$ and $\mathscr{U}_0(k_x,k_y) = \mathscr{U}_0(k_x,k_y,k_z')$. Setting $z = 0$ yields

$$U(x,y,0) = \iint \mathscr{U}_0(k_x,k_y)\, e^{-j(k_x x + k_y y)}\, dk_x dk_y \tag{2.25}$$

So $\mathscr{U}_0(k_x, k_y)$ is the Fourier transform of the field $U(x, y, 0)$ on the plane $z = 0$. From this fact and from the convolution theorem, equation 2.24 can be expressed as the convolution

$$U(x, y, z) = U(x, y, 0) * g(x, y, z) \tag{2.26}$$

where $g(x, y, z)$ is the Fourier transform of $e^{-jk'_z z}$ given by

$$g(x, y, z) = \frac{1}{2\pi} \frac{\partial}{\partial z} \left(\frac{e^{jk_0 R}}{R} \right) \tag{2.27}$$

which can be shown to be the diffracted field of a point source, or the Green's function. By expanding equation (2.26) and substituting (2.27) the following equation is obtained

$$U(x, y, z) = \frac{1}{2\pi} \iint U(x, y, 0) \frac{\partial}{\partial z} \left(\frac{e^{jk_0 R}}{R} \right) dx dy \tag{2.28}$$

which can be identified as the first Rayleight-Sommerfeld solution as shown in equation (2.13) thus, showing that both approaches lead to the same result.

2.2.3 Propagation as a linear spatial filter

Once shown that scalar diffraction theory can be seen as a linear process, the linear filter for scalar wave propagation can be easily derived. However, one last thing must be taken into account, the expression $k^2 > k_x^2 + k_y^2$ must be satisfied, as it should for all true propagation directions. If this expression is satisfied then all waves will be travelling waves, otherwise we are going to be dealing with a complex value which will lead to evanescent waves. Thus, a circular filter with radius $k < k_0$ must be introduced in k-space. Equation (2.24) can be rewritten to

$$\begin{aligned} U(x, y, Z) \quad = \quad & \iint_{-\infty}^{\infty} \mathscr{U}(k_x, k_y, 0) \cdot \operatorname{circ}\left(\sqrt{k_x^2 + k_y^2} \right) \\ & \times e^{jz\sqrt{k_0^2 - k_x^2 - k_y^2}} e^{j2\pi(k_x x + k_y y)} dk_x dk_y \end{aligned} \tag{2.29}$$

2.2.4 Two-Dimensional Sampling of the *PWS*

Since all the simulated and measured data on this dissertation is based on sampled data, it is important to introduce the formulas which gives the relation between the spatial and the spatial frequency domain.

We start by computing the spatial frequencies of the plane wave spectrum. First of all, the discrete spatial sampling frequency k^s in either x or y coordinates can be obtained from

$$k^s_{x,y} = \frac{1}{\delta_{x,y}} = \frac{N_{x,y}}{W_{x,y}} \tag{2.30}$$

where $\delta_{x,y}$ is the spatial sampling interval, $N_{x,y}$ the number of points and $W_{x,y}$ the width in the x or y direction in the acquisition plane. Care must be taken on how the intervals are chosen. In this dissertation the sampling is supposed to extend ± half interval over the sampling grid, since our sampling point is centered around the sampling interval.

Knowing the sampling frequency, the plane wave spectrum is enclosed by

$$k_{x,y} \in \left[\frac{-k^s_{x,y}}{2}, \frac{k^s_{x,y}}{2} \right] \tag{2.31}$$

where care must be taken to include only propagating waves, thus evanescent waves will be removed throughout the thesis, since we will consider a proper distance between the diffracting aperture and the scanning plane at all times, thus giving sufficient space for all existing evanescent waves to decay properly. Finally the interval of our plane wave spectrum will be given by

$$k_{x,y} \in \left[\frac{-k_0}{2} < \frac{-k^s_{x,y}}{2}, \frac{k^s_{x,y}}{2} < \frac{k_0}{2} \right] \tag{2.32}$$

2.3 Quasioptical propagation of Gaussian Beams

The study of Gaussian beams by means of quasioptics, is commonly defined as the propagation of a collimated radiation through a beam which dimensions are small when measured in wavelengths, tranverse to the axis of prop-

agation. Geometrical optics includes rigorous and complete methods for analyzing optical and radiowave systems which share the common characteristic that the dimensions of all components (lenses, mirrors, apertures, etc...) are large enough so the effects of finite wavelengths can be neglected. For a more in depth read on Quasioptics, the reader is referred to [86].

In quasioptical propagation the radiation beams are treated to be largely collimated, which means that they have a well-defined direction of propagation with some transverse variation. Thus, equations for Gaussian beam propagation are derived from the paraxial wave equation. Starting as well from the Helmholtz wave equation (2.2), the paraxial approximation implies that we can drop the propagation term on the second derivative, since it will be small compared to the rest.

Solutions to this paraxial equation are the Gaussian beam modes, that form the basis to quasioptical systems. There is no cutoff for the application of the paraxial approximation, but is generally reasonably good as long as the angular divergence of the beam is largely confined within 30 degrees of the propagation axis.

The most common used equation of quasioptics throughout this dissertation is used to compute the field distribution radiated by a certain antenna. This field distribution in rectangular coordinates for two dimensions can be derived from the paraxial wave equation by using a solution based on a two dimensional Gaussian beam as follows, where the amplitude has been normalized to the maximum amplitude on the off-axis value.

$$E(x,y,z) = \left(\frac{2}{\pi w_x w_y}\right)^{0.5} \cdot e^{-\frac{x^2}{w_x^2}-\frac{y^2}{w_y^2}-jkz-\frac{j\pi x^2}{\lambda R_x}-\frac{j\pi y^2}{\lambda R_y}+\frac{j\phi_{0x}}{2}+\frac{j\phi_{0y}}{2}} \tag{2.33}$$

where $w_{x,y}$ correspond to the beam waist radius defined in the value of the radius at which the field falls to $1/e$ relative to the on-axis maximum value:

$$w_{(x,y)} = w_{(0x,0y)}\left[1+\left(\frac{\lambda z}{\pi w_{(0x,0y)}^2}\right)^2\right]^{0.5} \tag{2.34}$$

where $w_{0x,0y}$ denotes the beam waist radius at $z = 0$.

In eq. (2.33) $R_{x,y}$ is the radius of curvature of an equiphase surface for a given beam which depends on the position along the axis of propagation and can is defined as:

$$R_{(x,y)} = z + \frac{1}{z}\left(\frac{\pi w_{(0x,0y)}^2}{\lambda}\right)^2 \tag{2.35}$$

Finally $\phi_{0x,0y}$ is known as the Gaussian beam phase shift:

$$\phi_{(0x,0y)} = \tan^{-1}\left(\frac{\lambda z}{\pi w_{(0x,0y)}^2}\right) \tag{2.36}$$

One useful equation for converting between directivity and beam waist is shown in eq. (2.37), this equation is commonly used in the dissertation in order to obtain the waist for any given antenna based on the given directivity. Specially on commercial antennas where no design parameters are given other than their beam widths.

$$D \approx 2\left(\frac{2\pi}{\lambda}\right)^2 w_0^2 \tag{2.37}$$

2.4 Off-Axis Holography

Since wavefronts have a coherent nature, it is necessary to acquire information of both amplitude and phase. However, in the past, optical recording mediums responded only to light intensity, as well as direct microwave or terahertz detectors do. Off-Axis Holography, also known as indirect holography or Leith and Upatnieks holography, involves recovering a reflected or scattered wave by means of *interferometry*; adding a second wavefront with a known amplitude and phase to the unknown wave.

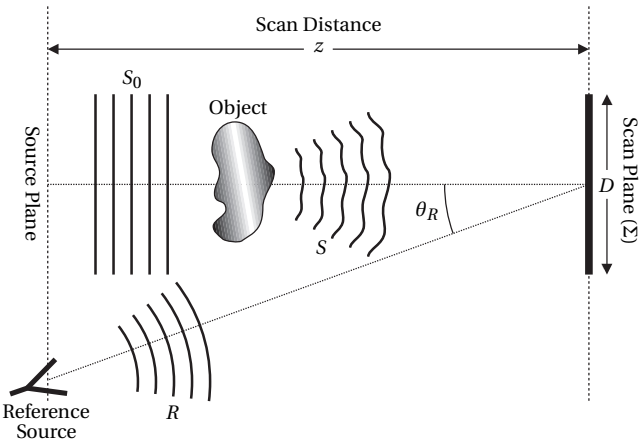

Figure 2.1: Basic diagram of a typical *off-axis* hologram scheme. The wavefront S_0 is composed of a plane wave incoming from the the source plane; the wavefront S is the scattered or diffracted wavefront resulting of applying the source wavefront S_0 to the object under test. The wavefront R is the reference wave, in this case a spherical wave as produced by a horn antenna.

The intensity of the interference pattern, or hologram H is proportional then to the intensity measurement I, which is composed of the target scattered field S and some previously-known reference R.

$$H \propto I = |S(x,y) + R(x,y)|^2 \tag{2.38}$$

by dropping the spatial dependence for x and y, equation (2.38) can be rewritten to

$$\begin{aligned} I &= SS^* + RR^* + SR^* + RS^* \\ &= |S|^2 + |R|^2 + SR^* + S^*R \end{aligned} \tag{2.39}$$

where * denotes the complex conjugate operator.

As shown in equation (2.39) the intensity of the acquired interference pattern is shown to depend on four terms. First two terms correspond to the spatial energy distribution of scattered and reference waves respectively, which are real numbers (quantities) that have no phase information and give rise to autocorrelation terms in the Fourier domain. The interest then will be focused on

the two S and R product terms, which lead to both the real and virtual image, and their superposition leads to the twin-image problem.

In order to separate the image terms from the intensity terms of the interference pattern in off-axis holography, the Plane-Wave Spectrum (PWS) of equation 2.39 must be obtained. Applying the two dimension (2D) Fourier transform, the spectral content of the interference pattern is shown to be

$$\mathscr{F}I = \mathscr{F}|S|^2 + \mathscr{F}|R|^2 + \mathscr{F}S \otimes \mathscr{F}R^* + \mathscr{F}S^* \otimes \mathscr{F}R \tag{2.40}$$

where $\mathscr{F}$ denotes the Fourier transform operation and $\otimes$ the convolution operator. Thus the aforementioned terms are found again to be the autocorrelation of both Source and Reference wave, and the cross-correlation between source and reference.

2.4.1 Off-Axis Hologram basics

From Gabor holography we known that complex information of the wavefront scattered by (or diffracted from) an object is present on the crosse-correlation terms of equation (2.40), thanks to the intensity of the superposition of the unknown wave with some reference wave. Using an offset reference, as stated by Leith and Upatnieks (as shown in figure 2.1), entails a spatial frequency separation of the image terms, provided that the specters of each terms are of a band-limited nature. Furthermore, this axial offset is required to reduce the spatial frequency overlap between the difference term which will produce artifacts in the final image.

If the reference wave is considered to be an ideal plane-wave traveling at a certain spatial angle, equation (2.40) shows that each cross-correlation term is composed of the convolution between the spectrum of the unknown wave $\mathscr{F}S$ (and its conjugate $\mathscr{F}S^*$) with the spectrum of the conjugate of the reference $\mathscr{F}R^*$ (and the reference $\mathscr{F}R$). The Fourier transform of the reference and its conjugate can be shown to be a delta on either side of the plane-wave spectrum and thus the convolution with the unknown wave shifts their spectrum to the

positive and negative part of the PWS; thus achieving not only the separation of the image terms from both autocorrelations but also from one another.

The reference wave is positioned at an angle (θ_R, ϕ_R) with respect to the origin of the acquisition plane Σ, and its spatial frequency spectrum $\mathscr{F}R$ can be shown to be centered at the spatial frequencies $k_{x,y}$ given by

$$\begin{aligned} k_{R,x} &= k_0 \sin\theta_R \cos\phi_R \\ k_{R,y} &= k_0 \sin\theta_R \sin\phi_R \end{aligned} \tag{2.41}$$

In Fig. 2.2 illustrates the spectrum of the interference pattern with an offset reference.

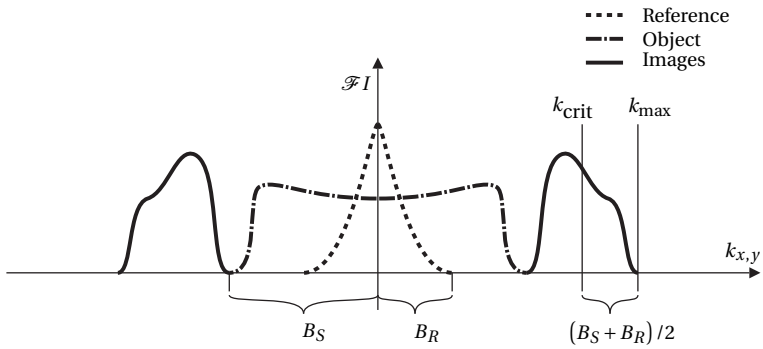

Figure 2.2: Spatial frequency spectrum of off-axis hologram power density. The first term from the Fourier transform of the intensity interference pattern as shown in equation (2.40) corresponds to the autocorrelation of the object(dot-dashed line), the second term corresponds to the reference autocorrelation (dashed line), while the third and fourth terms corresponding to the image and its conjugate (solid line). B_S and B_R are the full-bandwidths of the object and reference wave spectra respectively.

In order to achieve a successful separation of both convolution terms, thus avoiding overlap from autocorrelations, the image terms must be centered at a critical spatial frequency k_{crit}, derived from the spatial bandwidths of both the object and reference wavefronts

$$k_{crit} = \max(B_S, B_R) + \frac{B_S + B_R}{2} \tag{2.42}$$

where B_S and B_R are the spectral bandwidths of object scattered or diffracted and reference waves as shown on Fig. 2.2. The impinging reference wave must

be positioned with a critical angle θ_R (in a one-dimensional simplification as shown in Fig. 2.3).

$$\theta_R = \sin^{-1}\left(\frac{k_{crit}}{k_0}\right) \tag{2.43}$$

Even though the spectral bandwidth of the reference wave can be easily obtained since the reference will either be a simple known wave (plane, spherical or Gaussian wave) or by using a complex measurement; the bandwidth of an arbitrary propagated object wavefront field will pose a more difficult task since only some sort of approximation can be used which will depend on the type of object under test. For example for a reflector type antenna, the following approximation can be used as dervied in [89].

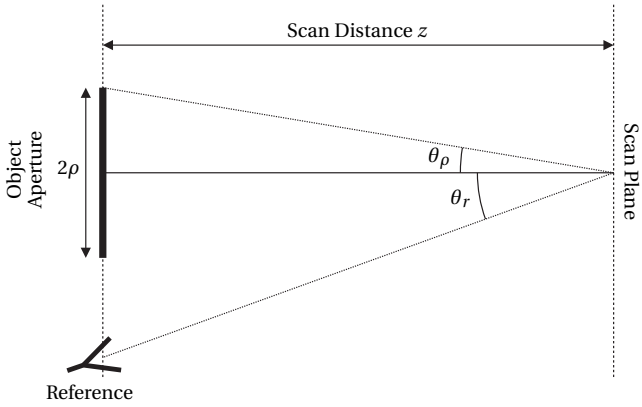

Figure 2.3: Schematic diagram of basic hologram geometry.

Assuming a spherical wave reference with spatial-frequency spectrum by

$$R(k) = A_R(k)\, e^{j\left(z_R\sqrt{k_0^2-|k|^2}+k_x x_R+k_y y_R\right)} \tag{2.44}$$

where $A_R(k)$ represents the plane wave spectral components of the reference antenna source.

And also assuming that our arbitrary object is a perfect reflector with theoretical spectrum

$$S(k) = \frac{\sin(\rho k)}{\rho k} \tag{2.45}$$

Using one of the image terms, for instance by using the third one of equation (2.40) the convolution yields

$$\begin{aligned} I_{\otimes}(k) &= S(k) \otimes R^{*}(-k) \\ &= \int_{-\infty}^{+\infty} S(k') R^{*}(k'-k)\, dk' \\ &= \int_{-\infty}^{+\infty} \frac{\sin(\rho k')}{\rho k'} e^{jz_o\sqrt{k_0^2-k'^2}} \cdot \left[A_R(k'-k)\, e^{jz_R\sqrt{k_0^2-(k'-k)^2}+j(k'-k)x_R} \right]^{*} dk' \end{aligned} \tag{2.46}$$

Expanding the square roots to their second order Taylor approximations the image term becomes

$$I_{\otimes}(k) \propto e^{j\left[k_0(z_A-z_R)+z_R\frac{k^2}{2k_0}-kx_R\right]} \int_{-\infty}^{\infty} \frac{\sin(\rho k')}{\rho k'} A_R(k'-k)\, e^{j\left[(z_R-z_A)\frac{k'^2}{2k_0}-\left(\frac{z_R k}{k_0}+x_R\right)k'\right]} dk' \tag{2.47}$$

by comparison with the following equation from [90]

$$\int_{-\infty}^{\infty} \frac{\sin(\pi x)}{\pi x} e^{-j2\pi Sx} dx = \begin{cases} 1 & |S| < 1/2 \\ 0 & |S| > 1/2 \end{cases} \tag{2.48}$$

Making $z_R = z_A = z$ and noting that $A_R(k)$ varies much slower than $\sin(\rho k')/\rho k'$, then a truncation point can be established for the integral in equation (2.47) when

$$\left| z\frac{k}{k_0} - x_R \right| > \rho \tag{2.49}$$

which leads to a maximum x-directed spatial frequency component of

$$k_x^{\max} = \frac{(\rho + x_R)\, k_0}{z} = k_0\left(\tan(\theta_\rho) + \tan(\theta_r)\right) \tag{2.50}$$

where θ_ρ is the angle subtended between the edge of the object under test and the scan origin and θ_r the angle subtended between the reference and the scan origin.

Thus the maximum spatial frequencies in our 2D problem regarding both the x and y-directed spatial frequency components are

$$\begin{aligned} k_x^{\max} &= k_0\left[\tan(\theta_\rho) + \tan(\theta_R)\sin(\phi_R)\right] \\ k_y^{\max} &= k_0\left[\tan(\theta_\rho) + \tan(\theta_R)\cos(\phi_R)\right] \end{aligned} \tag{2.51}$$

where it has been taken into account that our object is fitted inside a circle of 2ρ diameter and that we are using the reference angles as defined in (2.41).

2.4.2 Wavefront Reconstruction

Once the hologram, or the intensity of the interference pattern data is obtained, by taking into account all the requirements which yield a non-overlapped image in the plane wave spectrum, the desired image term is obtained by zeroing all the non-desired spatial frequency components, leading to the single image term:

$$\mathscr{F} I_{\otimes} = \mathscr{F} S \otimes \mathscr{F} R^{*} \tag{2.52}$$

from the properties of the Fourier transform a convolution in the transformed domain is equivalent to a product on the spatial domain

$$I_{\otimes} = SR^{*} \tag{2.53}$$

Assuming complete knowledge of the reference wave complex field R, or an approximation as in $\hat{R}$, the approximation to the complex field scattered by or diffracted from the object $\hat{S}$ can be recovered by removing the effect of the conjugate reference as in

$$\hat{S} = \frac{SR^{*}}{\hat{R}^{*}} \tag{2.54}$$

The assumption just taken in the above equation is valid in some fields as for example in microwave or terahertz holography where the referece wave can be fully acquired in both amplitude and phase hence $R = \hat{R}$ and therefore $S = \hat{S}$. However in some cases only the amplitude of the reference field can be measured, and thus the reference wave will have to be approximated either theoretically or by simulation. However, some studies have pointed out that by using simple reference waves such as plane-waves, spherical waves or Gaussian beam waves, the reference can be simulated yielding good results, as far as correct distances (it is common practice to perform some sort of optimization to obtain correct distances) are used for the reference wave simulation [91]. Thus

leading to $\hat{R}$ and therefore $\hat{S}$ to be fairly good estimations or approximations to both the complex reference R and the propagated field S.

Once $\hat{S}$ has been computed, a back-ward wave propagation filter by using equation (2.29) can be performed in order to obtain the image of the object or antenna under test.

CHAPTER 

OFF-AXIS GABOR HOLOGRAPHIC ARRAY

In this chapter the simulation, design, fabrication and measurement of a 16 element X-Band receptor array to be used with off-axis Gabor holography is discussed. The main purpose of the proposed system is to explore its advantages and limitations, as well as assess the technical issues, both in software and hardware, which may arise in the design and manufacture of an intensity-only imaging array, prior to a scale up in frequency towards W-Band or beyond. Using a one dimensional array of imaging elements brings the additional opportunity to experiment with different configurations, and thus different types of scenes have been taken into account in the upcoming sections. The tested scenes are the standard 2D Cartesian scene, a natural upgrade of the more common single-pixel raster scan, and a polar scene which can greatly speed-up the image acquisition rate while reducing the mechanical challenges of linear motorized stages.

The chapter is written mimicking the design flow of the array itself. It begins by designing and assessing the image capabilities of a one-dimensional ar-

ray, by means of presenting realistic simulations of the different imaging scenes under consideration. Once the design of the array has been planed out and properly validated in simulation, the sensor element of the array is designed, manufactured and characterized, enabling the fabrication of the whole 16 element array. Finally the array is validated in measurement and its results are reported followed by a brief discussion presented as final conclusions to the chapter.

3.1 Holographic array simulation

This section introduces the simulation of the different scenes studied along the chapter, and used to properly design the final array. In the dissertation, emphasis is taken on the validation of the array image recovering process itself.

The most straightforward way of implementing an imaging system is by using a single-pixel receiver mounted on a 2D scanner. This type of scene is similar to the raster scan of old television sets, where the whole image is constructed by sweeping a light-beam across the whole screen one line at a time, as shown in Fig. 3.1 (a). Even-though this type of system typically employs a relatively cheap RF stage, a 2D motorized stage is also required, which for most millimetre-wave applications could require a rather expensive piece of equipment. Furthermore, even with the most-expensive cutting-edge scanners, the acquisition time for a single image is extremely slow, as the scanning time will be usually limited by the travelling time of the scanner itself, however it is worth mentioning that sometimes the scanning time will be limited by the acquisition speed permitted by the detector bandwidth, since the travel distance must be kept less than 10% of the sampling interval while sampling on the fly, fast scanning will require then bigger detector bandwidths which will limit its dynamic range. The raster-scan imaging approach is normally used only for high-end purposes such as planar/polar scanners for near-field measurements inside anechoic chambers. In order to speed-up the system, a multi-pixel approach can be followed. Ideally a camera-like 2D full array receiver will be able to ac-

quire video-rate images, but the current state of technology is just starting to cope with such a high density of receivers [92], so current multi-pixel arrays are really expensive, even with only a few number of available receivers. A common trade-off between those two approaches consists in using a one dimensional receiver array scanned with a 1D only motorized stage. Where both the mechanical complexity and the acquisition time are decreased in exchange of a more costly RF stage. This 2D type of scan will be referred as the Cartesian scan (or scene) through out the rest of the chapter, as shown on Fig. 3.1 (b).

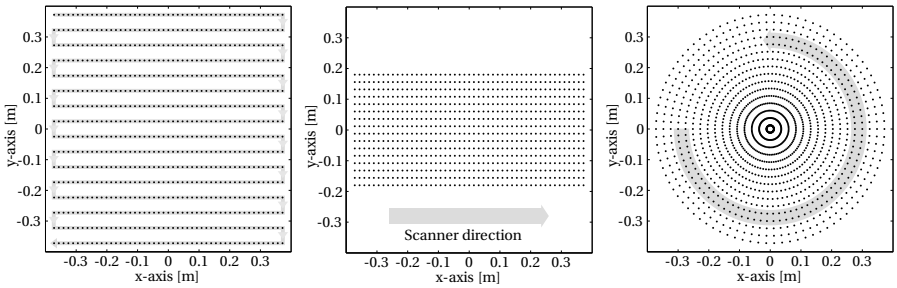

Figure 3.1: Different sampling schemes used in the current dissertation. (a) common raster scan, (b) one dimension scan for a one dimensional 16-element receiver array and (c) samples distributed along a circular scan path for the 16-element receiver array.

The second array sampling scheme involves a circular or polar movement of the array, so in this second case the array is rotated, requiring just a motor in a fan-like scanner as shown on the schematic drawing in Fig. 3.1 (c). This greatly reduces the price of the scanner since it just requires a simple motor with a proper encoder. Furthermore, the acquisition time of the receiver can be greatly reduced since in this case, the radial movement could be theoretically only limited by the receiver integration time, which makes this approach suitable in order to achieve images at video frame-rates with cheap non-stepper motors. The main drawback for this device is the requirement of a rotary joint in order to extract the low-frequency video signal from the receivers, even though other techniques can be explored such as sampling the

video signal in-place and transmitting it "over-the-air" by means of a suitable technology such as a radio link or even an optical transmitter.

3.1.1 The Cartesian scene simulation

For the Cartesian scene, the detector array is scanned in one dimension in order to obtain a two dimension matrix. However, the use of only 16 elements is not enough data for a useful image reconstruction, even using the low-number of samples in the offset reference axis (with fewer sampling requirements). The Cartesian scene is then composed of two scans of the same array, thus providing a total of 32 samples which provide a scan area comparable to that of the circular scheme (the area difference can be observed on Fig. 3.1). The Cartesian scene has been simulated entirely with the high-level numerical computation software Matlab with a join effort of the multiple theories introduced in chapter 2. Quasioptical theory is used for both source and reference waves which are computed by means of Gaussian beams (as introduced in section 2.3). While the source beam is computed on the image plane, the reference wave is computed on the scan plane, given a certain antenna position and direction.

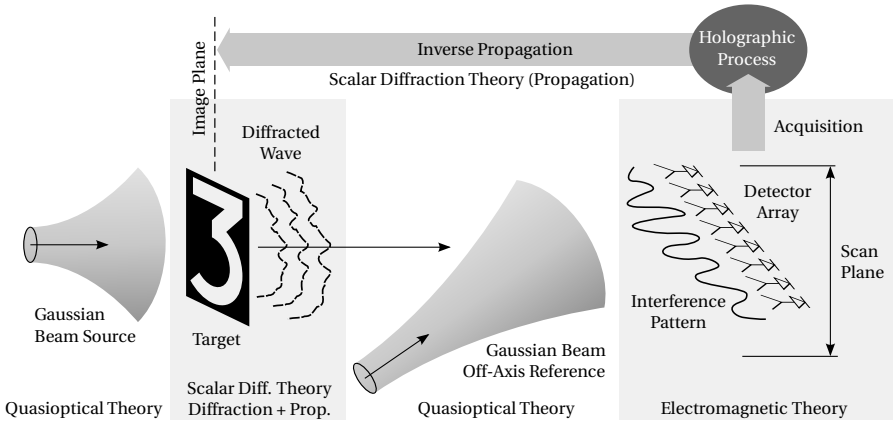

Figure 3.2: Simplified simulation diagram for the off-axis holographic detector array in the Cartesian scene.

The source wave is then diffracted by means of the Rayleigh Sommerfeld equation (2.1.3) by the target in Fig. 3.17 simulated as a perfect conductor planar screen. The diffracted wave is then propagated towards the scan plane by means of the spatial frequency filter from equation (2.29) as seen in section 2.2.3. Both the reference field and the propagated wave diffracted from the planar screen are combined to obtain the interference pattern, detected with a simple non-linear diode model and acquired with a 16 bit quantification. The digital signal is then fed to the holographic recovering process as explained in section 2.4.2. Finally the recovered field is propagated back to the image plane by means of the backward wave propagation filter in equation (2.29).

For the sake of clarity a scheme of all used methods and their corresponding theory is reported in the diagram of Fig. 3.2.

By using the aforementioned theoretical background, the simulation of the Cartesian scheme is carried out with parameters similar to those of the real scenario setup. In Fig. 3.3, a histogram of received power shows that more than 99% of the energy lays on the linear range of most common general purpose microwave detectors, between -10 to -50 dBm. Thus the dynamic range of the image superposes that of the microwave detector by using this particular configuration.

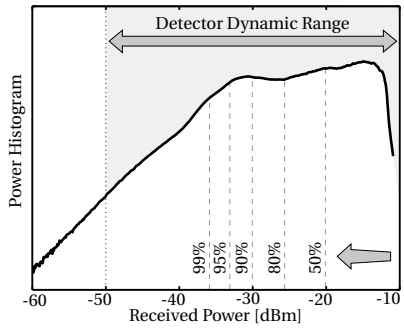

Figure 3.3: Received power histogram by the simulated imaging system. The figure is generated by computing the histogram of all the individual power contributions of each pixel of the 2D simulated scan plane.

The interference pattern obtained from the simulation is shown on Fig. 3.4 (a). The intensity of the signal is shown to be greater on the left-hand side of the figure, since the reference wave is geometrically closer to that edge thus resulting in a greater power intensity, which will be later taken into account when removing the effect of the reference wave.

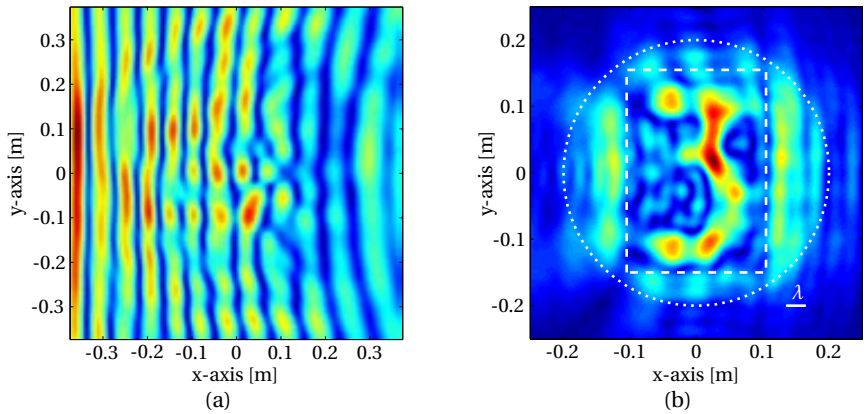

Figure 3.4: Off-axis Gabor holography simulation for the Cartesian scheme. (a) Interference pattern and (b) reconstructed image from the recovered amplitude field at the target position, the white dashed line represents the perfect electric conductor sheet target. The dotted line shows the non-blocked beam impinging at the target position.

In Fig. 3.4 (b) the recovered image shows poor resolution, since the target width is only about 1.3 λ and thus close to the resolving power of the array.

3.1.2 The circular scene simulation

The circular scheme is based on the diagram of Fig. 3.5, and simulated following the same pattern described for the Cartesian scheme (diagram on Fig. 3.2). The idea behind this concept is to rotate the array and thus achieve higher scan rates since the rotation can be performed at full-speed with the only requirement of properly driving the low-frequency signals through a rotary-joint, radio link or optical device communication system. Furthermore, by rotating the array the total span of the scan area is twice that of the one-dimensional array.

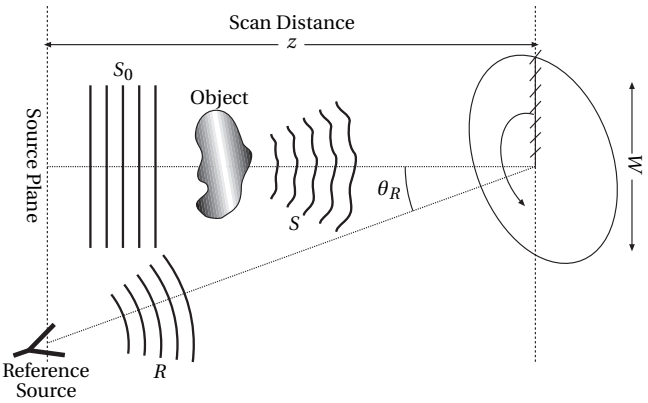

Figure 3.5: Simplified system diagram for the X-Band detector Arrays holography by means of the *Letih-Upatnieks* method with rotary array configuration.

Polarization

In this scene the array of receivers is rotated to acquire the interference pattern. In order to avoid polarization decoupling, either source and reference transmit antennas, or the antennas of the array elements have to be circularly polarized. Assuming that the transmit antennas are circularly polarized, and that the elements of the array are kept with a linear polarization in the radial direction, in an arbitrary angular position ϕ, the incident field can be shown to be

$$E_\rho = E\left(\frac{\hat{e}_x + j\hat{e}_y}{\sqrt{2}}\right)\cdot\left(\hat{e}_x\cos\phi + \hat{e}_y\sin\phi\right) \tag{3.1}$$

The resulting intensity is then proportional to the field in (3.1)

$$I:\rho = E_\rho\cdot E_\rho^* = \frac{|E|^2}{2}\cdot\left(\cos\phi^2 + \sin\phi^2\right) = \frac{|E|^2}{2} \tag{3.2}$$

Since only linear polarized transmit antennas were available, and the elements of the array had to be designed to be linearly polarized (for ease of fabrication, low-coupling and mechanical stability), two measurements had to be recorded for each acquisition, one for each polarization. This technique will only work provided that the response of the object under test is polarization independent, and thus, no difference is obtained by illuminating the object with

either vertical or horizontal polarizations. This is granted for objects following the scalar diffraction requirements. As a rule of thumb, objects with details greater than the wavelength will hold this requirement, objects which do not hold the scalar diffraction properties, such as for example a metal grating polarizer, will not lead to a recoverable image.

In Fig. 3.6, an actual measurement of the interference pattern between source and reference transmit antennas is shown for both the horizontal (a) and vertical (b) polarization, where the actual effect of the polarization decoupling is shown to be an angular modulation of the total interference pattern as shown in (c), reconstructed by direct combination of the vertical and horizontal components. As with the simulation in Fig. 3.4, here the power distribution is shown to be stronger on the right-hand side of the acquisition plane, due to the position of the reference antenna.

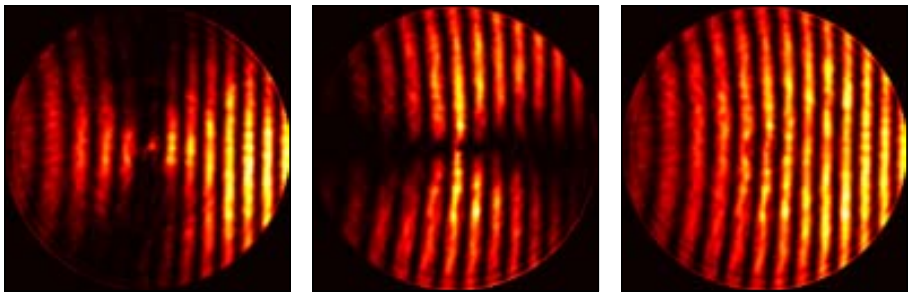

(a) (b) (c)

Figure 3.6: Acquired power of the interference patterns between source and reference antennas (50 cm separation) for (a) horizontal and (b) vertical polarizations and the resulting combination of both (c).

Polar to Cartesian transformation

Once the data has been obtained, it is composed of a 2D matrix whose indexes represents both the number of the antenna and the rotation angle. In order to process this information different alternatives can be followed such as a polar to Cartesian interpolation or more advanced techniques such as the Polar Fourier transform [93, 94].

Since the array can be sampled at a high speed while it rotates, a huge number of samples are available in concentric rings as shown in Fig. 3.1 (c) which means that the sampling will be critical along the radial axis where it will since it will have the lower number of samples in the measurement. By using a polar to Cartesian interpolation a 2D array representing the XY space can be recovered and used directly with the same holographic recovering process as used throughout the dissertation.

Circular scene simulation

In this particular case, after a first theoretical simulation, a more refined simulation of the diffracted wave, has been performed or improved by taking into account both the actual antenna pattern of each element as a small Yagi antenna, as well as the coupling between the elements of the array. This has been achieved by means of using the full-electromagnetic commercial simulator FEKO. The simulation is carried out by means of mimicking the rota-

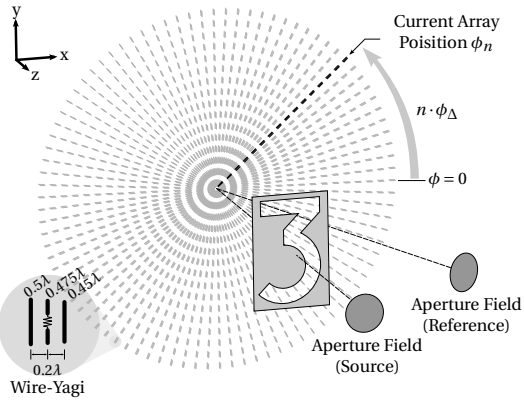

(a)

Figure 3.7: (a) Circular sample distribution for a 16 element array and 90 samples per rotation (or $\phi_\Delta = 4°$ per sample). (b) Scheme for full electromagnetic simulation with FEKO, the array is simulated by 16 wire-Yagi antennas sweep at ϕ_Δ intervals. The detected signal is extracted from the voltage across the resistor on each element of the array.

tion of the array by sweeping the array movement one angle at a time (ϕ_Δ = 360°/number of samples per revolution). The whole 16 element array is composed of simple wire-Yagi antennas with single reflector and director parasitic elements as shown in Fig. 3.7. In the simulation each antenna is loaded with a matched resistor, where the incoming signal level can be sensed by means of its resulting voltage across a 50Ω load. Both transmit source and reference wave can be chosen among different types of waves, plane-waves, point sources, simulation of actual antennas or the direct application of Gaussian beams. Gaussian beams have been used as the source of choice for the presented study cases. The computation time of using such method is much lower than having to compute the 3D representation of an actual antenna. However, the computation of the Gaussian beam was first compared to the full-wave simulation of the transmit antennas in order to verify that the correct Gaussian beam model was being used for our particular antenna. In Fig. 3.7, the actual simulation scheme for the FEKO simulation is shown, as well as the structure and dimensions of the wire-Yagi antenna used as array element.

The spacing between the elements of the array has been chosen to be 0.8λ, as an optimum simulation trade-off between minimum sampling (hence maximum spatial frequency) and total width of the scanner, leading to better spatial frequency resolution for the given target under test, taking also into consideration the minimum space required for the actual sensing element physical dimensions.

In Fig. 3.8 (a), the interference pattern resulting from the FEKO simulation is shown first for a 16 element array, where small artifacts are present in the form of small circles, which introduce a low spatial variation similar to that of a spatial interference produced by reflection but with a circular nature. This artifact is produced by the circular to Cartesian interpolation, and is ultimately caused by the low number of points along the array axis. The same behaviour is also present, on the actual interference pattern measurements from both Fig. 3.6 and Fig. 3.22.

In order to diminish those artefacts, the array can be shifted by half sep-

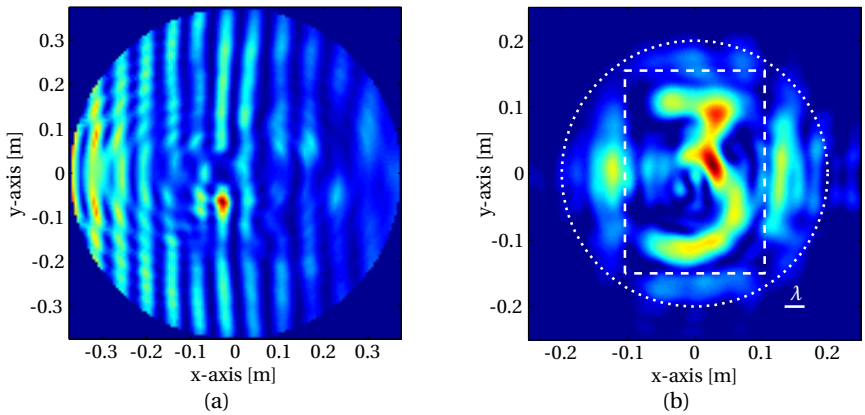

Figure 3.8: Off-axis Gabor holography simulation for the circular scheme with a 16 element array. (a) Interference pattern and (b) reconstructed image from the recovered amplitude field at the target position. The white dashed line represents the copper metal sheet target. The dotted line represents the non-blocked beam impinging at the target position.

aration step in order to obtain a virtual 32 element array at 0.4λ separation. By using this second approach the same simulation leads to the interference pattern of Fig. 3.9 (a), where the artifacts are still present but with a lower lever.

Once the circular to Cartesian interpolation has been performed, the application of the same recovering process, as used before for the Cartesian approach, leads to the image in Fig. 3.8 (b) and Fig. 3.9 (b), where the target number "3" is clearly recovered, as well as the edge and the impinging beam outside of the metal sheet. The image of the target is slightly better than that of the Cartesian simulation, which in part is caused by the intrinsic spatial circular filter imposed by the rotation of the array. By imposing a similar filter to the Cartesian simulation similar results are obtained. Even-though there is not much difference between the 16 and the 32 element, there is some improvement on the definition of both the number "3" and the rim of the metal sheet.

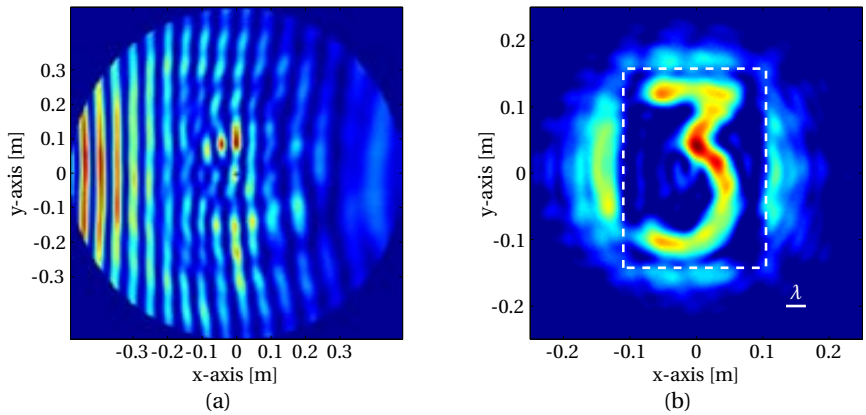

Figure 3.9: Off-axis Gabor holography simulation for the circular scheme with a 32 element array. (a) Interference pattern and (b) reconstructed image from the recovered amplitude field at the target position. The white dashed line represents the copper metal sheet target. The dotted line represents the non-blocked beam impinging at the target position.

3.2 Holographic Array Design

In this section the design, manufacture and characterization of the off-axis holographic array is reported. The basic element, an X-Band detector, is first designed according to the theory introduced in the schottky detector section 1.4.2, followed by its characterization and the whole array implementation.

3.2.1 X-Band Detector Design

The design of a microwave detector is extremely dependent on the Schottky diode model. For the required detector, a SMS7360-079LF low barrier Schottky diode from *Skyworks Inc.* was chosen for both its low-price, availability and, most important, great performance at the operating frequency range, where the diode impedance has a very low reactance. A microwave detector is typically based on a single or dual Schottky detector following the scheme of the diagram in Fig. 3.10. Before the diode device, the microwave detector is composed of the RF input (such as an antenna), a matching network which matches the impedance of the input stage to the impedance of the diode, and a DC re-

turn path which provides a proper path to ground for the DC signal, while at the same time must act as an open circuit for the RF signal. The diode is followed by a short circuit for the RF signal and, if required, a DC bias which will provide the appropriate operation point for the diode (this will not be the case in our design since we are using a zero-bias Schottky diode). Following the RF stage, the DC signal is filtered and amplified in the so-called *video stage* which provide appropriate conditioning for the ADC in the final acquisition stage of our element.

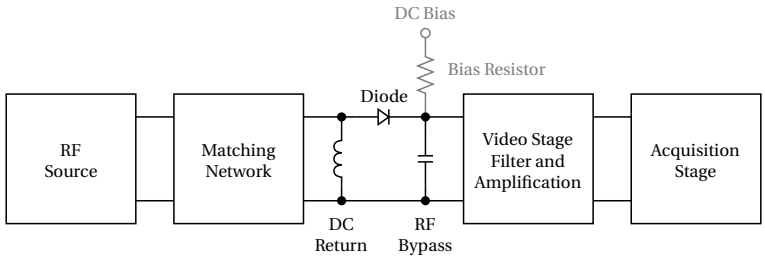

Figure 3.10: Diagram of a typical Schottky diode based microwave detector [69].

Since the development of the X-Band detector is used for testing purposes, the demonstrator is build with a central frequency of 9.4 GHz, a ten fold downscale from 94 GHz, where most commercially devices are available in the W-Band. The design of the detector involves a trade-off between sensitivity and bandwidth. The main goal for this detector has been achieving a high sensitivity in expense of a medium bandwidth [95].

The RF source for the microwave detector will either be an antenna printed on the same substrate or an antenna connected through an SMA (SubMiniature version A) cable specified both to a characteristic impedance of 50 Ω, which will also ease the characterization of the device through the Vector Network Analyzer (VNA). The chosen Schottky diode is a low-barrier SMS7630-079LF from *Skyworks Inc.* This low-barrier diode is also known as a zero-bias diode since it is manufactured with a low bias operation point; this low operation point makes it possible to work by using the power of the incoming RF signal alone, thus simplifying the design and cost of the final device since no bias has to be applied (and isolated from the RF signal), further considerations on

zero-bias Schottky detectors are reported in [96]. The parameters of the SPICE model, as extracted from the datasheet and fitted to our device, are shown on Table 3.1.

Parameter	SMS7630	Units	Parameter	SMS7630	Units
I_s	$5 \cdot 10^{-6}$	A	XTI	2	-
R_s	16	Ω	F_C	0.5	-
N	1.05	-	B_V	2	V
TT	$1 \cdot 10^{-11}$	s	I_{BV}	$1 \cdot 10^{-4}$	A
C_{j_0}	0.14	pF	V_J	0.34	V
M	0.4	-	L_S (pkg)	0.75	nH
E_G	0.69	eV	C_P (pkg)	0.2	pF

Table 3.1: PSPICE model for comercial Schottky diode SMS7630-079LF from *Skyworks Inc.*, including parasitic effects from the package.

Diode impedance matching

This Schottky diode is optimized for use in the X-Band range and thus has a very low reactance around 10 GHz. Different matching schemes can be performed depending on the desired bandwidth of the detector [97]. In order to match the low impedance of the diode, shown in Fig. 3.11 (a), to the impedance of the RF input, so the full power of the incoming wave goes through the diode, the impedance matching section is composed of a short-length line, used for fine-tuning the central frequency of the matching (b), followed by a simple quarter-wave impedance transformer (note that both simulation and measurement in Fig. 3.11 (c) take into account the contribution of the whole detector, not only the impedance of the transformer. In Fig. 3.13 the log-magnitude of the S_{11} is also represented).

The resulting reflection coefficient for this matching results on a bandwidth greater than 250 MHz with a Fractional Bandwidth (FBW) of 10%.

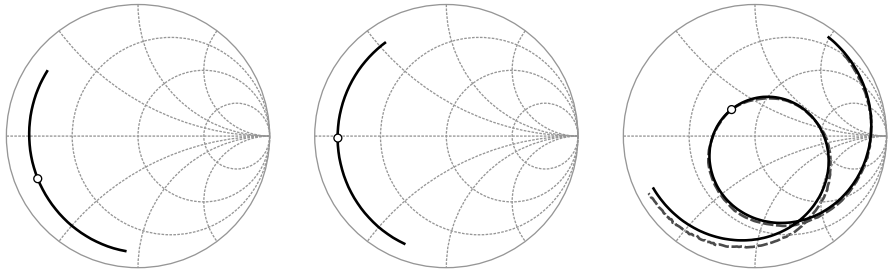

Figure 3.11: Impedance matching process of the Schottky diode for the X-Band microwave detector. Reflection coefficient for (a) the Schottky diode, (b) short line added to the diode and (c) whole microwave detector with quarter wave impedance transformer. Simulations are shown in solid-black line, whereas the measurement of the whole microwave detector is shown in dashed-gray line. The central design point at 9.4 GHz is shown in each step of the matching process.

DC return path

Once the matching has been designed, the DC return path for the diode is added by means of a straightforward quarter-wave shorted line, ideally acting as a high-frequency choke [98]. This line allows the DC current flow to the diode, but is seen as a virtual open circuit by the RF signal. By using this straightforward approach the resulting bandwidth is comparable to that of the transformer, without resorting to more complicated (and bigger) structures such as for example a radial stub with a high-impedance DC grounded line [99, 100].

Shorting filter

The anode of the diode is then connected to a shorting filter which must provide a proper short for the RF signal while letting the detected DC signal to pass through to the video stage.

The shorting filter is implemented by means of an step-impedance filter, other types of filters are often used such as hammerheads [101] or radial stubs. The magnitude of the reflection (S_{11}) and transmission (S_{21}) coefficients of the designed filter are shown in Fig. 3.12 (a), where the step-impedance filter is shown to behave as a low-pass filter, and thus complies with the required func-

tion of letting the DC voltage pass while rejecting the RF signal with a short-circuit as shown in (b) where the reflection coefficient is plot on the Smith chart, and the mark indicates that at the designed frequency the filter behaves as an RF short.

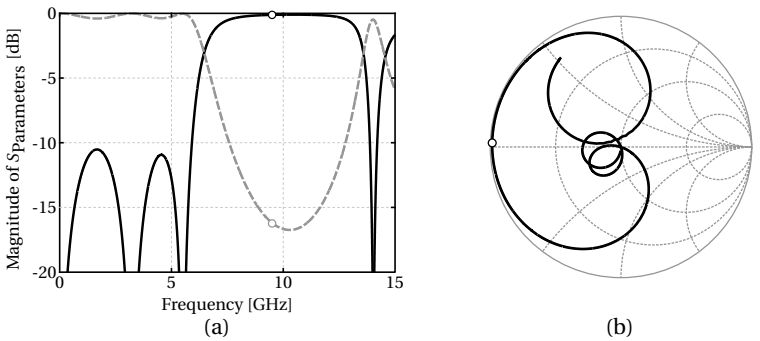

Figure 3.12: Shorting filter by means of a step-impedance filter. In (a) the scattering parameters are shown for both the reflection (S_{11}) in grey-dashed line and the transmission (S_{21}) coefficient in dark-solid line. The mark shows the center frequency at 9.4 GHz. In (b) the reflection coefficient of the filter is plot in the Smith chart, showing that at the desired frequency the shorting filter behaves as a short-circuit.

Detected voltage

Design on previous section have been carried out by means of Large-Signal S-Parameters (LSSP) for computing the Scattering parameters including non-linear devices such as the employed diode. For this section the used simulation tool is Harmonic Balance (HB), a frequency-domain analysis technique for simulating distortion in nonlinear circuits and which can be used along with analog RF and microwave systems [102]. In the context of high-frequency circuit simulations, harmonic balance obtains frequency-domain voltages and currents by means of computing its steady-state spectral content in the circuit. Harmonic balance is used to calculate the output voltage of the device for any given input power and frequency in order to characterize the output diode voltage and the required video impedance.

The trade-off between noise and maximum detected voltage is solved by means of using a 10 kΩ resistor as video load impedance for the diode since

the voltage is near-maximum while the noise is kept at a minimum level. In the aforementioned design, detected voltage versus temperature has not been taken into account assuming a constant room temperature at the lab facility, for a more thorough study on detector temperature dependence, the reader is referred to [103].

The detector is simulated versus both input power level and frequency. Both matching as well as the video output filter are tuned in order to obtain the maximum possible detected output at the central design frequency of 9.4 GHz. The resulting detector provides about 8 mV at -30 dBm input RF power as shown in Fig. 3.13, for both (a) detected voltage versus input power level and (b) detected voltage versus frequency.

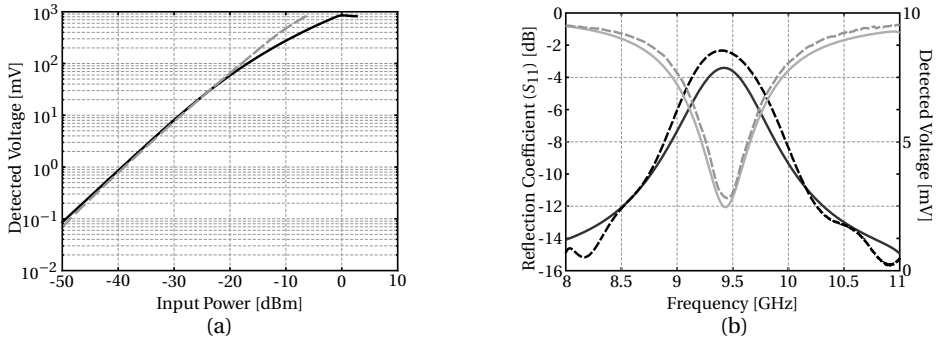

Figure 3.13: Comparison between the simulated X-Band microwave detector and the actual measurement for (a) detected voltage versus input power level, in black-solid line the harmonic-balance simulation and in gray dashed-line the actual measurement. This results have been obtained at the central design frequency of 9.4 GHz at an input level of -30 dBm. In figure (b) both the output detected voltage (black lines) and the reflection coefficient, S_{11}, (grey lines) are shown versus frequency; solid-lines represents simulated data while dashed-lines are the actual measurements of the manufactured device.

3.2.2 Quasi-Yagi Antenna

The microwave detector requires an antenna element which receives the incoming radiated electromagnetic signal from free space and translate it to a region where the wave is guided towards the microwave detector.

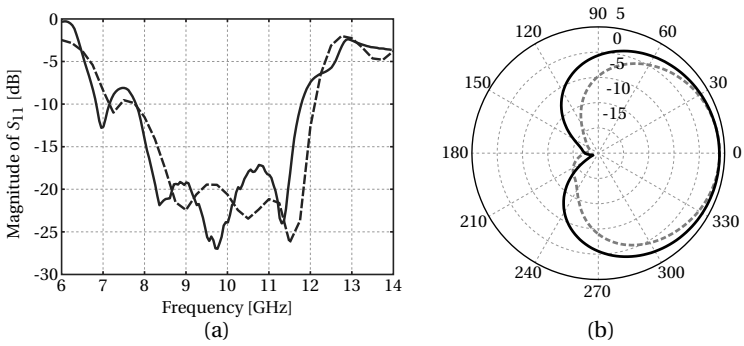

Figure 3.14: (a) Magnitude of S_{11} for the quasi-Yagi anntena. Simulated with Feko in dashed line and actual measurement in solid line. (b) Quasi-Yagi simulated directivity in dB for E-plane in gray dashed line and H-plane in solid black line.

The antenna used as sensing element is known as a quasi-yagi antenna [104]. This antenna is based on the classic Yagi-Uda configuration [105, 106] but is specifically adequate for our application since it is realized on a high dielectric constant substrate (RO3010), which enables sampling intervals as low as $\lambda/2$; this antenna is also compatible with microstrip circuitry; presents low coupling between elements since they are placed on the respective minimum of radiation, and furthermore, has small directivity, which means that high spatial frequencies will be detected. Although the use of an active system does not require high bandwidth, it makes multiple frequency measurements possible since it has a bandwidth of about 5 GHz or a FBW of nearly 50% as shown in Fig. 3.14 (a). The directivity diagrams are shown in Fig. 3.14 (b), with a maximum directivity at its boresight of 3 dB. The actual layout of the antenna is shown at the proper scale on Fig. 3.15 (a).

3.2.3 Detector fabrication

The microwave detector, both first prototype as well as all elements of the array, have been milled with a circuit board plotter ProtoMat S62 machine from *LPKF Laser & Electronics*. In order to mill those high-frequency substrate care must be taken in order not to remove (mill) the topmost layer of the dielectric, since it

will greatly affect the response of its distributed components, even-though deviations due to over-mill are more perilous to other distributed elements such as resonators and thus more difficult in coupled resonator filter design.

The chosen dielectric is a high-dielectric constant laminate composed of a ceramic-filled PTFE composite for use in high-frequency microwave and RF applications with designation RO3010 from *Rogers corp.*. The substrate used has a height of 0.635 mm with dielectric constant of 10.2 and a loss tangent of 0.0023.

The final layout of both detector and antenna are shown on Fig. 3.15.

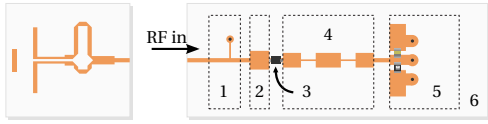

(a) (b)

Figure 3.15: Split layout in actual dimensions of (a) quasi-Yagi antenna and (b) x-Band detector schematic layout composed of: 1.- DC Return path, 2.- impedance matching, 3.- SMS7630-079LF diode, 4.- RF shorting filter, 5.- video filter and connections, 6.- Rogers 3010 substrate ($\varepsilon_r = 10.2$).

3.2.4 Detector array design

The detector designed in 3.2.1 is cloned to manufacture a sixteen element one-dimensional array. The number of elements in the array has been fixed by the maximum amount of single-ended analog inputs available in our NI-PCI 6251 data acquisition board from *National Instruments*. The spacing between elements is fixed as a trade-off between spatial and frequency resolution, resolved to be 0.8λ. The X-Band detector array will be used for taking unfocused images by means of microwave holography for both a rectangular and circular, or rotary, configuration as shown in the diagram of Fig. 3.5.

3.2.5 Elements of the array

The detectors of the array are separately mounted on an FR-4 substrate which acts both as support for the delicate receiver RO3010 substrate and as the detected signal router, which drives the incoming signals towards the acquisition card ribbon cable. The element spacing of the array is chosen to be 0.8λ, since a good trade-off is achieved between overall length (75 cm) and spatial sampling frequency. The overall length established the spatial frequency resolution of the system while the spatial sampling sets the maximum spatial frequency spectrum which can be resolved without aliasing artifacts for the given object under test. The whole array is assembled as shown in Fig. 3.16, compared to a 1€ coin.

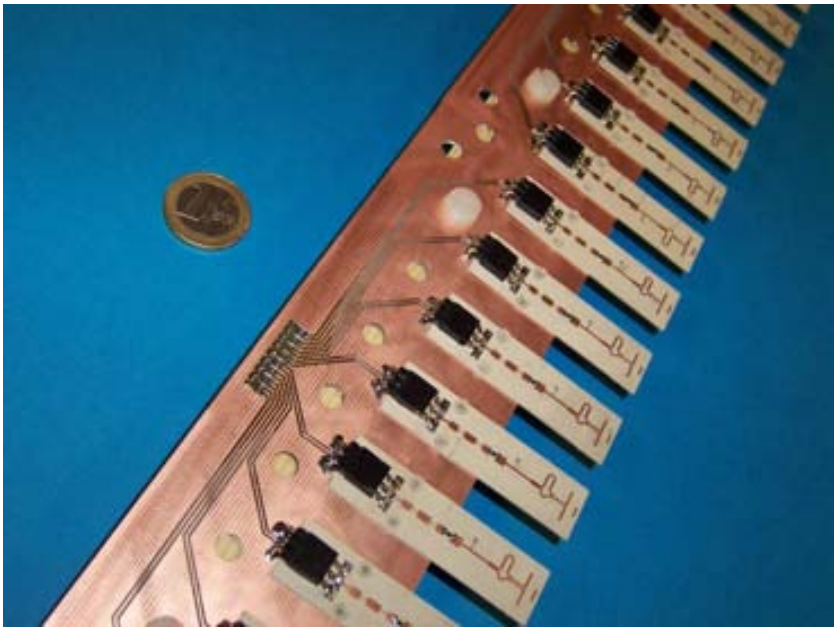

Figure 3.16: Photograph of the 16 element rotary X-Band array.

3.2.6 Target under test

Even-though different objects have been used for testing the array, the same planar screen is presented as shown previously in the simulation section. A number three has been cutout from a 30×20 cm copper metal sheet with a 1.3λ path as shown on Fig 3.17.

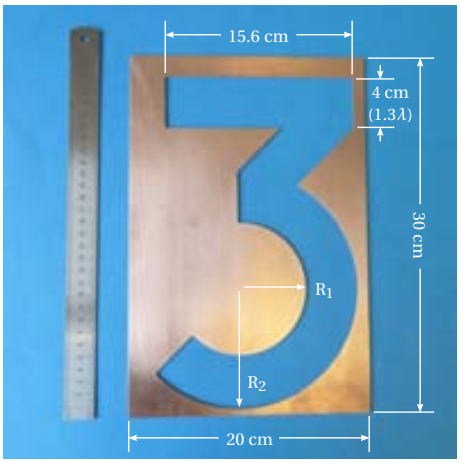

Figure 3.17: Photograph of the x-Band holographic target used in both simulation and measurements (R_1 = 5.6 cm, R_2 = 9.6 cm).

3.2.7 Validation and calibration of the array

In order to validate all the elements of the array, a N5183A MXG Analog Microwave Signal Generator from *Agilent Technologies* is used to drive an antenna in front of each receiver. In order to perform a calibration of the power to be received by every single receiver, a single quasi-yagi antenna is manufactured and connected to a U2002H USB Power Sensor from *Agilent Technologies*. By using the commercial software Matlab, a power sweep is programmed to the signal generator and the data of the power sensor is captured and stored for later comparison with the actual detected voltage of the receiving elements.

By using the antenna connected to the power sensor as a reference point, every single array element is placed at the same standing point. The program automatically sweeps the output power of the signal generator, and the charac-

teristic detected voltage is extracted for every diode-based receiver. In fig. 3.18 the different curves for every single receiver are shown, where it is clear that the deviation on the device response is small in the linear and saturated regions. There is an outlayer with far more noise than the average, caused by a faulty solder which was later fixed and thus its response corrected.

In Fig. 3.18, the linear section of the devices is shown to extend from -45 to -20 dBm. These curves can later be used for calibrating the response of each receiver, by mapping each output voltage to its corresponding power if the power received by the array is greater than -20 dBm at some point during the acquisition of the interference pattern.

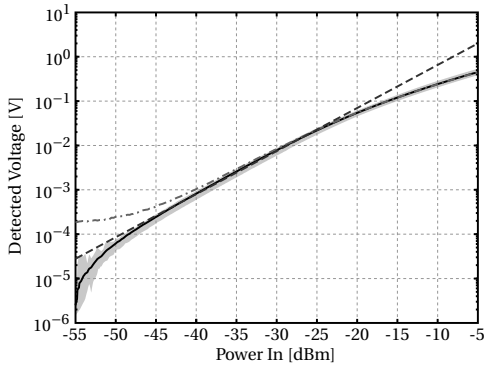

Figure 3.18: Voltage detected for each element of the array versus power sweep shown lying inside the grayed area, except for the out-layer (represented in gray dot-dashed line), which was later fixed. In solid black line the average of the output detector voltage is shown with an average sensitivity of 3800 mV/mW. Finally a linear response guide dashed-line is shown in dark-gray.

3.3 Holographic Array Measurements

Once the design and characterization of the array and its elements has been presented, in this section the holographic experiment is setup, and its measurements presented and discussed along with the recovered image for both Cartesian and circular scenes.

3.3.1 Experimental setup

Similar configurations are used in both scenes. However, minor changes had to be applied in order to cope with physical limitations such as the maximum extent of the linear motorized stage, which will be taken into consideration in the upcoming sections. On the transmit section of this setup, the same exact configuration is used in both scenes, source and reference transmit antennas are based on two in-house manufactured open-ended circular waveguide antennas with standard directivity of 7 dB. Those antennas are mounted on a sliding rail where its separation can be easily adjusted between almost "contact" (1cm) and 120cm. Furthermore, the fundamental issue in order to achieve a correct measurement in the circular scene, where both vertical and horizontal polarizations are required, is taken care by a custom in-house manufactured antenna holder which enables a precise 90° antenna rotation along its axis. In Fig. 3.19 (a) a descriptive drawing of this piece shows how we can achieve the 90° rotation in the antenna (and hence its polarization) by choosing the appropriate set of holes while mounting the antenna holder in the rail. In Fig. 3.19

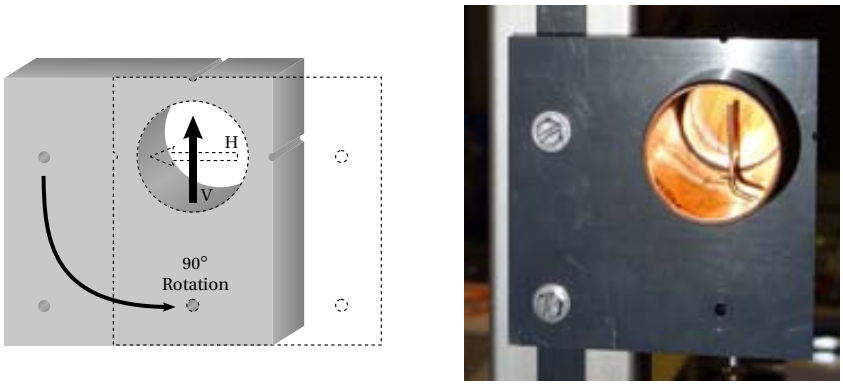

(a) (b)

Figure 3.19: (a) Drawing of the PVC manufactured antenna holder showing how the required 90° rotation is achieved, thus obtaining horizontal and vertical polarizations. (b) Actual picture of open-ended waveguide antenna on the antenna holder mounted on the vertical rail system.

(b) a picture of the PVC antenna holder mounted on a vertical rail.

The final configuration of the transmit antennas, as obtained from simulation, involves a separation of 80 cm between them and a 50 cm separation towards the target, mounted in front of the source antenna, which provides enough illumination from the source, avoiding at the same time blockage from the reference wave.

In the case of the Cartesian scene, the 2-axis linear motorized stages are centred at one meter in front of the source antenna, while in the polar scene the rotation motorized stage is the one centered in front of the source transmit antenna.

With the actual technology available in our lab, the acquisition time with the Cartesian scenario is about 40 minutes, for the circular scheme the timing can be as low as 4 minutes. However, ghosting problems present between the different channels of the acquisition card makes the rotation to take up to 20 minutes.

3.3.2 Motorized stages

In order to perform the required movements, either in the Cartesian or the circular scenes, both some linear and rotatory motorized stages are required. In the Cartesian case the array is mounted on two 60 cm Linear motorized stages (NLS8) from Newmark Systems. Although a single stage should suffice for this configuration, the requirement of double the measurement points, from 16 to 32, makes it worthy to use the second available stage to automatically displace those 12 mm. Those linear stages are mounted in a XZ configuration, with maximum speed of 25 mm/s with a maximum motor resolution of 0.08 μm with a bidirectional repeatability of 10 μm, a picture of this linear motorized stages is shown in Fig. 3.20 (a). For the circular scene the array is mounted on a RT-5 Rotary Stage (Fig. 3.20 (b)) also from Newmark Sytems with a maximum motor resolution of 0.36 arc-seconds and a repeatability of 5 arc-seconds and a maximum speed of 25°/s.

(a) (b)

Figure 3.20: (a) Two NLS8 Linear motorized stages in an XY configuration (50 mm travel range instead of 600 mm). (b) RT-5 Rotary motorized stage. Both images are from the manufacturer, Newmark Systems Inc. `http://www.newmarksystems.com/`.

3.3.3 Cartesian scene measurement

As in the Cartesian simulation, the array must cover roughly the same area as the circular scene, so the array is scanned twice in +x and -x thus obtaining a total span equal to 75 cm, equal to the outer diameter in the circular scene setup. However, the actual maximum scanning range of the linear motorized stage is 58 cm, and this will cause a trimming on the resolved image. In the Cartesian scene, we can decide the best direction for the reference wave since we will only have 64 sample points on one axis, the longer one, but in the short axis we will have as many data points as we want. This is specially opportunistic for holography, as the sample points required in the reference axis is always greater since the bandwidth to resolve is also bigger (the bandwidth is shifted towards greater frequencies).

In this case then, the reference will be aligned perpendicular to the array to take advantage of the multiple available points.

In Fig. 3.21 (a) the actual measurement of the Cartesian scene is shown, where the margins are kept identical to those of the simulations in order to show the difference in the scan plane. In (b), the recovered image is shown where the number “3” is shown to be in really good agreement with the actual simulation in Fig. 3.4 (b) on page 60, where all the maxima and minima of the number “3” are represented in the exact same position. The aforementioned trimming of the recovered image is clearly shown in both left and right hand

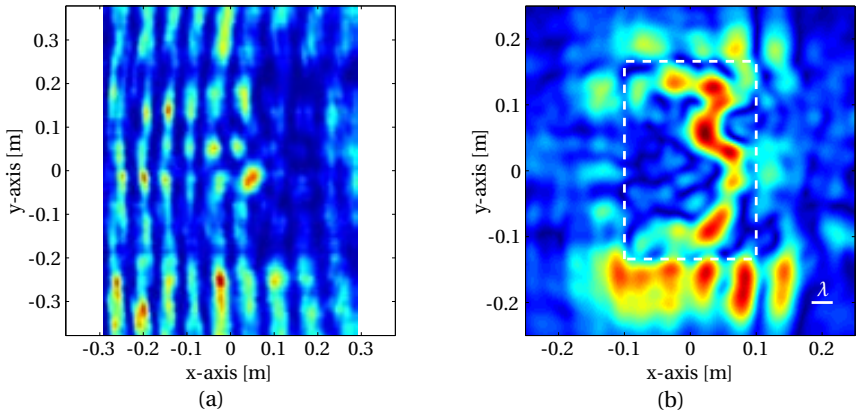

Figure 3.21: (a) Voltage detected as measured from the 16 element X-Band array demonstrator in the Cartesian scene. (b) Recovered image by means of Gabor holography. In white dashed line the 20×30 copper sheet is outlined.

side of the image, where the outer source beam is not present as it is in the simulation, or in the upcoming measurements of the circular scenes.

3.3.4 Circular scene measurement

According to the simulation of the circular scene, two measurements are presented for both 16 and 32 array points. In this scene, the 32 point array is achieved by physically shifting the array half antenna separation and performing a second measurement. As aforementioned in the simulation section, even though the extension of the array is bigger than in the Cartesian scene, at least in one of its directions, the total scanning plane is circularly filtered which will introduce a small degradation in resolution as compared to a whole sized planar scan.

Both the measured interference pattern and the recovered target image are displayed in Fig. 3.22 (a) and (b) respectively, for the 16 pixel array. They are shown to be quite similar to the its simulation as reported in Fig. 3.8 on page 65.

For the 32 element array, both the interference pattern in Cartesian coordinates and the recovered image are shown in Fig. 3.23 (a) and (b). Since with the

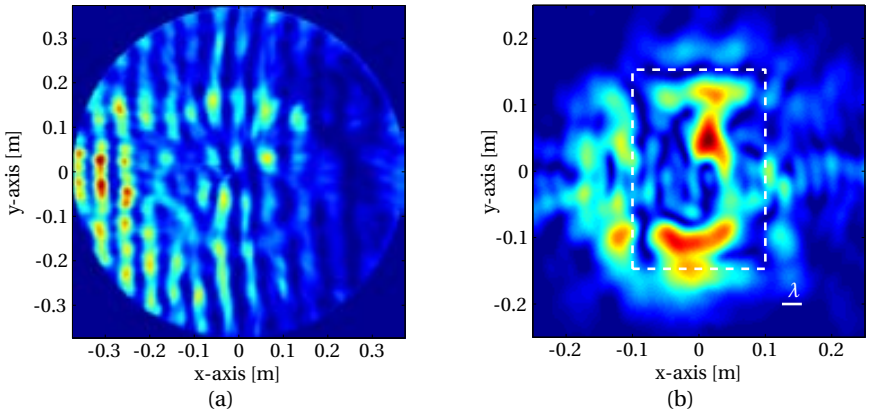

Figure 3.22: (a) Voltage detected as measured from the 16 element X-Band rotary array demonstrator in Cartesian coordinates. (b) Recovered image by means of Gabor holography. In white dashed line the 20 × 30 copper sheet is outlined.

16 element measurement there was some “power leak” in the bottom shape of the number “three” due to the small rim presented by the target at that point, the metal on the base has been extended downwards in order to improve the recovering of the image as can be greatly appreciated by comparing the 16 and 32 element recovered image.

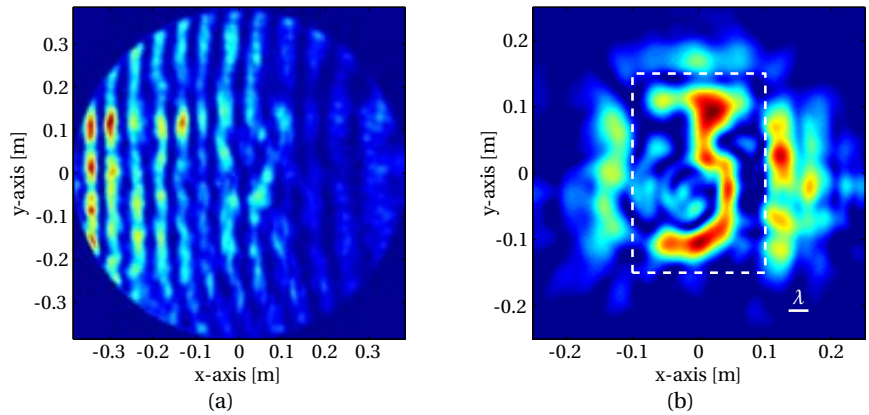

Figure 3.23: (a) Voltage detected as measured from the 2 × 16 element X-Band rotary array demonstrator in Cartesian coordinates. (b) Recovered image by means of Gabor holography. In white dashed line the 20 × 30 copper sheet is outlined.

3.4 Conclusions

In this chapter the design, simulation, fabrication and measurement process has been reported for a one dimension array of Schottky-based detectors to be used in off-axis Gabor holography.

The simulation process of the receiving array has enabled a more efficient design. Available CAD software tools for simulation and design simplifies the design stage of every single project, where the designer is able to test every single step in as much detail as required. In the case of this dissertation multiple techniques have been used to drive the design process. A suitable Matlab design environment has been created, which was intended to be used throughout the entire dissertation. Special care has been taken in order to use the proper approximations to ensure the best design process with the fewer possible computational cost. Special emphasis is placed on describing how every different step has been simulated, not only on this particular chapter, but on the rest of the dissertation.

Once the simulation and design of the array has been described, the manufacture and characterization of the array is reported. Manufacturing has been simplified as much as possible, trying to keep a reduced cost per element. The X-Band frequency range was selected due to lower manufacturing complexity and higher number of available commercial devices and instrumentation. Constructing this array has proven to be a significant test ground to gain the required expertise in order to create higher frequency systems. As an example, two W-Band receiver prototypes are shown in Fig. 3.24. In figure (a), the W-Band frequency up-scaled version of the X-Band receiver presented in this chapter is shown. In (b), an up-close picture of the prototype W-Band radiometer is shown.

Two different schemes have been simulated and experimentally tested. It has been shown that in order to obtain the maximum imaging benefits for a given number of array elements, different solutions have to be taken into account. In this particular case by using a circular scheme approach, instead of a more commonly used Cartesian scheme, not only the total size of the array

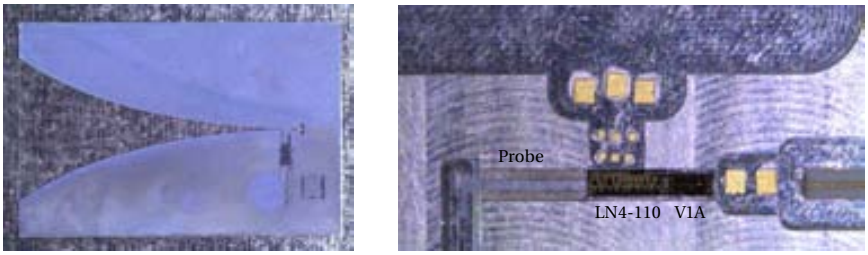

(a) (b)

Figure 3.24: W-Band Prototypes for (a) Millimeter-wave detector based on a *Virgina Diode (VDI)* zero-bias Schottky Detector very similar to the X-Band detector described in current chapter. (b) Radiometer based on a low noise amplifier LN4-110 and a wide-band detector V1A from *HRL Laboratories*.

is effectively doubled, but the mechanical speed and simplicity can be greatly increased.

Simulation and measurement have been shown to be in very good agreement in all presented cases, even while working close to the maximum resolution power of the array.

Two main disadvantages arise from the rotation of the array. First of all the rotation entails a polarization decoupling between transmit and receiving antennas. This effect creates an angular modulation of the sensed field, which must be solved in order to use the array for imaging applications. This issue is solved by combining two different measurements with both horizontal and vertical polarizations, but can also be solved with just performing a single measurement with circularly polarized antennas in one or both ends of the experimental setup (either transmit and/or sensing antennas). The second intrinsic issue of this setup is how to route the low frequency signals out of the array, in the presented experiment a single rotation is measured each time and thus an standard flat ribbon cable is used and untangled each time. However, this will defeat the ultimate purpose of the array, the ability to take multiple acquisitions on a continuous spin. As described, other signal distribution systems must be explored in order to drive both the video signals out and, if required by the video stage, some power supply in.

The circular scanning approach has specially proven less mechanically challenging, both in hardware requirements as well as in software control. Even the repeatability can be greatly improved by using an actual encoder, while the linear stages will require more bulky equipment, as well as costly calibration procedures. Furthermore, linear motorized stages are prone to smearing problems and overall more difficult to fix and maintain.

Future development of this work can be done by using more complex sampling schemes to further improve the circular scenario, for instance obtaining an optimal non-fixed spacing between the elements of the array. This will improve the uneven sample distribution issue that is intrinsic to this approach.

CHAPTER 

OPPOSITE-PHASE HOLOGRAPHY WITH SYNTHESIZED INTERNAL REFERENCE

In the previous chapter the common Gabor off-axis holography was used with exactly the same scheme as envisioned by Gabor and improved by Leith and Upatnieks. The interference of two transmit sources impinging with different angles was used to obtain the image component separation in the spatial frequency domain. The main focus of previous chapter research was carried out in the receiving stage of the setup.

By contrast, the present chapter explores the idea of modifying the transmit antenna stage. Two experiments are going to be develop, first using the same scheme as before, two measurements are going to be taken by shifting the reference angle, with this so called Opposite-Phase reference, the autocorrelation image terms between source and reference are going to be eliminated, thus requiring a smaller spatial frequency bandwidth. The second experiment will place the reference wave inside of the receiving device. This setup allows the creation of ideal reference wave, as for instance pure plane waves, thus

preventing any blocking, removing any unwanted reference antenna taper and also improving the dynamic range of the overall setup. In order to create such an internal reference, a new detector has been manufactured which not only allows the use of this internal reference but also enables the use of the opposite-phase reference, thus taking advantage of both improvements at the same time.

This chapter is divided in three sections. First the the experimental setup and results of the Opposite-Phase Off-Axis Gabor holography is presented. The second section reports the experimental setup and results of the Internal reference approach as well as the actual implementation of the new detector receiver. The third section consists on the conclusions to the chapter.

4.1 Opposite-phase Holography

As discussed on the introduction of this chapter, the first experiment is carried out by using a second reference wave shifted 180°.

By subtracting a recording of the common Gabor hologram described in section 1.5.3 with this second hologram with its reference phase modified by 180°, equation (2.38) becomes

$$I = |S+R|^2 - |S-R|^2 \tag{4.1}$$

which can be also expanded into its image terms as:

$$\begin{aligned} I &= |S|^2 + |R|^2 + S\cdot R^* + S^*\cdot R \\ &\quad -|S|^2 - |R|^2 + S\cdot R^* + S^*\cdot R \\ &= 2\cdot(S\cdot R^* + S^*\cdot R) \end{aligned} \tag{4.2}$$

In equation (4.2) it is finally clear that both source and reference autocorrelations have been removed from the hologram. Furthermore, by using this methodology the desired image terms from both recordings are effectively combined, and therefore the signal to noise ratio is increased by 3 dB with respect to the common hologram. In Fig. 4.1 (a) the spectral energy distribution (SED) of both object and reference are shown in solid area for a simulated hologram.

This image brings a more intuitive approach to the opposite-phase concept. The actual hologram, in black solid line is shown to follow the envelope of the total spectral energy distribution of both autocorrelation terms here represented in solid grey coloured areas.

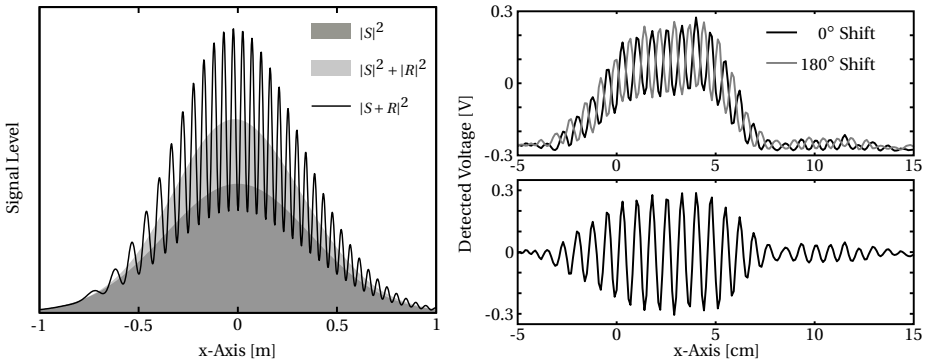

Figure 4.1: (a) Spectral energy distribution of object wave S in solid dark gray area, SED of object S and reference R wave in solid light gray area and actual interference pattern in black line. (b) Top: two measured 100 GHz holograms with 0° and 180° reference phase shifts and (b) opposite-phase hologram comprised of both subtracted holograms.

In order to remove the spectral energy distribution corresponding to the autocorrelation terms, a second hologram recording with its phase shifted by 180° is subtracted from the first one. As shown on Fig. 4.1 (b) top image, the shift on the second hologram makes its interference pattern interchange its constructive/destructive behaviour in the spatial domain. By subtracting both phase-shifted interference patterns (Fig. 4.1 (b) lower image), the low spatial frequencies for both object and reference wavefronts, corresponding to their spectral energy distributions are removed, leaving only the higher spatial frequency terms corresponding to both source and reference cross-correlations.

4.1.1 Experimental setup

The technical feasibility of opposite-phase holograms is tested at the W-Band frequency range in a common off-axis hologram scheme as shown in Fig. 2.1. The terahertz source wave is generated by the V10VNA2 series WR10 Frequency Extension T/R Module (Fig. 4.2:1) from *OML*, while the reference wave is generated by an active multiplier chain from (Fig. 4.2:2) AMC-10-RFH00 from *Millitech*. Both sources are driven by a dual source N524A PNA-X vector network analyser (Fig. 4.2:3) from *Agilent Technologies*. In this setup both wave are radiated by 25° beam-width scalar horn antennas SFH-10-R0000 also from *Millitech*. The required 180° phase-shift has been achieved by increasing the reference distance by $\lambda/2$ with a linear stage micropositioner mechanically fixed to lock on two fixed positions for repeatability purposes.

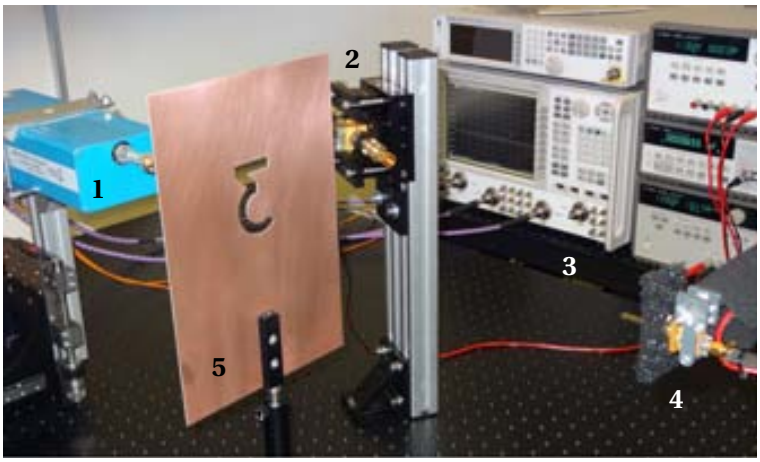

Figure 4.2: Opposite-Phase off-axis hologram W-Band demonstrator setup. The experimental setup is composed of 1: source signal generator, 2: reference wave generator, 3: dual source PNA-X N5242A, 4: millimetre-wave detector mounted on scanner and 5: target under test.

On the receiver stage, the receiver itself is based on a general purpose wideband detector DET-10-RPFW0 (Fig. 4.2:4) from *Millitech* with a custom made 4 cm long open ended rectangular waveguide probe. The detected signal is integrated by a 100 kHz filter and acquired by a 34420A Nano-Voltmeter from *Agi-*

lent Technologies. The receiver is mounted on two 60 cm NLS8 Linear Stages from *Newmark Systems* used in a XZ configuration, as presented in section 3.3.2. Errors due to miss-alignment and precision are less problematic in millimetre-waves than they are in optics, or in the terahertz range, so less stringent requirements and more economic motorized stages can be used. Furthermore, by working at those frequencies there is no need for a vibration isolated optical table in this particular setup.

For this configuration a total scan plane size of 50 × 50 cm with a spatial sampling of 1 mm ($\sim \lambda/3$) on the off-axis reference axis and 5 cm on the vertical axis has been used.

The target (Fig. 4.2:5) is made out of a copper metal sheet with a 3λ width cutout number "3" about 22λ of total height, placed in between the source and scan plane at 35 cm from the probe tip. A close-up of the target is also shown in Fig. 4.3 (c). In order to minimize the interaction between the reference beam and the target, the reference source is placed at the same z-distance as the target with an spatial offset of 20 cm, tilted 30° towards the scan plane origin.

4.1.2 Experimental results

By using the aforementioned setup, two 180° phase-shifted off-axis holograms are acquired. In Fig. 4.3 (a) a single common off-axis hologram is shown, in (b) the opposite-phase hologram is shown, constructed by subtracting the second hologram recorded with its reference phase-shifted 180°, where both object and reference spectral energy distributions have been removed, and hence the resulting signal spans in both the positive and negative range of voltage values. In both Fig. 4.3 (c) and (d) the acquired holograms have been decimated on the off-axis direction up to a sampling interval of 6 mm (2λ). However, by doing this procedure we are not violating the Nyquist sampling theorem in any case, since this will always hold true provided that we consider only a band limited portion of the whole plane wave spectrum.

The plane wave spectrum of the different holograms from Fig. 4.3 are shown by means of their bidimensional Fourier transform in Fig. 4.4. In (a) the plane

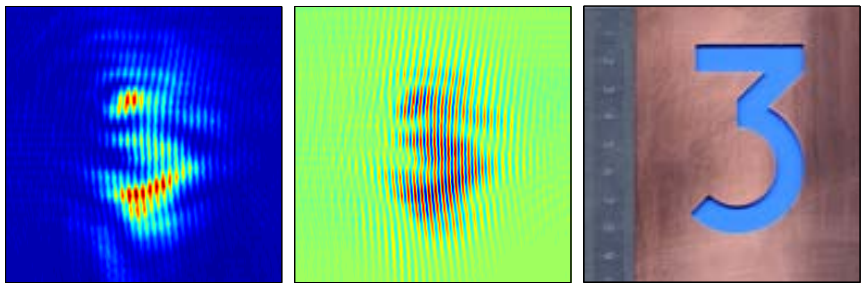

(a) (b) (c)

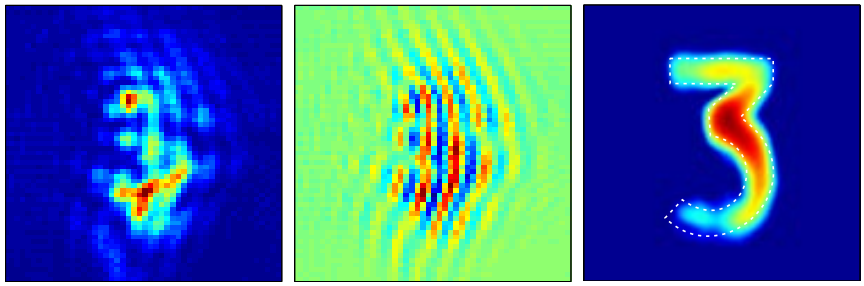

(d) (e) (f)

Figure 4.3: Cropped 30 × 30 cm sections of 100 GHz measurements for the common off-axis hologram (a), the 180° opposite-phase hologram (b), and their corresponding decimated counterparts (d) and (e). (c) corresponds to the actual target under test and (f) the result of the opposite-phase reconstruction process for the Opposite-Phase undersambled hologram (e).

wave spectrum of the single measured hologram is shown, where both autocorrelation and cross-correlated terms are present, but spaced enough so no overlap is present between them. As a consequence, the image can be recovered using the common off-axis holographic process, as introduced in section 2.4.1. In (b) the spectrum of the 180° opposite-phase hologram is shown, where both S and R autocorrelation terms have been removed from the *pws*. In both Fig. 4.4 (c) and (d) the same behavior is also present, nonetheless, the maximum spectral frequency of the hologram has been reduced and therefore both real and virtual image have folded back into a reduced spectra, thus causing the common decimated hologram from Fig. 4.3 (c) to overlap with the autocorrelation terms. On the other hand, the spectral content corresponding to both real

and virtual images for the decimated phase-shifted hologram spectra of Fig. 4.4 (d) remains free from overlap.

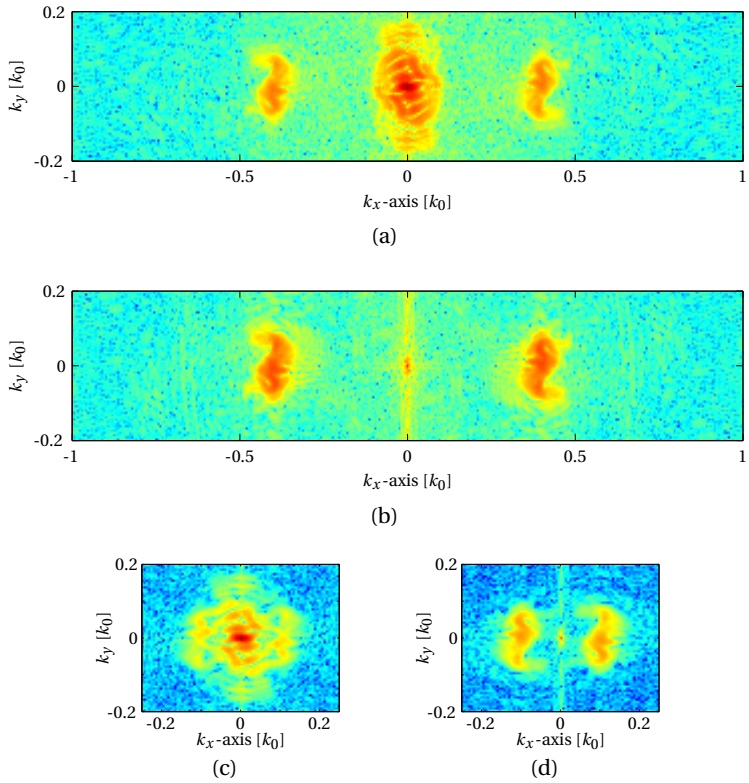

Figure 4.4: Plane wave spectrum of 100 GHz measurements for (a) common off-axis hologram, (b) opposite-phase off-axis hologram and their decimated counterparts (c) and (d) correspondingly, showing the reduced spectral content on the decimated offset axis direction.

Recovering the complex field of the scattered wave from the low-sampled 180° phase-shifted hologram requires exactly the same algorithm used for the common off-axis hologram. Nevertheless, it is important to note that the undersampling may have caused aliasing on the crossed terms, so special care is required in order to choose the appropriate real image term instead of the virtual term. For example in Fig. 4.4 (d), the image term on the right corresponds to the image term on the left in one of the non-decimated spectra as shown on ei-

ther Fig. 4.4 (a) or (b). Direct application of the reconstruction algorithm can be used, given an appropriate reference measure or simulation by taking into account both the low number of samples and the possible folding of the plane wave spectrum. Another method could be used, where the under-sampled measure is actually expanded by zeros, which produces a replicated *pws*, which lead to a proper unfolding of the actual imaging terms.

The actual result of the reconstruction process is shown on Fig. 4.3 (f), it is worth mentioning that even though the actual level change in the image is due to the illumination taper and not caused by the algorithm itself.

4.2 Holography with Internal Reference

Until this very section all mentions to the interfering reference signal have supposed that the wave is of a radiated nature. Nevertheless, this reference wave is not required to be radiated, therefore the superposition of the object wavefront can be accomplished directly inside the receiver itself by means of a guided wave combiner such as couplers, Wilkinson power dividers or hybrids among others.

The main benefit of using a guided (instead of radiated) reference is that the desired reference wave can be synthesized for optimal illumination schemes, such as plane-waves, Gaussian beam shapes, certain tapers, etc. Furthermore, by having a guided reference there is no possible blockage from the object under test and therefore no restriction to the actual spatial angle of the synthesized wave. For instance, another interesting benefit from using an internal reference, although it is not restricted to this method, is the ability to increase the signal level of the intensity hologram above the noise level of the receiving detector by just creating an appropriate reference wave. In fig 4.5 a Gaussian beam field is superposed to both another Gaussian beam coming from a second source representing a separate radiating antenna (a) and a synthesized plane wave (b). It is clearly visible that for a detector with a noise floor of -50 dBm, a huge portion of the interference pattern will not be able to be properly

resolved, meanwhile with the plane wave approach, all the signal can be acquired without any meaningful loose of information, at least prior to the ADC. A second important point that can be extracted from those plots is that in the Gaussian beam approach, the excursion of the data is way bigger than the actual excursion in the synthesized wave. So by using a clever synthesized wave, optimum scenarios for not only the microwave detector but also for the ADC can be obtained, thus further improving the performance of the overall imaging system.

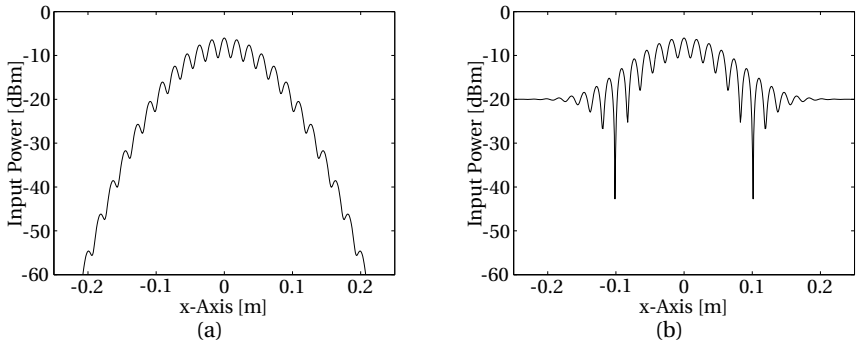

Figure 4.5: Intensity interference pattern between a Gaussian beam and a reference wave consisting on (a) another Gaussian beam and (b) a synthesized plane wave both impinging at a certain spatial frequency.

The internal reference can be both used in single or multiple-element array receivers. In single receivers the desired reference must be provided on each acquisition point. This approach requires a more advanced synthesizer since it has to be fast enough to provide the corresponding amplitude and phase of the desired reference wave for each single point (or sets of points, such as a complete line as discussed in the upcoming sections). If used on an array, it can be further simplified since the reference wave can be provided by a single source with multiple components such as delay lines, couplers or any other distributed component with coupling values as low as 20 or 30 dB. In opposition to mixer arrays where the distribution of enough LO power is one of the main concerns of the actual array design. The low-power required in the reference wave makes this setup really suitable for arrays or even matrices of low

complexity detector-based receivers.

4.2.1 Opposite-Phase with Internal Reference

The introduction of the synthesized reference inside the detector is accomplished by means of coupling a portion of the reference signal to the incoming signal from the antenna. In order to perform the demonstration with a single pixel receptor, a 90° hybrid coupler is used. However the use of 90° couplers means that one of its four ports must be matched to accomplish proper performance in both isolation and balance, even after matching this fourth port half the power of the incoming signal is lost in the matched load resistor.

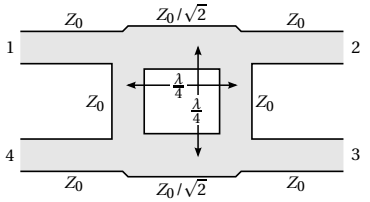

$$\frac{1}{\sqrt{2}}\begin{bmatrix} 0 & 1 & j & 0 \\ 1 & 0 & 0 & j \\ j & 0 & 0 & 1 \\ 0 & j & 1 & 0 \end{bmatrix} \tag{4.3}$$

(a)

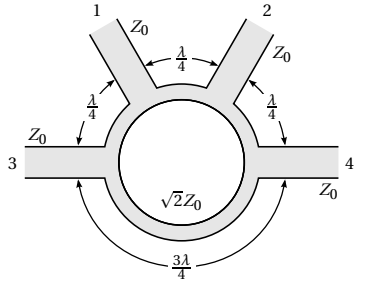

$$\frac{1}{\sqrt{2}}\begin{bmatrix} 0 & 1 & 1 & 0 \\ 1 & 0 & 0 & -1 \\ 1 & 0 & 0 & 1 \\ 0 & -1 & 1 & 0 \end{bmatrix} \tag{4.4}$$

(b)

Figure 4.6: Hybrid couplers for coupling the internal reference wave to the incoming signal for both (a) 90° hybrid and (b) 180° hybrid or rat-race coupler.

By replacing the matching load for a a second microwave detector, the signal is no longer lost and can be used later on the processing stage to improve the SNR of the acquired signal. By substituting the 90° hybrid (Fig. 4.6 (a)), with s-parameter response given by equation (4.3) for a 180° hybrid implemented

as a rat-race coupler (Fig. 4.6 (b)), with s-parameter response given by equation (4.4), the incoming signal is added both with the synthesized reference and with its opposite-phase value, thus obtaining the second measurement required for the opposite-phase technique as shown in section 4.1.

4.2.2 Opposite-Phase Detector with Internal Reference

In order to test feasibility of the Opposite-Phase with internal reference, an X-Band microwave receiver is designed and manufactured based on two diode-based detectors as designed in section 1.4.2. Those detectors are connected to the 180° hybrid sum and difference outputs, as shown in Fig. 4.7 (a).

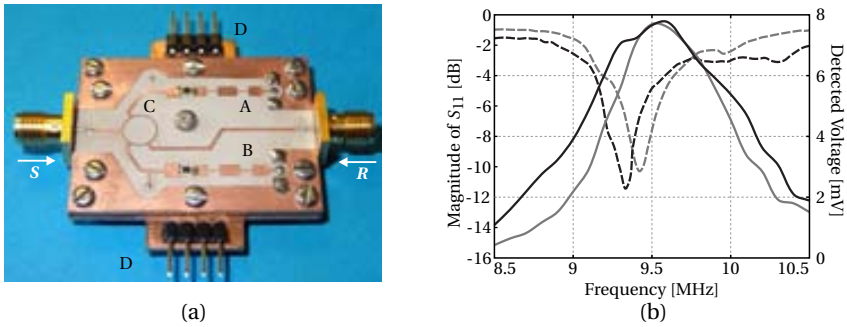

(a) (b)

Figure 4.7: (a) X-Band Microwave detector with internal reference composed of *S*: Scattered signal input, *R*: synthesized Reference input, A and B: diode-based microwave detectors, C: rat-race 180° hybrid and D: outputs and supply of operation amplifiers (other side of the board). (b) characterization of microwave opposite-phase detector by means of its detected output voltage for an input power of -30 dBm (measure is taken before amplification) in dashed line (black for sum and grey for difference branch) and the magnitude of the reflection coefficient in solid line (black for source *S* and grey for internal reference *R* inputs).

The X-Band detector is manufactured on a Rogers RO3010 substrate with low mechanical resistance. Since this board require SMA connectors for the reference and source wave, special care is required since applying even the appropriate amount of torque to the connector will bend, and even break, the RF board. In order to solve this issue both the RF and video board (FR-4 substrate) are mounted on a brass support as shown on the exploded diagram of Fig. 4.8,

which overcomes the fragility of the malleable RO3010 substrate maintaining a good ground for the detector.

On the RF Board two microwave detectors, same ones as described earlier in section 3.2.1, are connected through the 180° rat-race coupler to both signal coming from the antenna input (RF Signal connector in the image) as well as to the synthesized signal used as reference.

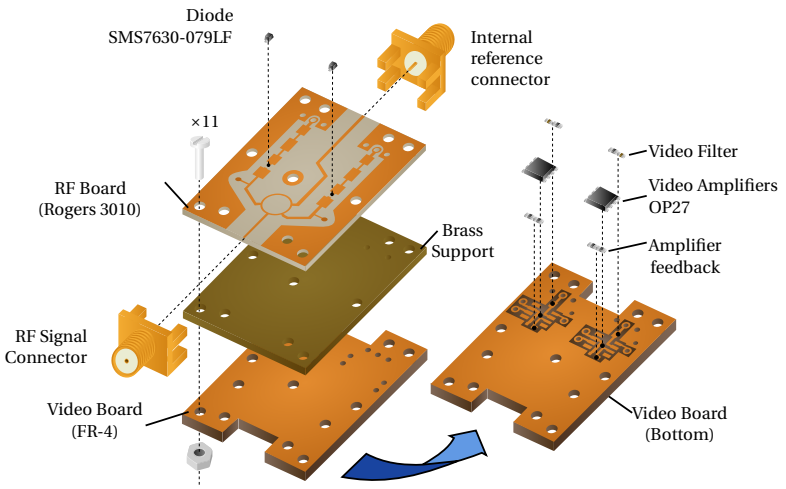

Figure 4.8: Exploded diagram of the microwave X-Band detector mounting and support.

The rectified signal coming from the diodes are driven towards the video board through two header pins that directly connect the signal to the video filters composed of a passive low-pass filter with 100 KHz bandwidth loaded with a 100 kΩ impedance. The signal is then amplified by a low-noise operational amplifier OP27 from *A*nalog Devices in a negative feedback configuration as shown in the circuit of Fig. 4.9.

The amplifier is configured for a total linear gain of 22, which matches the maximum input voltage of the ADC for the maximum power, gain as a function of input power is shown on lower plot of Fig. 4.10 (b). The detected voltage of the receiver with and without the amplification stage is shown on the top plot of (b). Figure 4.10 (a) shows the response of both detectors when applying a phase-shift to the reference wave of arbitrary angles between -180 and 180

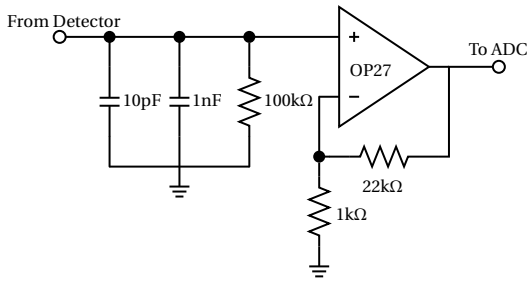

Figure 4.9: Detected voltage versus reference to source input synthesized relative phase-shift. Top: output voltage versus input power before (grey) and after (black) the video amplifier stage. Solid and dashed line corresponds to sum and difference branches while dot-dashed line is the theoretical non-saturated response. Bottom: video gain for both branches, black for sum and grey for difference output.

degrees. As it is shown, the complementary behaviour of both detectors has a good agreement, not showing any deviations on the fabrication at the central frequency with nominal power of -20 dBm, and the amplifier set to 20 dB gain.

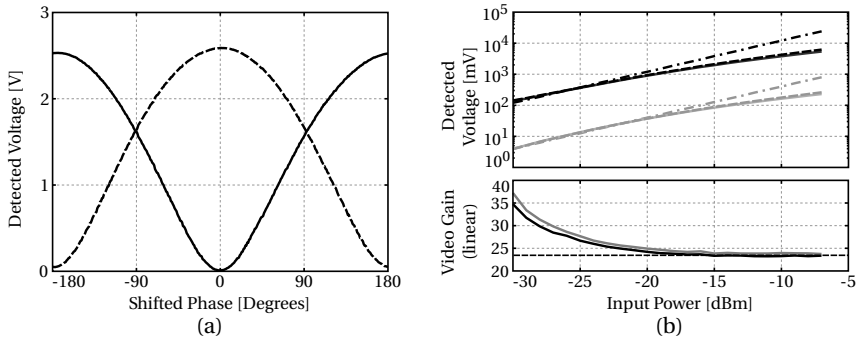

Figure 4.10: (a) Detected voltage versus reference to source input synthesized relative phase-shift. (b) Top: output voltage versus input power before (grey) and after (black) the video amplifier stage. Solid and dashed line corresponds to sum and difference branches while dot-dashed line is the theoretical non-saturated response. Bottom: video gain for both branches, black for sum and grey for difference output.

4.2.3 Quasi-Monostatic Principle

For testing the internal reference, a new setup is considered based on a quasi-monostatic configuration. This new setup has been chosen since it will im-

prove the resolution of our system, taking into account that only one receiver is going to be fabricated to test the aforementioned techniques. In the quasi-monostatic system configuration, both transmit and receiver antennas are really close with a separation as small as possible and thus, the system can be treated as a single transceiver antenna (The monostatic approach only uses one antenna for both transmit and receive).

The quasi-monostatic approach for the X-Band setup is shown in the diagram of Fig. 4.11, as shown, the main setup of the system is based on a two source VNA which will drive both the source antenna (Tx) and the probing antenna (Rx). The required phase shift of the internal reference technique is provided directly by a programmable phase-shift inside the VNA, instead of using the mechanical approach followed on section 4.1.1.

The collection of data points is performed by mechanically scanning the target under test over a flat square lattice in the field of view of both transmitter and receiver.

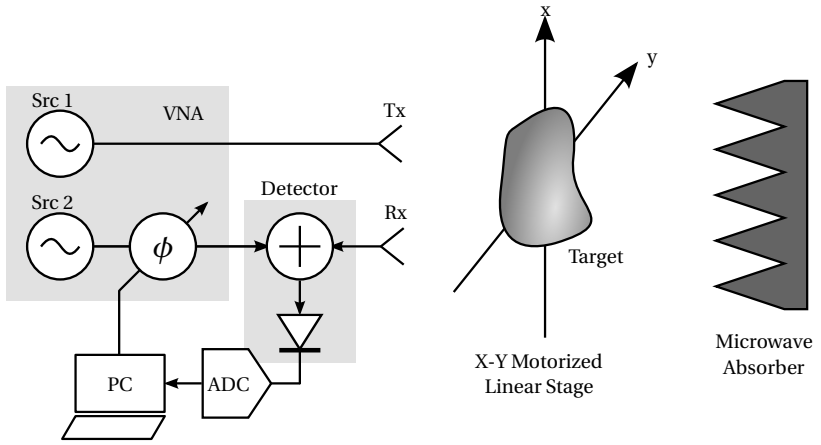

Figure 4.11: Simplified diagram of the quasi-monostatic Gabor holographic imaging system with synthesized internal reference.

Each point in the scan plane $(x', y', 0)$ will take into account only the effect of its own illumination for each scanned point at the target (x, y, z). The phase of the retrieved field can be shown to be twice the phase of a bistatic config-

uration with fixed source, corresponding to the roundtrip phase of the signal, as derived from equation (2.19), the Rayleigh-Sommerfeld Diffraction formula can be simplified to equation (4.5).

$$U'\left(x',y'\right) = \iint_{\Sigma} e^{-j2k_0\sqrt{(x-x')^2+\left(y-y'\right)^2+z^2}}\,dx\,dy \tag{4.5}$$

In order to reconstruct the target image, the backward-wave propagation (Section 2.2.3) in conjunction with the Fast Fourier Transform algorithm (FFT) is used which can be summarized into:

$$U\left(x,y,z\right) = \mathscr{F}^{-1}\left\{\mathscr{F}\left\{U'\left(x',y',0\right)\right\}e^{-jk_z z}\right\} \tag{4.6}$$

where $\mathscr{F}$ is the two dimensional FFT, and k_z corresponds to the z component of the roundtrip wave-number as stated by

$$k_z = \sqrt{4k_0^2 - k_x^2 - k_y^2} \tag{4.7}$$

The main advantage of the quasi-monostatic approach is that it is able to resolve the image with twice the resolution, since the phase change is also twice that of a common bistatic imaging system as we have been using previously throughout the dissertation.

On the other hand its main disadvantage is that it requires a different illumination for each scan point so, either the transmit/receive pair or the target have to be scanned, this makes it difficult to implement in some configurations such as in a multiple-pixel approach where the quasi-monostatic principle might not hold depending on antenna separation and distance to the target.

4.2.4 Holographic Techniques

Three different imaging techniques will be used with this same setup, first of all since the source wave is based on a VNA, the receiver antenna can be connected directly into one of its receivers and thus a coherent image can be acquired which will serve as the resolution goal for the other techniques. In antenna metrology acquiring both amplitude and phase of an illuminated Antenna Under Test (AUT) is known as holography, in order to differentiate from

the other holographic techniques reported in this dissertation, this technique is going to be referred as "Phase & Amplitude holography". Since complete knowledge of the scattered field is acquired, a simple backward-wave propagation is used to recover the image of the target. Precisely the fact of acquiring both amplitude and phase entails its main disadvantage since amplitude and phase heterodyne receivers are more difficult to design, manufacture and replicate at terahertz or even millimeter-wave frequencies, as discussed on the introduction of the thesis.

In addition to the Off-Axis Synthesized Internal reference technique, a second phase-less measurement based on an Inline Hologram will also take advantage of the internal reference detector.

With in-line holography the reference wave is usually emitted along with the source. In this method, the twin-image problem is not avoided since both images overlap on the *pws* origin along with source and reference autocorrelation terms.

In such a setup, different approaches exist in order to overcome the twin-image overlap mainly by using multiple measurements. The most common technique used takes into account the use of multiple measurements with different phase-shifted references, but other techniques such as phase-retrieval have been also used to overcome the twin-image problem and recover the scattered field [107, 108].

By using the phase-shifting method [109], four quadrature intensity (I_θ) measurements are required with the reference shifted by $\theta = 0°$, $90°$, $180°$ and $270°$.

$$I_\theta = |S + R_0 e^{j\theta}|^2 \tag{4.8}$$

where the $S \in \mathbb{C}$ is the complex scattered wave, and $R_0 \in \mathbb{R}$ the amplitude of the reference wave. By evaluating equation (4.8) by all the angular values of the reference, equations (4.9-4.12) are obtained.

$$I_0 = |S|^2 + |R|^2 + R_0\left(S + S^*\right) \tag{4.9}$$

$$I_{\frac{\pi}{2}} = |S|^2 + |R|^2 + jR_0\left(S - S^*\right) \tag{4.10}$$

$$I_{\pi} = |S|^2 + |R|^2 - R_0\left(S^* + S\right) \tag{4.11}$$

$$I_{\frac{3\pi}{2}} = |S|^2 + |R|^2 + jR_0\left(S^* - S\right) \tag{4.12}$$

By direct manipulation of those four intensity measurements, equation (4.13) is obtained where the constant real value $4R_0$ can be removed or disregarded as an scale factor.

$$\begin{aligned} I_T &= I_0 + jI_{\frac{\pi}{2}} - I_{\pi} - jI_{\frac{3\pi}{2}} \\ &= 4R_0S \end{aligned} \tag{4.13}$$

The main disadvantage of in-line holography in microwaves is precisely the requirement of multiple measurements, since CCD camera-like receivers are not yet available and thus long times have to be used for acquiring the whole set of measurement. However, by using the Opposite-phase detector the required measurements can be reduced to only two, since we are already taking care of complementary angles.

4.2.5 Experimental Setup

The quasi-monostatic approach for all configurations follows the diagram on Fig. 4.11. It is based on the PNA-X N5242A Vector Network Analyser from *Agilent Technologies* with options 400 (*Dual Source*) and 460 (*Integrated True Mode Stimulus Application*). The VNA creates two signals, both source and reference, with a software controlled phase-shift between the two (in the case of the coherent acquisition, the microwave detector is discarded and the output of the receiving antenna is connected directly to one of the VNA receivers).

Two different antennas for the receiving stage have been contemplated. First of all, an integrated quasi-yagi antenna as used in chapter 3 and shown in Fig. 4.12 (a). However, this particular antenna was too wide and therefore

too much coupling from the source was present. Rendering this antenna approach useless for this particular setup. Finally, another open-ended circular waveguide antenna was used (same one as the source), allowing a much more lower coupling between them.

In order to position the antennas, a vertical rail with antenna holders is used, as described in section 3.3.1. The antennas are separated 10 cm between them in order to reduce the mutual coupling, this setup can be observed in Fig. 4.12 (b), where also the X-Band detector is shown directly connected to the receive antenna.

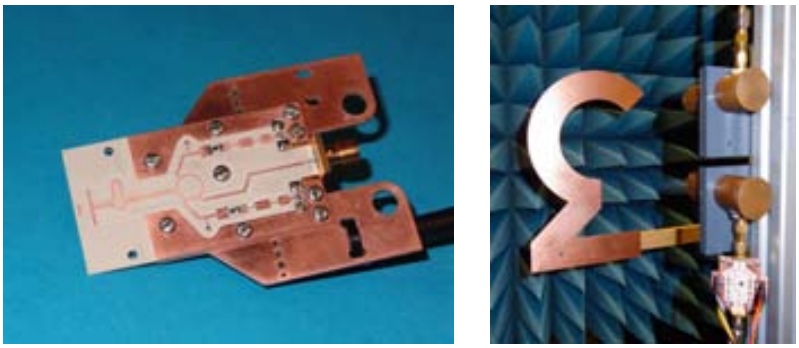

(a) (b)

Figure 4.12: (a) X-Band detector with quasi-yagi antenna, discarded due to high coupling with source antenna. In this setup, the Video board has been modified so it can directly connect to the vertical rail. In (b) the final quasi-monostatic antenna setup is shown. Upper circular open-ended waveguide antenna is used as the transmit or source antenna and is connected directly to the VNA. The lower antenna is connected to the opposite-phase internal reference X-Band detector. In the picture the target under test is also shown composed of a copper metal sheet number "3", with total size of 16×27 ($5.3 \times 9\lambda$) and path width of 4 cm (1.3λ). (upside down due to position of XZ motorized stage).

For this experimental setup, the target is the complementary of the one used in the previous chapter, this means that in this setup the source will be reflected on the target and thus a similar image will be acquired. The target used is a number "3" silhouette cut out from a copper metal sheet as shown in Fig. 4.12 (b). The width of the number's path is 4 cm or 1.3λ, with a total size of 16×27 ($5.3 \times 9\lambda$). The target is mounted to the NLS8 Motorized stages

(from *Newmark Systems*) mounted on a XZ configuration. In this setup, the scan plane size is 50 × 50 cm, while the sampling on the horizontal axis is set to continuous acquisitions, the vertical direction is scanned at 5 mm steps.

4.2.6 Experimental Results

Phase & Amplitude Holography

This measurement is performed by connecting the transmit antenna to the source of an VNA, and the receiver antenna to one of its receivers. Different approaches can be followed to obtain this same measurement with the VNA, obtaining a coherent measurement of the transmission S_{21} parameter is sufficient although most VNA comes with multiple inputs and outputs to drive directly the desired signals from source or to one of the receivers.

In Fig. 5.1 (a) and (b) the amplitude and phase of the received scattered field is shown as directly obtained with the internal coherent receiver of the VNA. By direct backward-wave propagation, the image of the target is reconstructed in the image plane as shown in (c). It is worth mentioning that vertical stripes present in the figures correspond to reflection of the source wave in the vertical axis of the scan.

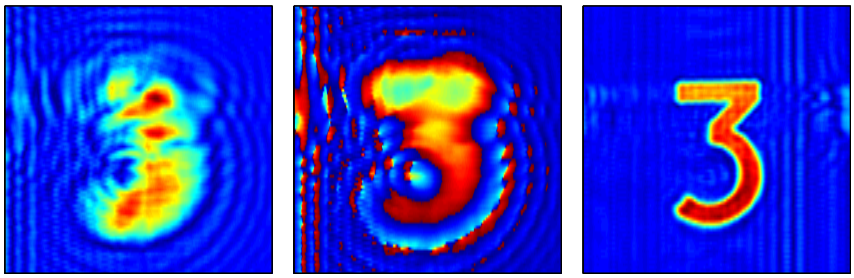

(a) (b) (c)

Figure 4.13: Complex field from coherent acquisition in both amplitude (a) and phase (b). Target image (c) by backward-wave propagation. All image sizes are 50cm x 50cm.

Off-Axis Gabor Holography with internal reference

In the off-axis Gabor approach, the opposite-phase microwave detector is connected to the receiver antenna. The second source of the VNA drives the internal reference of the detector and introduces the required phase-shift for each scanned line, this means that in this case the axis with lower sampling is the one used as the offset-axis, and as such it has to cope with a more stringent sampling. This approach has been used since the continuous movement of the scanner does not allow the VNA to switch the phase of the signal as quickly as it should since some settling time needs to be taken into account. By using this approach, the phase of a whole horizontal line is set when the current line scan is finished. While the scanner moves in the Z axis to go for the new line, the VNA has more than enough time to settle the change in phase.

The opposite-phase hologram is depicted on Fig. 4.14 (a), as a direct subtraction of both detected voltage outputs. The recovered field before removing the reference signal is shown both in amplitude (b) and phase (c). It is clearly visible in this phase picture that the reference has been synthesized as a pure plane-wave since the phase change is in perfect horizontal planes. Although thanks to this synthesized reference, the removal of the reference wave is straightforward, no approximations, simulations or measurements have to be performed, since the phase of the reference wave is well known for each point of the measurement, obtaining the image in (d). Finally, by applying the backward-wave propagating filter, the target image is obtained in figure (e). By direct visual inspection with the coherent approach, it is clear that this method suffers from a lower resolution, mainly caused by the spatial spectrum filtering that needs to be applied in order to select one of the imaging terms. However, by comparing this final image with the ones carried out in the previous chapter (Fig. 3.21) it can be clearly stated that by using the quasi-monostatic approach with opposite-phase better resolution can be achieved, although this is not a fair comparison between experiments, since this was not the purpose of neither setup.

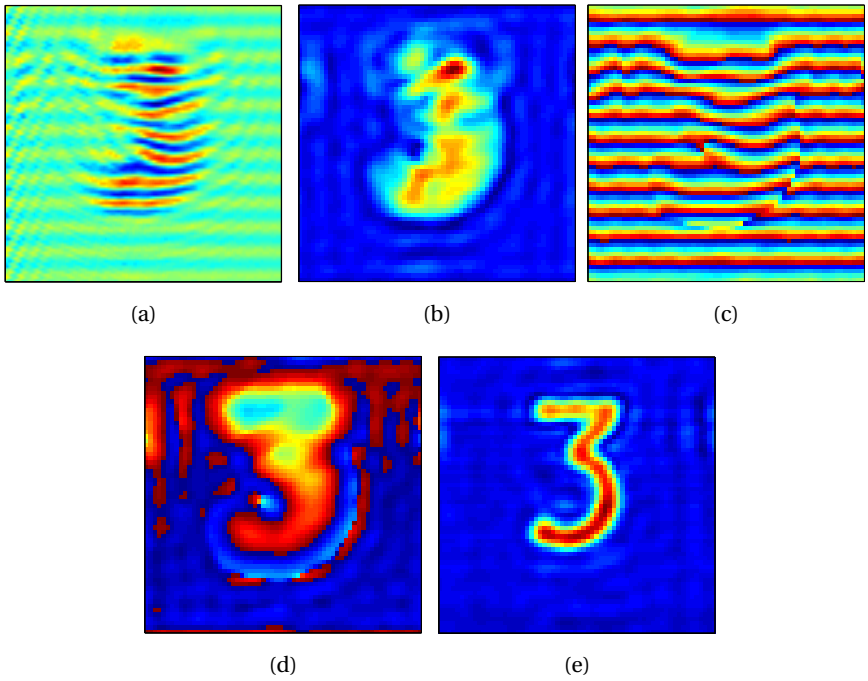

Figure 4.14: Gabor Holographic Off-Axis measured opposite-phase interference pattern (a), recovered complex field amplitude (b), field phase before (c) and after (d) removal of the synthesized reference wave. (e) Reconstructed target image. All image sizes are 50 × 50 cm.

In-Line Holography

In order to perform the in-line holographic experiment, the same setup presented for off-axis gabor holography is used. Rather than using a different phase-shift for each scanned line, the synthesized phase remains constant for the whole measurement. As seen on the previous section, four measurements are required and hence four acquisition with different synthesized phases should be used. Nevertheless, by using the opposite-phase outputs of the receiver, only two measurements are required to obtain both the real and imaginary terms from equation (4.13).

In Fig. 4.15 (a to d) the four quadrature measurements, as acquired with the

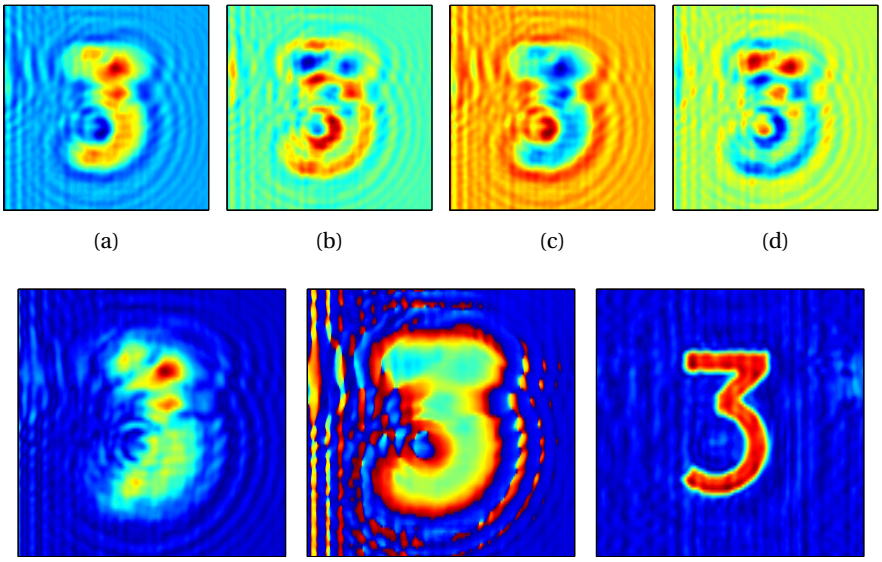

Figure 4.15: Inline holographic measurements for synthesized reference phase: (a) 0°, (b) 90°, (c) 180° and (d) 270°. Recovered complex field amplitude (e), field phase (f) and (g) reconstructed target image. All image sizes are 50cm x 50cm.

microwave detector are shown for the different phase-shift values. By direct combination of (a) and (c), as provided by the microwave detector for the first 0-180° pair with the second (b) and (d) 90-270° pair, we directly recover the field as shown both in amplitude (e) and phase (f). By using the backward-wave propagation method once more, the resulting image of the target is obtained as shown in (e). With in-line holography, the resulting image is qualitatively as good as with the coherent image.

Resolution Comparison

The resolution of the imaging system is commonly described as the ability to resolve any given detail on the object under test. Even though it is common to theoretically express this quantity by the Point Spread Function (PSF), the

use of more convenient methods such as the Line Spread Function (LSF) or the Edge-Response are often used. In our case, the Edge-Response method can be directly applied to previously reported images.

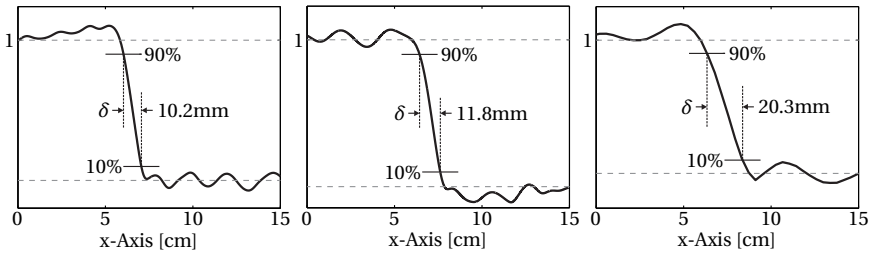

Figure 4.16: Resolution comparison using the Edge-Response method between: (a) Coherent Holography, (b) In-Line Holography and (c) Off-Axis Holography.

The Edge-Response function is the response of the imaging system to an steep step (it is worth to mention that the LSF can be found by direct differentiation of the step response). Ideally an infinite length step going from zero to full reflection should be used. In reported experiments, the contrast between the Radar Absorbent Material (RAM) material and the straight metallic section of the number "3" are used to obtain the step for the different system configurations, as shown on Fig. 4.16 for the coherent system (a), the In-Line Hologram (b) and the Off-Axis Hologram (c).

The resolution of the system is obtained by measuring the rising time of the step from 10% to 90%. For our systems the resolutions obtained are 10.2 mm for the coherent system, 11.8 mm for the in-line hologram and 20.3 for the off-axis hologram. Both the coherent and the in-line hologram system provide a similar resolution of about $\lambda/3$, while the off-axis hologram configuration has half the resolving power as expected ($2/3\lambda$). This is due to the reduction in the plane wave spectrum, which at most (such as in the current case) will be half the spectra of the whole *pws*.

4.3 Conclusions

This chapter introduces two separate concepts, which by the end of the chapter are used together in order to improve the holographic techniques. Different imaging techniques and strategies have been followed to obtain better and faster images while keeping the detector inexpensive and simple.

The so called Opposite-Phase Holography is a basic technique which allows to reduce the effect of one of the major issues in Off-Axis Holography, the autocorrelation of both source and reference. Unfortunately, this improvement can not completely overcome the twin-image problem. However, the spatial frequency contributions of both image and virtual image terms can be shifted down towards the center of the plane-wave spectrum origin, effectively diminishing the minimum required bandwidth by half, thus allowing to lower constrictions on either sampling, or minimum wave orientation angle. This procedure can be achieved either by reducing the reference wave incident angle or by taking control of the plane wave spectrum alias, as shown with the decimated example of this chapter. This technique has been validated by using a W-Band setup. The required 180° phase different between acquisitions has been achieved by using a $\lambda/2$ mechanical shift.

The second concept presented in this chapter is the use of an internal reference wave to drive the holographic process, instead of a radiated wave. This internal wave can be generated by different methods such as using mechanical or electrical shifters, synthesizing the signal directly with a Direct Digital Synthesis (DSS), or in our case directly using the VNA as a probe of concept.

The control of how the reference wave is synthesized also allows the possibility of obtaining better illumination schemes, where the reference is no longer limited by the shape and position of the antenna, but can be precisely altered line by line, or even point by point, to create the optimum illumination for a given configuration; no target blockage, no spillover and no degraded reference power across the entire scan plane are some of the ultimate benefits of using this approach. With the synthesized reference, it is possible to adequate the signal to the hardware since we now have the ability to shape the reference

in such a way that, for instance, the interference pattern of the hologram can be exactly placed on the linear response of the detector diode, or at least just above its noise level.

In the last section of this chapter the X-Band detector presented in chapter 3 has been replicated and combined through a rat-race 180° hybrid coupler, which not only allows to introduce the internal synthesized reference phase but also allows to acquire opposite-phase hologram at the same time.

The actual feasibility of the Opposite-Phase Holography with internal reference has been tested. In the mean time with this setup different recovering techniques have been tested and compared. A quasi-monostatic setup has been chosen for this experiment, by using this technique the resolution of the system is actually doubled. This same setup has been also used for obtaining In-Line holography images (thus proving the versatility of the internal synthesized reference wave), where the source is combined with different reference phases. A clever combination of those quadrature phased acquisitions allows to recover the amplitude and phase for the target scattered and received field. This two phase-less techniques have been finally compared to a coherent acquisition. Comparing all setup resolution, by means of the Edge-Response method, it is clearly visible that both the Coherent image as well as the In-Line Holographic image share practically the same resolution (double the resolution thanks to the use of the quasi-monostatic setup). Using only the Opposite-Phase holography only delivers half of that resolution. This is caused mainly by the spatial-frequency filtering imposed on the Off-Axis holography approach.

Future work entails the creation of 1D array of opposite-phase detectors with internal synthesised reference, mimicking the rotatory array of chapter 3. In this device both amplitude and phase will be fixed by using distributed components along the signal path. Using this internal reference to drive the holographic process will allow the array to be driven by a low power source, instead of the very complex high power LO required in coherent multi-pixel receivers. This could probe to be an interesting starting point towards faster and cheaper imaging acquisition devices for multiple applications.

CHAPTER 

APPLICATION IMAGES

This chapter introduces a few measured acquisition of different targets, trying to showcase some applications as well as introduce some additional features worth mentioning as found in the practical application of the aforementioned techniques during the course of the dissertation.

5.1 Flat targets and standing waves

Flat targets have been used throughout the dissertation in order to simplify the acquisition and improve the contrast of the images. However, going from a simple two dimensional flat plane to something in three dimensions entails an increase on complexity, since the metrics of the system will now have to change. No longer the resolution of the system is the only parameter into account, but others such as depth and ambiguity must also be taken into account.

In order to show this issue, a flat target with depth information has been created as shown in Fig. 5.1 (a). Using the Protomat S62 milling machines, con-

centric annular grooves have been milled with different sizes and in steps of 100 μm with a total of 8 grooves or 800 μm.

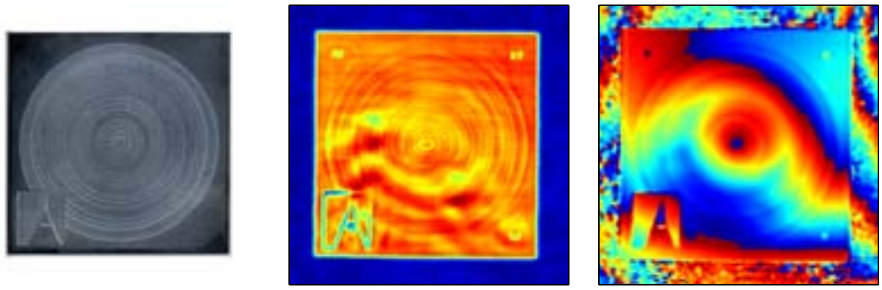

(a) (b) (c)

Figure 5.1: (a) Flat aluminium plate (20 × 20 cm) used as target, millet in 100 μm steps with a 800 μm depth UAB Logo. Recovered amplitude (a) and phase (b) are depicted as recovered by means of In-Line holography at W-Band.

This experiment has been carried out at W-Band frequencies. In-Line Holography, as discussed on chapter 4, has been chosen for this setup due to its increased resolution in comparison to the X-Band setup. The recovered image is shown in Fig. 5.1 for both amplitude (a) and phase(b). It clear that even though the border of the target is as sharp as presented in previous chapters, this is not the case for the details of the flat plane. In fact one of the first things to notice is this diagonal ripple present in the shape. This is caused by coupling between the flat plane and the receiver. However the important details on this flat plane, better observed in the amplitude image, are the scattering of the edges as shown in the annular rings, where there is one extra annular ring per edge which confuses completely the shape of the milled panel, but this issue is specially accused on the UAB logo, where the deep straight walls grooved in the panel create this non-existsing hole in the target. By looking into the phase recovered picture, all this effects are greatly reduced, but the dynamic range of the phase is so small between grooves that only the logo is clearly depicted. The coupling effect between plate and antenna is significantly worse in the phase where different grooves are all shown to have the same recovered phase.

Another issue with this figures can be appreciated by looking in the screws on the amplitude image, where it is clear that even though the flat screws are clearly shown thanks to their grooves (screws not present on actual photography), showing the great resolution achievable with this setup, they are shown not to be in focus. Focusing by using this technique requires an exact position, or an optimization to get the best focus point, however with a three-dimensional object this can not be achieved since multiple depths will require multiple focus points (focus stacking) or using a different approach which shows a greater depth of field.

This coupling between caused by a strong standing wave between the antenna (and also all the measurement equipment) and the target itself is better shown in Fig. 5.2.

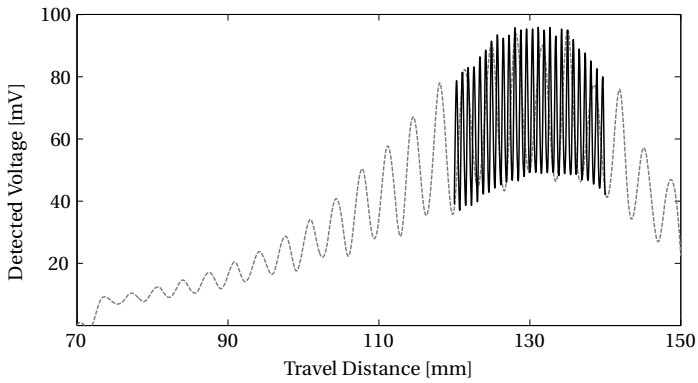

Figure 5.2: The dashed-line in grey is a coarse measurement to determine the focal point with 1 mm steps, the maximum excursion of the ripple is shown. In black solid line the a fine sampling of 0.1 mm has been carried out showing the real frequency of the ripple. This experiment has been carried out by a quasi-optical system in a quasi-monostatic configuration.

This ripple has been generated by moving a flat target across the focus point of a quasi-optical system. The imaging system focus point is found by using a coarse sampling of 1 mm, showing this broad ripple, while a finer scanning resolution is carried out only on the peak of the focus point showing the actual ripple produced by the standing wave between the system and the target. In this case a huge depth uncertainty will be present since the ripple standard

deviation is almost 20 μV with a mean value (on the peak) of less than 70 μV making the depth prediction invalid for relative depths greater than 2 μm. The experiment has been carried out at a frequency of 186 GHz.

5.2 Antenna Beam-width and Security Applications

In this section a couple of configurations with different types of antennas are shown. In order to test this experiments the setup has been based on a possible imaging system for Security applications, and a dummy metal gun has been used as a more realistic target as shown in Fig. 5.3 (a). Using this type of target enables us to additionally discuss qualitatively the possibility of detecting threads in security applications, in this case solely by looking at its shape through different system configurations. It has to be noted that in this experiments the dummy metal gun is always in the best possible situation with respect to the scanner, and no concealment has been taken into consideration.

(a) (b) (c)

Figure 5.3: (a) Actual photography of the dummy metal gun used as target. Recovered image of the dummy metal gun in both amplitude (b) and phase (c). This measurement has been carried out with a quasi-static setup at W-Band frequencies using two 25° antennas.

In Fig. 5.3 both amplitude and phase of the recovered image are shown for the quasi-monostatic setup at W-Band frequencies by using two 25° beam-width SFH-10-R0000 horn antennas from *Millitech*. All the major features of the gun are clearly shown although the strongest signal comes from the per-

fectly aligned flat surfaces on the barrel. The plastic grip shows the composite interior where the gas tank of the BB gun is stored.

For the second setup, the overall system configuration is kept the same. Both horn antennas are exchanged with 4 cm long rectangular wave-guides. This custom-made probes have not been properly characterized but should have a beam-width in excess of 50% in its narrower plane. The recovered image on Fig. 5.4 is visually quite different from the previous one. In this particular case the use of wider probes allows a much more finer detail to be extracted both in amplitude (a) and phase (b). This finer resolution comes in exchange of dynamic range since the signal is lower with respect to the background, but also more diffraction appears on the edges of every single detail, thus creating a more cluttered image. This diffraction effect can be appreciated not only in the object itself but also on the reconstruction of the borders of the image, corresponding to the edges of the gun wood holder, and it is directly caused by computing a higher number of spatial frequency components, caused by both the use of the probe antenna in combination with the In-Line holographic process since no component is discarded as in the case of Off-Axis Holography.

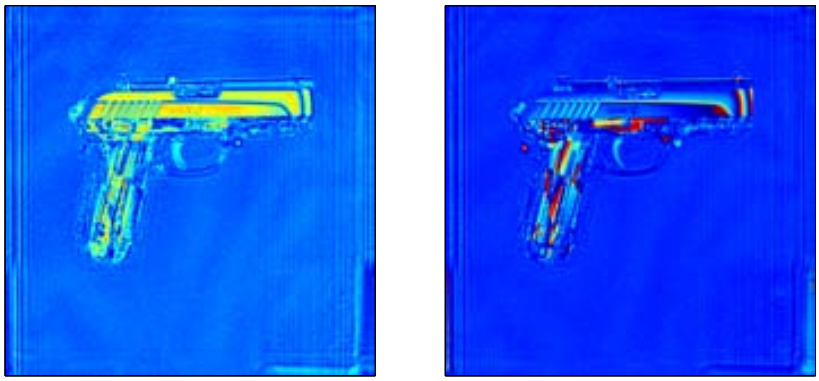

(a) (b)

Figure 5.4: Recovered image of the dummy metal gun in both amplitude (a) and phase (b). This measurement has been carried out with a quasi-static setup at W-Band frequencies using two high-beam width custom-made rectangular wave-guide antennas.

With the aforementioned system enough detail is shown, at least to detect this type of threads, a gun or a knife, by taking into account only the resolution of the system, and overlooking other possible issues such as the limitations of the systems regarding the orientation of targets. Can thus the frequency be reduced in order to drastically decrease the cost of a possible imaging system for security applications? In order to answer this question a final measure has been carried out with the X-Band setup obtaining the results in Fig. 5.5. In this case although using high beam-width antennas the resolution of the system is so diminished that only basic shapes can be discerned. However, some details are still clearly discernible such as the barrel, the grip and even the trigger, although only distinguishable on the phase measurement.

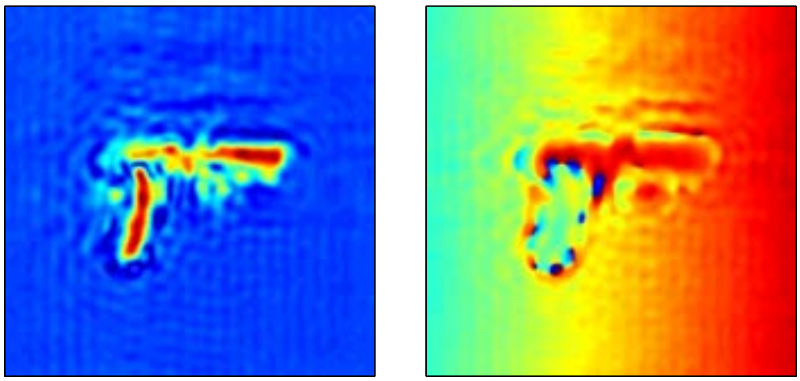

(a) (b)

Figure 5.5: Recovered image of the dummy metal gun in both amplitude (a) and phase (b). This measurement has been carried out with a quasi-static setup at X-Band frequencies using two high-beam width custom-made circular wave-guide antennas.

On the technical side of this section, a comparison between two different antenna beam-widths shows that the higher the beam-width the greater the perceivable resolution, although care must be taken in order to properly control the power requirements of the system since the emitted power will not be as focused as with the higher directivity antennas.

5.3 Conclusion

In this chapter two different experiments have been presented showing different effects present in previously reported setups. The quasi-monostatic configuration has been chosen again, since it provides better resolution which will enable us to compare other characteristics of those setups.

Section 5.1 shows the effect of coupling between a flat plane an the receiver, and how this fact is translated in the recovered image where even slight amplitude and phase deviations could have a bigger impact in both amplitude and phase rather than the target shape itself. Three major issues have been described, the uncertainty of determining a depth from the measurement, the scattering occurring depending on the input angle and the most important issue, the presence of the standing wave in the measurement that can become an important error if characteristics must be determined such as depth distances or relative positions.

The second experiment has the double purpose of introducing the reader to a more realistic example, while showing the effect of different antenna beamwidths. As shown, the use of a bigger beam-width implies acquiring a bigger spatial frequency spectrum and thus obtaining a more detailed representation of the object under test. This is of the out-most importance for applications such as Non-Destructive Testing, where small cracks and features must be detected. However, for this particular application it is clear that using narrower beam-width antennas is enough (resolution-wise) and this will provide the design with a greater dynamic range and a better range since the energy of the active imaging system is more focused.

One of the important points from this experiment is the fact that no matter what technique the system uses, having the phase in addition to the amplitude always gives additional information. So while creating a detection algorithm for any type of application, it will be advisable to use both amplitude and phase components to achieve a better success rate for the detection of desired features, threats or defects.

Finally, it is worth mentioning the comparison between the W-Band and

the X-Band gun measurement. Although the resolution is far better at W-Band, certain types of applications will not care for such great detail and therefore some imaging systems may be able to operate at lower frequencies, 10 or 20 GHz without requiring such expensive equipment as Millimter-wave or even Terahertz ones. For instance, a hand-help scanner with X-Band detectors such as presented in this dissertation may be enough to detect concealed weapons on a pad-down type of scenario with a very low price tag.

CHAPTER 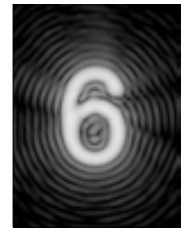

CONCLUSION AND FUTURE WORK

6.1 Conclusion

This thesis has been focused on the use of intensity-only holographic measurements for image acquisition, specifically using Off-Axis holography at both X-Band and W-Band frequencies. There is a current trend to use well known and established techniques with new technology advances in millimeter-wave and submillimeter-wave devices, and this thesis has reviewed the use of such holographic techniques and proposed some different new setups for imaging applications.

In chapter 3 of this dissertation a circular rotating array of receivers has been proposed, mainly focused on reducing the acquisition time. Special care has been taken into consideration to reduce the cost of the array by using straightforward receivers which can be easily scaled towards higher frequencies. An X-Band demonstrator array composed of 16 zero-bias Schottky diode detectors has been designed and constructed in order to test its behaviour and acquire

the required background to scale towards higher frequencies such as W-Band or beyond, not only on the microwave front-end but also on the video stage, acquisition, as well as software manipulation in order to follow the whole process from taking an actual measurement to recovering the final image.

The following key conclusions can be derived from the aforementioned work:

- A 16 element array has been constructed at X-Band based on Zero-bias Schottky detectors.
- For the used setup, 16 elements separated 0.8λ is not enough to recover a clean image, and therefore a second measurement using 0.4λ has been used with an effective 32 elements array, which successfully reduces artefacts on the 2D interpolation.
- In the circular scenario, the interference pattern can be constructed of different polarization components, using linearly polarized antennas as both transmit and receive elements. However, a second measurement is required.
- Devise new setups and different approaches to the same problem can further extend the usability of devices such as in the case of the reported array where using a Circular instead of a Cartesian scan can greatly increase speed and scan area.
- Representation of the actual recovered image is subject to additional improvements in post-processing. Changing the image dynamic range, colors or scale can dramatically change the recognition of the image.
- The lack of amplification on the array receivers greatly reduces the usable range of the imaging system, which limits possible applications. Other receiver architectures using low-noise amplifiers can be taken into account, however scaling towards higher-frequencies will probe to be much more challenging as we go up in frequency.

- Working with high-frequency devices requires specialized equipment and highly trained personnel.

In chapter 4, two different improvements are introduced to the common Off-Axis holographic technique. The first one consists on combining two measurement with their reference shifted 180° leading to the so called Opposite-Phase off-axis holography. By using this second shifted hologram the following conclusions can be derived:

- With Opposite-Phase technique, source and reference autocorrelations are removed from the interference pattern intensity.
- By removing autocorrelations no overlap is present between them and both cross-correlations.
- Cross-correlations can be shifted down towards the origin of the *PWS*. Shifting of the cross-correlated terms can be achieved by lowering the impinging reference angle or reducing the actual sampling frequency, care must be taken in order to satisfy Nyquist sampling theorem for band-limited signals.
- Combination of both the common and the 180° shifted hologram increase signal to noise ratio by 3dB.
- The resulting combination of both holograms entails and improved ADC dynamic range usage, since only the interference pattern is acquired.
- The main drawback of opposite-phase is that it requires a second measurement, or a second receiver.
- Additionally opposite-phase requires a phase-shifting device to introduce the 180° phase shift.

The second improvement is called synthesized internal reference and consists on adding the reference wave directly to the receiver, which entails the following conclusions:

- By adding the internal reference there is no need to radiate the reference wave and thus no blockage is present on the scheme.
- Since the reference wave is not radiated, there is no spillover or non-homogeneities on the scan area caused by the propagation of the reference wave, or defects on the antenna.
- The reference wave can be synthesized to create optimum illumination schemes.
- The reference wave can be synthesized to drive the intensity hologram over the receiver noise-floor.
- In order to recover the image in Off-Axis holography, there is no need to approximate the reference wave since we have full control over it.
- Synthesizing the reference wave can be accomplished by multiple approaches(some more costly than others). It may be created by using fixed values for either amplitude and/or phase by using distributed elements such as couplers and delay lines, or it can be programatically generated such as with a DSS, VNA or phase-shifting devices.
- On an array, the reference wave must be distributed to each pixel, but the low power level required in holography makes it much more easier than in other architectures such as in heterodyne receivers.
- If using a programmable synthesized reference on a single pixel scanner, every single point can have a different amplitude and/or phase. In a multi-pixel array or matrix, different approaches can be used to drive single pixels, entire lines or sub-matrices with different amplitudes or phases.

However extra potential of the aforementioned improvements can be unleashed by combining both approaches. The combined system will inherit all benefits for both Opposite-Phase and Internal Reference. With an appropriate

receiver design, it will solve some of its intrinsic issues. For instnace, the 180° phase-shift required for Opposite-Phase can be integrated inside the receiver easily by using an appropriate coupler for the internal reference, however it still requires a second measurement which can be done on the fly by using a second receiver. A new basic pixel has been reported by duplicating the low-cost pixel of Chapter 3, combining it through a 180° coupler, one of its inputs being the antenna, while the second one drives the internal reference.

Finally in Chapter 4 the receiver has been used to test other methods such as the presented In-Line holography where two 90° shifted reference are applied to create four actual measurements, which combined together are able to overcome completely the twin-image problem. Those methods have been compared by using a quasi-monostatic setup which effectively doubles the resolution of our system by scanning both transmit and receive antenna at the same time. A resolution comparison between In-Line and Off-Axis Holography along with a direct heterodyne measurement is carried out with the following conclusions

- The quasi-monostatic setup entails a two-fold resolution improvement, although it is highly challenging to implement on a multi-pixel receiver.

- In-Line Holography has roughly the same resolution as an amplitude and phase measurement, although it requires 4 different acquisitions (2 in our case).

- Off-Axis holography achieves half the resolution of In-Line holography.

In Chapter 5, different experiments and setups are used which lead to the following conclusions:

- Standing waves between the object under test and the transmitter/receiver are crucial for image recovering algorithms, specially when using almost all-flat targets.

- Both phase & amplitude bring different information that should be used for automatic image recognition algorithms.

- Lower frequency imaging systems may be feasible to use in imaging applications where low-resolution images can still be usable.

- Antenna probe design must be considered for optimum results according to the actual application. Higher beamwidth antennas are required for narrow or small detail detection, while high directivity antennas are more suitable for applications like stand-off security scanners where resolution is not as critical, but where the system can benefit from a more collimated beam in terms of range and unwanted reflections.

6.2 Future work

As future work, this thesis has established the starting point to build a W-Band demonstrator for imaging applications at video frame rate speeds with a circular rotating array, which should be further improved by creating an Opposite-phase with internal synthesized array. Future task should involve:

- Optimization of the sampling grid to account for non-homogeneous 2D Cartesian sampling, or usage of Polar FFT techniques.

- Routing of video signals and DC power lines by using a rotary joint or an RF/optical stage will unlock the full speed capabilities of the circular array.

- Low electro-magnetic noise non-stepper motors used along with a high-speed encoder. Having non-stepper motors will increase the rotation speed and will provide a cleaner electromagnetic environment for the video and acquisition stage of the receiver. Having an encoder will provide precise positioning of each sample point without requiring expensive and complex calibration setups.

- Acquisition board should be substituted by single ADCs mounted as close to the detector as possible in order to diminish noise converting the signals to digital as soon as they are detected.
- Linear polarized antennas should be substituted by circular polarized ones in either transmit, receive or ideally both in order to remove the second required measurement.
- The introduction of an internal synthesized reference to the circular scheme will change the sampling topology and thus require a change on the recovering algorithm, furthermore the optimal synthesized reference wave scheme should be obtained for the circular array.
- Use of more realistic three-dimensional objects instead of flat targets, depending on target application.
- Manufacturing capabilities should be procured to cope with the high technical requirements of W-Band systems.

On the other hand, a more in-depth analytical and rigorous treatment of the different subsystems should be taken into considerations to further exploit all hardware capabilities, such as optimum integration time, minimum required quantification levels for proper reconstruction or the optimum antenna beam-with pattern for a given range and application. Furthermore a more rigorous quantification of recovered image quality should be researched and employed in order to remove the subjective and qualitative comparison among recovered images.

BIBLIOGRAPHY

[1] I. T. U. (ITU), "Itu-r v.431-7, nomenclature of the frequency and wavelewave band used in telecommunications," *Recommendations: V Series*, 2000-05. [Online]. Available: www.itu.int

[2] P. Siegel, "Thz instruments for space," *Antennas and Propagation, IEEE Transactions on*, vol. 55, no. 11, pp. 2957–2965, 2007.

[3] D. Fixsen, E. Cheng, J. Gales, J. C. Mather, R. Shafer, and E. Wright, "The cosmic microwave background spectrum from the full cobe firas data set," *The Astrophysical Journal*, vol. 473, no. 2, p. 576, 1996.

[4] D. Doyle, G. Pilbratt, and J. Tauber, "The herschel and planck space telescopes," *Proceedings of the IEEE*, vol. 97, no. 8, pp. 1403–1411, 2009.

[5] M. Tarenghi, "The atacama large millimeter/submillimeter array: Overview & status," *Astrophysics and Space Science*, vol. 313, no. 1-3, pp. 1–7, 2008.

[6] A. Wootten, "Alma capabilities for observations of spectral line emission," in *Science with the Atacama Large Millimeter Array*. Springer, 2008, pp. 9–12.

[7] M. Scarfi, M. Romano, R. Di Pietro, O. Zeni, A. Doria, G. Gallerano, E. Giovenale, G. Messina, A. Lai, G. Campurra *et al.*, "Thz exposure of whole blood for the study of biological effects on human lymphocytes," *Journal of Biological Physics*, vol. 29, no. 2-3, pp. 171–176, 2003.

[8] C. J. Strachan, P. F. Taday, D. A. Newnham, K. C. Gordon, J. A. Zeitler, M. Pepper, and T. Rades, "Using terahertz pulsed spectroscopy to quantify pharmaceutical polymorphism and crystallinity," *Journal of Pharmaceutical Sciences*, vol. 94, no. 4, pp. 837–846, 2005.

[9] P. Taday, I. Bradley, D. Arnone, and M. Pepper, "Using terahertz pulse spectroscopy to study the crystalline structure of a drug: A case study of the polymorphs of ranitidine hydrochloride," *Journal of pharmaceutical sciences*, vol. 92, no. 4, pp. 831–838, 2003.

[10] K. Humphreys, J. Loughran, M. Gradziel, W. Lanigan, T. Ward, J. Murphy, and C. O'Sullivan, "Medical applications of terahertz imaging: a review of current technology and potential applications in biomedical engineering," in *Engineering in Medicine and Biology Society, 2004. IEMBS '04. 26th Annual International Conference of the IEEE*, vol. 1, 2004, pp. 1302–1305.

[11] C. Yu, S. Fan, Y. Sun, and E. Pickwell-MacPherson, "The potential of terahertz imaging for cancer diagnosis: A review of investigations to date," *Quantitative imaging in medicine and surgery*, vol. 2, no. 1, p. 33, 2012.

[12] S. Kharkovsky and R. Zoughi, "Microwave and millimeter wave nondestructive testing and evaluation - overview and recent advances," *Instrumentation Measurement Magazine, IEEE*, vol. 10, no. 2, pp. 26–38, 2007.

[13] S. Kharkovsky, J. Case, M. Abou-Khousa, R. Zoughi, and F. Hepburn, "Millimeter-wave detection of localized anomalies in the space shuttle external fuel tank insulating foam," *Instrumentation and Measurement, IEEE Transactions on*, vol. 55, no. 4, pp. 1250–1257, 2006.

[14] P. Parasoglou, E. P. J. Parrott, J. Zeitler, J. Rasburn, H. Powell, L. Gladden, and M. Johns, "Quantitative moisture content detection in food wafers," in *Infrared, Millimeter, and Terahertz Waves, 2009. IRMMW-THz 2009. 34th International Conference on*, 2009, pp. 1–2.

[15] H. Yoneyama, M. Yamashita, S. Kasai, H. Ito, and T. Ouchi, "Application of terahertz spectrum in the detection of harmful food additive," in *Infrared and Millimeter Waves, 2007 and the 2007 15th International Conference on Terahertz Electronics. IRMMW-THz. Joint 32nd International Conference on*, 2007, pp. 281–282.

[16] A. J. L. Adam, P. C. M. Planken, S. Meloni, and J. Dik, "Terahertz imaging of hidden paint layers on canvas," in *Infrared, Millimeter, and Terahertz Waves, 2009. IRMMW-THz 2009. 34th International Conference on*, 2009, pp. 1–2.

[17] J. Caumes, A. Younus, S. Salort, B. Chassagne, B. Recur, A. Ziegle, A. Dautant, and E. Abraham, "3d millimeter wave imaging of xviiith dynasty egyptian sealed pottery," in *Infrared, Millimeter and Terahertz Waves (IRMMW-THz), 2011 36th International Conference on*, oct. 2011, pp. 1 –2.

[18] D. Woolard, E. Brown, M. Pepper, and M. Kemp, "Terahertz frequency sensing and imaging: A time of reckoning future applications?" *Proceedings of the IEEE*, vol. 93, no. 10, pp. 1722–1743, 2005.

[19] R. M. Woodward, "Terahertz technology in global homeland security," in *Defense and Security*. International Society for Optics and Photonics, 2005, pp. 22–31.

[20] Y. Ogawa, S. Hayashi, C. Otani, and K. Kawase, "Terahertz sensing for ensuring the safety and security," *PIERS Online*, vol. 4, no. 3, pp. 396–400, 2008.

[21] R. Appleby and R. Anderton, "Millimeter-wave and submillimeter-wave imaging for security and surveillance," *Proceedings of the IEEE*, vol. 95, no. 8, pp. 1683–1690, 2007.

[22] H.-B. Liu, H. Zhong, N. Karpowicz, Y. Chen, and X.-C. Zhang, "Terahertz spectroscopy and imaging for defense and security applications," *Proceedings of the IEEE*, vol. 95, no. 8, pp. 1514–1527, 2007.

[23] P. F. Taday, "Applications of terahertz spectroscopy to pharmaceutical sciences," *Philosophical Transactions of the Royal Society of London. Series A: Mathematical, Physical and Engineering Sciences*, vol. 362, no. 1815, pp. 351–364, 2004.

[24] K. Kawase, Y. Ogawa, Y. Watanabe, and H. Inoue, "Non-destructive terahertz imaging of illicit drugs using spectral fingerprints," *Opt. Express*, vol. 11, no. 20, pp. 2549–2554, 2003.

[25] B. Schulkin, B. Clough, D. Brigada, N. Laman, T. Tongue, and X.-C. Zhang, "Progress toward handheld thz spectrometry," in *Infrared, Millimeter, and Terahertz Waves, 2009. IRMMW-THz 2009. 34th International Conference on*, 2009, pp. 1–2.

[26] J.-Y. Lu, L.-J. Chen, T.-F. Kao, H.-H. Chang, H.-W. Chen, A.-S. Liu, Y.-C. Chen, R.-B. Wu, W.-S. Liu, J.-I. Chyi, and C.-K. Sun, "Terahertz microchip for illicit drug detection," *Photonics Technology Letters, IEEE*, vol. 18, no. 21, pp. 2254–2256, 2006.

[27] R. Appleby and H. Wallace, "Standoff detection of weapons and contraband in the 100 ghz to 1 thz region," *Antennas and Propagation, IEEE Transactions on*, vol. 55, no. 11, pp. 2944–2956, 2007.

[28] M. C. Kemp, P. Taday, B. E. Cole, J. Cluff, A. J. Fitzgerald, and W. R. Tribe, "Security applications of terahertz technology," in *AeroSense 2003*. International Society for Optics and Photonics, 2003, pp. 44–52.

[29] R. Appleby, "Passive millimetre wave imaging and seenrity," in *Radar Conference, 2004. EURAD. First European*, 2004, pp. 275–278.

[30] R. Anderton, R. Appleby, J. Borrill, D. Gleed, S. Price, N. Salmon, G. Sinclair, and A. Lettington, "Prospects of imaging applications," 1997.

[31] K. Mizuno, Y. Wagatsuma, H. Warashina, K. Sawaya, H. Sato, S. Miyanaga, and Y. Yamanaka, "Millimeter-wave imaging technologies and their applications," in *Vacuum Electronics Conference, 2007. IVEC '07. IEEE International*, 2007, pp. 1–2.

[32] R. Appleby, "Passive millimetre–wave imaging and how it differs from terahertz imaging," *Philosophical Transactions of the Royal Society of London. Series A: Mathematical, Physical and Engineering Sciences*, vol. 362, no. 1815, pp. 379–393, 2004.

[33] P. Coward and R. Appleby, "Comparison of passive millimeter-wave and ir imagery in a nautical environment," in *SPIE Defense, Security, and Sensing*. International Society for Optics and Photonics, 2009, pp. 730 904–730 904.

[34] R. Appleby, P. Coward, and J. N. Sanders-Reed, "Evaluation of a passive millimeter-wave (pmmw) imager for wire detection in degraded visual conditions," in *Proceedings of SPIE*, vol. 7309, 2009, p. 73090A.

[35] D. Sheen, D. McMakin, T. Hall, and R. Severtsen, "Active millimeter-wave standoff and portal imaging techniques for personnel screening," in *Technologies for Homeland Security, 2009. HST '09. IEEE Conference on*, 2009, pp. 440–447.

[36] N. Llombart, K. Cooper, R. Dengler, T. Bryllert, and P. Siegel, "Confocal ellipsoidal reflector system for a mechanically scanned active terahertz imager," *Antennas and Propagation, IEEE Transactions on*, vol. 58, no. 6, pp. 1834–1841, 2010.

[37] K. Cooper, R. Dengler, N. Llombart, B. Thomas, G. Chattopadhyay, and P. Siegel, "Thz imaging radar for standoff personnel screening," *Terahertz Science and Technology, IEEE Transactions on*, vol. 1, no. 1, pp. 169–182, 2011.

[38] N. Llombart, R. Dengler, and K. Cooper, "Terahertz antenna system for a near-video-rate radar imager [antenna applications]," *Antennas and Propagation Magazine, IEEE*, vol. 52, no. 5, pp. 251–259, 2010.

[39] J. Parron, H. Rossel, P. de Paco, G. Junkin, and O. Menendez, "Millimeter-wave scene simulation using blender," *Proceedings of XXV Simposium Nacional de Union Cientifica Internacional de Radio, URSI 2010*, 2010.

[40] K. Cooper, R. Dengler, N. Llombart, T. Bryllert, G. Chattopadhyay, E. Schlecht, J. Gill, C. Lee, A. Skalare, I. Mehdi, and P. Siegel, "Penetrating 3-d imaging at 4- and 25-m range using a submillimeter-wave radar," *Microwave Theory and Techniques, IEEE Transactions on*, vol. 56, no. 12, pp. 2771–2778, 2008.

[41] J. Booske, R. Dobbs, C. Joye, C. Kory, G. Neil, G.-S. Park, J. Park, and R. Temkin, "Vacuum electronic high power terahertz sources," *Terahertz Science and Technology, IEEE Transactions on*, vol. 1, no. 1, pp. 54–75, 2011.

[42] G. Chattopadhyay, "Technology, capabilities, and performance of low power terahertz sources," *Terahertz Science and Technology, IEEE Transactions on*, vol. 1, no. 1, pp. 33–53, 2011.

[43] E. Ojefors, B. Heinemann, and U. Pfeiffer, "Active 220- and 325-ghz frequency multiplier chains in an sige hbt technology," *Microwave Theory and Techniques, IEEE Transactions on*, vol. 59, no. 5, pp. 1311–1318, 2011.

[44] A. Maestrini, I. Mehdi, J. Siles, J. Ward, R. Lin, B. Thomas, C. Lee, J. Gill, G. Chattopadhyay, E. Schlecht, J. Pearson, and P. Siegel, "Design and characterization of a room temperature all-solid-state electronic source tunable from 2.48 to 2.75 thz," *Terahertz Science and Technology, IEEE Transactions on*, vol. 2, no. 2, pp. 177–185, 2012.

[45] J. V. Siles, G. Chattopadhyay, E. Schlecht, C. Lee, R. Lin, J. Gill, J. Ward, C. Jung, I. Mehdi, P. Siegel, and A. Maestrini, "Next generation solid-

state broadband frequency-multiplied terahertz sources," in *Antennas and Propagation Society International Symposium (APSURSI), 2012 IEEE*, 2012, pp. 1–2.

[46] T. Phillips and J. Keene, "Submillimeter astronomy [heterodyne spectroscopy]," *Proceedings of the IEEE*, vol. 80, no. 11, pp. 1662–1678, 1992.

[47] R. Blundell and C.-y. E. Tong, "Submillimeter receivers for radio astronomy," *Proceedings of the IEEE*, vol. 80, no. 11, pp. 1702–1720, 1992.

[48] S. Shitov, O. Koryukin, A. Uvarov, M. A. Bukovsky, Y. Uzawa, T. Noguchi, M. Takeda, Z. Wang, M. Krough, and A. Vystavkin, "Study on sis mixers for alma band-10," in *Physics and Engineering of Microwaves, Millimeter and Submillimeter Waves and Workshop on Terahertz Technologies, 2007. MSMW '07. The Sixth International Kharkov Symposium on*, vol. 1, 2007, pp. 219–221.

[49] B. Thomas, J. Gill, A. Maestrini, C. Lee, R. Lin, S. Sin, A. Peralta, and I. Mehdi, "An integrated 520-600 ghz sub-harmonic mixer and tripler combination based on gaas mmic membrane planar schottky diodes," in *Infrared Millimeter and Terahertz Waves (IRMMW-THz), 2010 35th International Conference on*, 2010, pp. 1–2.

[50] H.-W. Hubers, "Terahertz heterodyne receivers," *Selected Topics in Quantum Electronics, IEEE Journal of*, vol. 14, no. 2, pp. 378–391, 2008.

[51] A. Karpov, D. Miller, F. Rice, J. Stern, B. Bumble, H. Leduc, and J. Zmuidzinas, "Low noise 1 thz-1.4 thz mixers using nb/al-aln/nbtin sis junctions," *Applied Superconductivity, IEEE Transactions on*, vol. 17, no. 2, pp. 343–346, 2007.

[52] M. Justen, M. Schultz, T. Tils, R. Teipen, S. Glenz, P. Pẗz, C. E. Honingh, and K. Jacobs, "Sis flight mixers for band 2 of the hifi instrument of the herschel space observatory," in *Infrared and Millimeter Waves, 2004 and 12th International Conference on Terahertz Electronics, 2004. Conference*

Digest of the 2004 Joint 29th International Conference on, 2004, pp. 437–438.

[53] S. Shitov, O. Koryukin, Y. Uzawa, T. Noguchi, A. Uvarov, M. Bukovski, and I. Cohn, "Design of balanced mixers for alma band-10," *Applied Superconductivity, IEEE Transactions on*, vol. 17, no. 2, pp. 347–350, 2007.

[54] Q.-J. Yao, Z.-H. Lin, J. Li, and S.-C. Shi, "Experiment on terahertz imaging with an nbn sis detector," in *Antennas, Propagation and EM Theory, 2008. ISAPE 2008. 8th International Symposium on*, 2008, pp. 493–495.

[55] J. Zmuidzinas and P. Richards, "Superconducting detectors and mixers for millimeter and submillimeter astrophysics," *Proceedings of the IEEE*, vol. 92, no. 10, pp. 1597–1616, 2004.

[56] P. Richards, "Bolometers for infrared and millimeter waves," *Journal of Applied Physics*, vol. 76, no. 1, pp. 1–24, 1994.

[57] M. O. Reese, "Superconducting hot electron bolometers for terahertz sensing," Ph.D. dissertation, Citeseer, 2006.

[58] J. Gao, M. Hajenius, Z. Q. Yang, J. J. A. Baselmans, P. Khosropanah, R. Barends, and T. Klapwijk, "Terahertz superconducting hot electron bolometer heterodyne receivers," *Applied Superconductivity, IEEE Transactions on*, vol. 17, no. 2, pp. 252–258, 2007.

[59] M. Hajenius, J. Baselmans, J. Gao, T. Klapwijk, P. De Korte, B. Voronov, and G. Golt́sman, "Low noise nbn superconducting hot electron bolometer mixers at 1.9 and 2.5 thz," *Superconductor Science and Technology*, vol. 17, no. 5, p. S224, 2004.

[60] S. Shiba, Y. Irimajiri, T. Yamakura, H. Maezawa, N. Sekine, I. Hosako, and S. Yamamoto, "3.1-thz heterodyne receiver using an nbtin hot-electron bolometer mixer and a quantum cascade laser," *Terahertz Science and Technology, IEEE Transactions on*, vol. 2, no. 1, pp. 22–28, 2012.

[61] W. Zhang, W. Miao, S.-L. Li, K.-M. Zhou, S. Shi, J. Gao, and G. Goltsman, "Measurement of the spectral response of spiral-antenna coupled superconducting hot electron bolometers," pp. 1–1, 2013.

[62] S. Cherednichenko, V. Drakinskiy, T. Berg, P. Khosropanah, and E. Kollberg, "Hot-electron bolometer terahertz mixers for the herschel space observatory," *Review of scientific instruments*, vol. 79, no. 3, pp. 034 501–034 501, 2008.

[63] B. Thomas, A. Maestrini, D. Matheson, I. Mehdi, and P. de Maagt, "Design of an 874 ghz biasable sub-harmonic mixer based on mmic membrane planar schottky diodes," in *Infrared, Millimeter and Terahertz Waves, 2008. IRMMW-THz 2008. 33rd International Conference on*, 2008, pp. 1–2.

[64] European Space Agency, "N° 11-2013: Herschel closes its eyes on the universe," in *ESA Press Releases*, 7-May-2013. [Online]. Available: http://www.esa.int/For_Media/Press_Releases/Herschel_closes_its_eyes_on_the_Universe

[65] T. Crowe, R. Mattauch, H. Roser, W. Bishop, W. C. B. Peatman, and X. Liu, "Gaas schottky diodes for thz mixing applications," *Proceedings of the IEEE*, vol. 80, no. 11, pp. 1827–1841, 1992.

[66] B. Thomas, "Etude et réalisation d'une tête de réception hétérodyne en ondes submillimétriques pour l'étude des atmosphères et surfaces de planètes," Ph.D. dissertation, Observatoire de Paris, 2004.

[67] A. Kerr, M. Feldman, and S. Pan, "Mma memo 161 receiver noise temperature, the quantum noise limit, and the role of the zero-point fluctuations."

[68] J. E. Carlstrom and J. Zmuidzinas, "Millimeter and submillimeter techniques," *Reviews of Radio Science*, vol. 1995, 1993.

[69] Skyworks, "Mixer and detector diodes," Application Note, Tech. Rep., August 19, 2008.

[70] D. M. Pozar, "Microwave engineering, 3rd," *Danvers, MA: Wiley*, 2005.

[71] F. Mohammed, M. Bain, F. Ruddell, D. Linton, H. Gamble, and V. Fusco, "A novel silicon schottky diode for nltl applications," *Electron Devices, IEEE Transactions on*, vol. 52, no. 7, pp. 1384–1391, 2005.

[72] S. Gearhart and G. Rebeiz, "A monolithic 250 ghz schottky-diode receiver," *Microwave Theory and Techniques, IEEE Transactions on*, vol. 42, no. 12, pp. 2504–2511, 1994.

[73] W. Lucas, "Tangential sensitivity of a detector video system with r.f. preamplification," *Electrical Engineers, Proceedings of the Institution of*, vol. 113, no. 8, pp. 1321–1330, 1966.

[74] J. Hesler and T. Crowe, "Nep and responsivity of thz zero-bias schottky diode detectors," in *Infrared and Millimeter Waves, 2007 and the 2007 15th International Conference on Terahertz Electronics. IRMMW-THz. Joint 32nd International Conference on*, 2007, pp. 844–845.

[75] G. Chattopadhyay, K. Cooper, R. Dengler, T. Bryllert, E. Schlecht, A. Skalare, I. Mehdi, and P. Siegel, "A 600 ghz imaging radar for contraband detection," in *Proceeding of 19th International Symposium on Space Terahertz Technology*, 2008, pp. 300–303.

[76] D. Gabor, "Holography, 1948-1971," *Proceedings of the IEEE*, vol. 60, no. 6, pp. 655 –668, june 1972.

[77] W. Kock and F. Harvey, "Sound wave and microwave space patterns," *Bell Syst. Tech. J*, vol. 20, pp. 564–587, 1951.

[78] A. Anderson, "Microwave holography," *Electrical Engineers, Proceedings of the Institution of*, vol. 124, no. 11, pp. 946 –962, november 1977.

[79] E. N. Leith and J. Upatnieks, "Reconstructed wavefronts and communication theory," *J. Opt. Soc. Am.*, vol. 52, no. 10, pp. 1123–1128, Oct

1962. [Online]. Available: http://www.opticsinfobase.org/abstract.cfm?URI=josa-52-10-1123

[80] D. Gabor and W. P. Goss, "Interference microscope with total wavefront reconstruction," *J. Opt. Soc. Am.*, vol. 56, no. 7, pp. 849–856, Jul 1966. [Online]. Available: http://www.opticsinfobase.org/abstract.cfm?URI=josa-56-7-849

[81] D. Rochblatt and B. Seidel, "Microwave antenna holography," *Microwave Theory and Techniques, IEEE Transactions on*, vol. 40, no. 6, pp. 1294–1300, 1992.

[82] J. Ala-Laurinaho, T. Hirvonen, and A. Raisanen, "Optimization of a submillimeter wave hologram catr," in *Antennas and Propagation Society International Symposium, 1997. IEEE., 1997 Digest*, vol. 1, 1997, pp. 136–139 vol.1.

[83] R. Larson, J. Zelenka, and E. Johansen, "A microwave hologram radar system," *Aerospace and Electronic Systems, IEEE Transactions on*, vol. AES-8, no. 2, pp. 208–217, 1972.

[84] L. Gregoris and K. Iizuka, "Visualization of internal structure by microwave holography," *Proceedings of the IEEE*, vol. 58, no. 5, pp. 791–792, 1970.

[85] N. Farhat and W. Guard, "Millimeter wave holographic imaging of concealed weapons," *Proceedings of the IEEE*, vol. 59, no. 9, pp. 1383–1384, 1971.

[86] J. W. Goodman, *Introduction to Fourier optics*. McGraw-hill New York, 1968, vol. 2.

[87] C. A. Balanis, *Advanced engineering electromagnetics*. Wiley New York, 1989, vol. 205.

[88] H. H. Arsenault, "Alternate way to teach fourier optics," in *SPIE's 1995 International Symposium on Optical Science, Engineering, and Instrumentation*. International Society for Optics and Photonics, 1995, pp. 468–472.

[89] G. Junkin, T. Huang, and J. Bennett, "Holographic testing of terahertz antennas," *Antennas and Propagation, IEEE Transactions on*, vol. 48, no. 3, pp. 409–417, 2000.

[90] R. N. Bracewell and R. Bracewell, *The Fourier transform and its applications*. McGraw-Hill New York, 1986, vol. 31999.

[91] A. Tamminen, J. Ala-Laurinaho, and A. Raisanen, "Indirect holographic imaging at 310 ghz," in *Radar Conference, 2008. EuRAD 2008. European*, 2008, pp. 168–171.

[92] H. Sherry, J. Grzyb, Y. Zhao, R. Al Hadi, A. Cathelin, A. Kaiser, and U. Pfeiffer, "A 1kpixel cmos camera chip for 25fps real-time terahertz imaging applications," in *Solid-State Circuits Conference Digest of Technical Papers (ISSCC), 2012 IEEE International*, feb. 2012, pp. 252 –254.

[93] B. E. Coggins and P. Zhou, "Polar fourier transforms of radially sampled {NMR} data," *Journal of Magnetic Resonance*, vol. 182, no. 1, pp. 84 – 95, 2006.

[94] A. Averbuch, R. Coifman, D. Donoho, M. Elad, and M. Israeli, "Fast and accurate polar fourier transform," *Applied and Computational Harmonic Analysis*, vol. 21, no. 2, pp. 145 – 167, 2006.

[95] Hewlett-Packard (HP), "Schottky barrier video detectors," Application Note 923, Tech. Rep., November 1999.

[96] Hewlett-Packard (HP), "The zero bias schottky detector diode," Application Note 969, Tech. Rep., August 1994.

[97] Hewlett-Packard (HP), "Impedance matching techniques for mixers and detectors," Application Note 963, Tech. Rep., August 1980.

[98] G. Torregrosa-Penalva, A. Asensio-López, J. L.-L. de Guevara, and F. J. Ortega-Gonzalez, "Microwave temperature compensated detector design for wide dynamic range applications," *Microwave Journal*, vol. 44, no. 5, p. 336, 2001.

[99] B. Aja Abelán *et al.*, *Amplificadores de banda ancha y bajo ruido basados en tecnología de GaAs para aplicaciones de radiometría.* Universidad de Cantabria, 2007.

[100] B. Aja, J. P. Pascual, L. De La Fuente, M. Detratti, E. Artal, A. Mediavilla, P. De Paco, and L. Pradell i Cara, "Planck-lfi 44 ghz back end module," *Aerospace and Electronic Systems, IEEE Transactions on*, vol. 41, no. 4, pp. 1415–1430, 2005.

[101] J. Oswald and P. Siegel, "The application of the fdtd method to millimeter-wave filter circuits including the design and analysis of a compact coplanar strip filter for thz frequencies," in *Microwave Symposium Digest, 1994., IEEE MTT-S International*, 1994, pp. 309–312 vol.1.

[102] Agilent Technologies, Inc., "Diode detector simulation using agilent technologies eesof ads software," Application Note 1156, Tech. Rep., November 1999.

[103] R. Harrison and X. Le Polozec, "Nonsquarelaw behavior of diode detectors analyzed by the ritz-galerkin method," *Microwave Theory and Techniques, IEEE Transactions on*, vol. 42, no. 5, pp. 840–846, 1994.

[104] W. Deal, N. Kaneda, J. Sor, Y. Qian, and T. Itoh, "A new quasi-yagi antenna for planar active antenna arrays," *Microwave Theory and Techniques, IEEE Transactions on*, vol. 48, no. 6, pp. 910–918, 2000.

[105] D. M. Pozar, "Beam transmission of ultra short waves: An introduction to the classic paper by h. yagi," *Proceedings of the IEEE*, vol. 85, no. 11, pp. 1857–1863, 1997.

[106] H. Yagi, "Beam transmission of ultra short waves," *Proceedings of the IEEE*, vol. 85, no. 11, pp. 1864–1874, 1997.

[107] J.-P. Liu and T.-C. Poon, "Two-step-only quadrature phase-shifting digital holography," *Optics letters*, vol. 34, no. 3, pp. 250–252, 2009.

[108] G. Junkin, "Planar near-field phase retrieval using gpus for accurate thz far-field prediction." *Antennas and Propagation, IEEE Transactions on*, vol. PP, no. 99, p. 1, 2012.

[109] S. Lai, B. King, and M. A. Neifeld, "Wave front reconstruction by means of phase-shifting digital in-line holography," *Optics communications*, vol. 173, no. 1, pp. 155–160, 2000.

UAB

Universitat Autònoma de Barcelona

2014